DEMOCRATIC AND POPULAR REPUBLIC OF ALGERIA
MINISTRY OF HIGHER EDUCATION AND SCIENTIFIC RESEARCH

BLIDA 1 UNIVERSITY

TECHNOLOGY AND SCIENCE

MECHANICAL ENGINEERING DEPARTMENT

PHD THESIS (THIRD CYCLE - LMD)

Closed-loop separated flow control on backward facing step

Contrôle en boucle fermée d'un écoulement décollé sur une marche descendante

---

Author:
Salim KOUAH

Supervisor:
Prof. Mohamed ROUDANE
Co-supervisor:
Assoc. Prof. Fawzi FADLA

Jury Members

BENAROUS Abdellah	Professor	U. Blida 1	President
ROUDANE Mohamed	Professor	U. Blida 1	Thesis Director
FADLA Fawzi	Associate Professor	AMC	Co-Thesis Director
SALHI Merouane	Associate Professor	U. Blida 1	Examiner
DANOUNI Samir	Associate Professor	C.U. Tipaza	Examiner

Abstract

Salim KOUAH

Closed-loop separated flow control on backward facing step

This thesis proposes a novel approach to closed-loop flow control using artificial intelligence (AI), focusing on the prediction and manipulation of dynamic flow behaviors in fluid dynamics applications. The research begins with a numerical investigation of flow separation over a backward-facing step (BFS) using the Detached Eddy Simulation (DES) model, validated against experimental data to ensure fidelity in capturing critical flow features. We introduce a new class of neural networks designed to predict dynamic flow behavior over the (BFS) using wall pressure measurements. These networks achieve high accuracy, enabling real-time flow control applications. The study further explores the influence of frequency information and shear layer dynamics on effective flow control strategies. Leveraging these insights, AI-driven methods are applied to predict and manipulate shear layer behavior, achieving significant improvements in flow control performance. Correlation analyses demonstrate the predictability of future and past flow states within a defined time horizon, offering valuable insights for optimizing both open-loop and closed-loop control systems. These findings contribute to the development of adaptive, efficient flow control strategies with broad implications for aerospace, automotive, and energy systems.

Keywords:
Flow separation; Backward facing step; Instabilities; LSTM Recurrent neural network; Dynamics prediction; Machine learning; Closed loop control.

Résumé

Control en boucle fermée d'un écoulement décollé sur une marche descendante.
Cette thèse propose une nouvelle approche du contrôle d'écoulement en boucle fermée en utilisant l'intelligence artificielle (IA), en mettant l'accent sur la prédiction et la manipulation des comportements dynamiques des écoulements dans les applications de la dynamique des fluides. La recherche commence par une étude numérique de la séparation d'écoulement sur une marche descendante avec le modèle Detached Eddy Simulation (DES), validé par des données expérimentales pour assurer la fidélité dans la capture des caractéristiques essentielles de l'écoulement. Nous introduisons une nouvelle classe de réseaux neuronaux conçus pour prédire le comportement dynamique de l'écoulement au-dessus de la BFS en se basant sur les mesures de pression pariétale. Ces réseaux atteignent une précision élevée, permettant des applications de contrôle d'écoulement en temps réel. L'étude explore en outre l'influence de l'information fréquentielle et de la dynamique de la couche de cisaillement sur l'efficacité des stratégies de contrôle d'écoulement. En s'appuyant sur ces analyses, des méthodes basées sur l'IA sont appliquées pour prédire et manipuler le comportement de la couche de cisaillement, aboutissant à des améliorations significatives des performances du contrôle d'écoulement. Les analyses de corrélation démontrent la prévisibilité des états futurs et passés de l'écoulement sur un horizon temporel défini, offrant des perspectives précieuses pour l'optimisation des systèmes de contrôle en boucle ouverte et en boucle fermée. Ces résultats contribuent au développement de stratégies de contrôle adaptatif et efficace des écoulements, avec de larges implications pour les secteurs de l'aérospatiale, de l'automobile et de l'énergie.

Mots clés :
Décollement de la couche limite; Marche descendante; Instabilités; Réseau de neurones récurrent LSTM; Prédiction de la dynamique; Apprentissage automatique; Contrôle en boucle fermée.

Contents

List of Figures

List of Tables

List of Symbols

AR	Aspect Ratio
ER	Expansion Ratio
Re_h	Reynolds number
f	Frequency
δ	Boundary Layer Length
$\mathrm{U}_i(\mathbf{x}, t)$	Reconstructed field variable
u	Longitudinal velocity
$a_n(t)$	Time coefficients associated with each mode
v	Normal velocity
$\mathbf{\Phi}(\mathbf{x})_n^{(i)}$	i^{th} POD mode at spatial location $\mathbf{x}$, with n modes in total
P	Pressure
ν	Kinematic viscosity
ε	Turbulent dissipation rate
L_t	Turbulence length scale
ρ	Density
t	Time
$\mathbf{C}_{DES}$	A constant used in DES models tocontrol the transition between RANS and LES regions
$\Delta_{\max}$	Largest spacing between grid points in the computational mesh
S_t	Strouhal number
ζ	Vorticity magnitude

Introduction

Flow separation, a fundamental phenomenon in fluid dynamics, occurs when the boundary layer detaches from the surface of an object, when the flow loses its ability to adhere to the surface due to adverse pressure gradients or geometric repture, leading to a significant decrease in flow efficiency. The resulting separation bubble can induce a variety of undesirable effects, including increased drag, flow instability, and reduced aerodynamic performance. Understanding and controlling flow separation is crucial in many engineering applications, such as in the design of aircraft, turbines, and automotive systems, where maintaining smooth and efficient flow over surfaces is vital for optimal performance. A widely studied configuration that demonstrates flow separation is the backward-facing step (BFS). In this setup, a sudden change in surface geometry creates a region of flow separation, followed by a recirculation zone and a reattachment point. The BFS provides a unique opportunity to study turbulent flow behavior, separation dynamics, and the interaction between the flow and surface geometry. This test case has been extensively used in computational fluid dynamics (CFD) simulations to explore separation-induced flow structures and to evaluate various flow control strategies. The purpose of controlling flow separation is to mitigate the negative effects it can have on system performance. In particular, controlling the shear layer position, reattachment point, and turbulence intensity can lead to significant improvements in aerodynamic efficiency. Over the years, a variety of techniques have been developed to control flow separation, ranging from passive methods like vortex generators and surface modifications to more active methods such as jet actuators, suction, and pulsed flow manipulation. These traditional control methods have demonstrated varying degrees of success but often face limitations in terms of adaptability, precision, and energy efficiency. In recent years, artificial intelligence (AI) and machine learning techniques have emerged as powerful tools for addressing these challenges. AI offers the potential for adaptive, data-driven control strategies that can dynamically adjust to changing flow conditions in real time. In particular, techniques such as neural networks which have shown promise in modeling and predicting complex flow behaviors by learning from historical data. These AI-based approaches can enhance the precision of flow control, enabling more effective manipulation of flow dynamics. In this thesis, we propose a novel approach to closed-loop flow control using AI, focusing on predicting and controlling the dynamic behaviors of flow over a backward-facing step. We first numerically investigate the flow separation phenomenon using the Detached Eddy Simulation (DES) model, which is validated against experimental results under similar conditions. This provides a foundation for exploring more advanced control techniques.

After that we compare various strategies for controlling separated flow over a (BFS), focusing on active flow control using continuous and pulsed jets, alongside a novel technique. The proposed method employs a closed-loop control system that monitors wall pressure to activate flow control only when the separation bubble reaches its maximum size. By targeting specific timing, this approach optimizes airflow management while minimizing energy consumption. Results demonstrate that this method not only effectively regulates flow but also consumes less energy compared to conventional continuous and pulsed jet techniques. These findings highlight its potential for more energy-efficient aerodynamic applications. We then introduce a new generation of LSTM neural networks that leverage wall pressure measurements to predict dynamic flow behavior. These networks are trained to predict the shear layer position and other critical flow features, enabling more precise and efficient control strategies. Through this study, we demonstrate the effectiveness of using AI-based control methods to predict and manipulate flow dynamics, with a particular focus on improving the time response and stability of closed-loop control systems. By applying LSTM networks to predict future flow dynamics, we provide a pathway for real-time, adaptive control of flow separation, which holds great potential for improving the performance of a wide range of fluid systems.

Introduction to Separated Flow: Fundamental Concepts and Challenges

Chapter abstract

This chapter introduces the fundamental principles of separated flow, a key phenomenon in fluid mechanics where the boundary layer detaches from a surface. It explores the theoretical background, common challenges, and significance of flow separation in various engineering applications.

I.1 Introduction to Flow Separation

Flow separation is a critical phenomenon in fluid dynamics that occurs when the flow of a fluid detaches from the surface of an object. This detachment happens when the boundary layer of the fluid, which is the layer closest to the surface, experiences a significant adverse pressure gradient. As the fluid moves along the surface, it gradually decelerates due to this pressure gradient, eventually reaching a point where the flow can no longer adhere to the surface and separates, leading to the formation of a wake and increased turbulence. The significance of flow separation is evident across various engineering disciplines. In aerodynamics, for example, flow separation on aircraft wings results in increased drag and reduced lift, which can severely affect flight performance and fuel efficiency. Similarly, in automotive engineering, flow separation around a vehicle can contribute to higher drag forces, impacting speed and fuel consumption. In civil engineering, flow separation around structures such as bridges and buildings can influence their stability and durability under wind loads [27]. The impact of flow separation extends beyond traditional applications, with advancements in control strategies playing a crucial role in mitigating its adverse effects. Techniques such as vortex generators, which create controlled disturbances in the boundary layer, and boundary layer suction, that removes the separated flow, are employed to delay or prevent separation. Additionally, active flow control methods, including the use of oscillatory air jets and adaptive surfaces, are being explored to improve aerodynamic efficiency. The principles of Fundamentals of Aerodynamics are integrated into design processes to enhance these methods. These advancements aim to optimize

flow management and enhance performance in both aerospace and automotive applications, as well as in other engineering domains [15]. Understanding and controlling flow separation is essential for optimizing the performance and efficiency of various engineering systems. Continued research and technological advancements are key to overcoming the challenges associated with flow separation and improving the design and functionality of aerodynamic and hydrodynamic systems.

I.2 Fundamental Concepts of Flow Separation

I.2.1 Boundary Layer Theory

The boundary layer is the thin layer of fluid that adheres to a surface due to viscosity. As the fluid travels along the surface, it experiences a gradual decrease in velocity due to frictional forces as shown in fig I.1. The behavior of this boundary layer is crucial in determining whether or not flow separation occurs. When the boundary layer encounters an adverse pressure gradient, it slows down and may eventually detach from the surface, leading to flow separation. The theory of boundary layer separation was first studied by Prandtl in 1904, identifying separation as occurring at the wall where the shear stress is zero with a negative axial gradient. This initial formulation served as the first criterion for detecting separation, but it was only valid for steady, two-dimensional flows. This limitation led scientists to investigate other criteria applicable to unsteady, two- and three-dimensional flows. Since then, mathematical tools and numerical simulation techniques have evolved, aiding the development of new separation criteria. Perry and Fairlie (1975) focused on solving boundary layer equations, defining separation as the appearance of a singularity in the solution. Van Dommelen and Cowley (1990) adopted a similar approach but used Lagrangian coordinates, offering better insights into unsteady separation dynamics compared to Eulerian frames. However, in both cases, the emergence of a singularity in the numerical resolution of boundary layer equations suggested that the original assumptions were no longer valid, though this did not necessarily indicate a separation phenomenon. A general criterion for detecting unsteady separation was proposed by Haller in 2004, offering a kinematic, Lagrangian, and non-linear approach. In this new theory, separation is identified as a material instability caused by a material line emanating from a point on the wall. Over time, these unstable structures attract and eject particles near the wall, and the theory allows for determining both the position and the shape of the separation profile. Remarkably, this approach can be applied to unsteady, compressible, and incompressible flows, unifying previous theoretical efforts into a single framework. Haller (2004) also defined two types of separation: fixed separation, which occurs when the flow has a well-defined average, such as in periodic flows where the separation characteristics are obtained over one period; and moving separation, where the separation point changes over time. These findings were later extended to three-dimensional steady flows (Surana et al., 2006) and further applied to unsteady three-dimensional flows (Surana et al., 2008b).

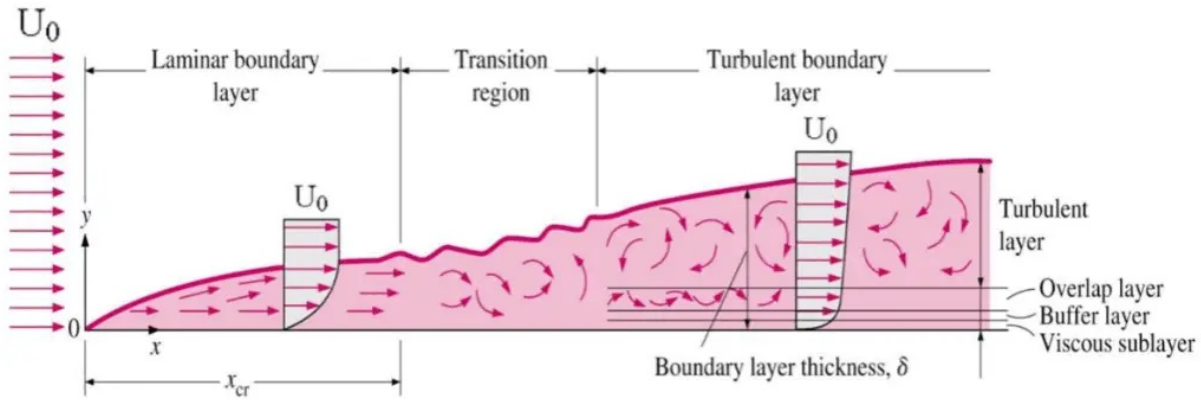

FIGURE I.1: Different types of separation include geometry-induced separation (on the left), caused by abrupt changes in surface contours, and pressure gradient-induced separation (on the right), resulting from adverse pressure gradients.[11]

I.3 Geometric Influences

The shape and curvature of the surface significantly affect flow separation. Sharp edges, abrupt changes in surface geometry, and high-curvature regions tend to increase the likelihood of separation. Smooth and gradual changes in surface contours can help mitigate separation by maintaining a more stable boundary layer. Design considerations often involve optimizing surface geometry to manage flow behavior and reduce adverse effects.

I.3.1 Causes of Flow Separation: Adverse Pressure Gradient and Geometric Rupture

Flow separation occurs when the boundary layer of a fluid, moving along a surface, can no longer remain attached to that surface. Two primary factors lead to this detachment: the presence of an adverse pressure gradient and abrupt changes in surface geometry, known as geometric rupture.

Adverse Pressure Gradient

A pressure gradient refers to how pressure changes along the flow direction. In fluid dynamics, an adverse pressure gradient occurs when pressure increases in the direction of the flow. This creates a decelerating force on the fluid particles, making it difficult for the boundary layer (the thin layer of fluid close to the surface) to overcome the growing pressure. As the boundary layer moves downstream, the increasing pressure causes it to lose momentum. Eventually, the fluid's velocity within the boundary layer decreases to zero, leading to flow reversal and separation, shown in the right of Fig.I.2. The adverse pressure gradient usually arises in situations where the flow transitions from a low-pressure to a high-pressure region, such as over the trailing edge of an airfoil or downstream of a vehicle body. This gradient opposes the flow's movement, which weakens the boundary

layer's energy and leads to detachment. Once separation occurs, the smooth laminar flow is replaced by chaotic, turbulent flow, creating a wake region behind the object and increasing drag [31].

Geometric Rupture

In addition to pressure gradients, geometric rupture or abrupt changes in surface geometry can also cause flow separation. When fluid flows over a surface, it naturally follows the contours of that surface. However, if the surface has sharp angles, sudden curvature changes, or discontinuities, the boundary layer struggles to follow the new shape due to inertia and viscous forces as shown in the left of Fig.I.2. For example, on a blunt object or one with a backward-facing step, abrupt geometric changes prevent the boundary layer from adhering to the surface, leading to flow separation. This separation increases drag and may induce structural vibrations or oscillations. The sharpness of the surface curvature is a key factor in geometric-induced separation. High-curvature regions or sharp angles significantly increase the likelihood of separation. In contrast, surfaces with gradual curvature transitions are more likely to maintain attached flow, reducing drag and improving aerodynamic efficiency[14] .

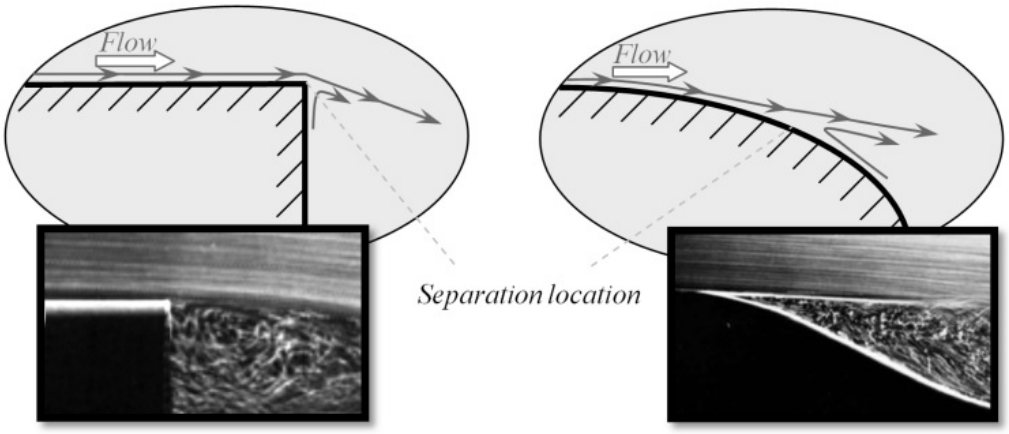

FIGURE I.2: Different types of separation include geometry-induced separation (on the left), caused by abrupt changes in surface contours, and pressure gradient-induced separation (on the right), resulting from adverse pressure gradients.[11]

I.4 Backward facing step

The study of flow over a backward-facing step (BFS) in turbulent regimes is a prominent area of interest in both academic and industrial research. The BFS is favored due to its simple geometry, which facilitates controlled investigations of flow separation caused by geometric disruption [8]. With its sharp 90° angle, the BFS provides ideal conditions for

studying separation behavior. The geometry's simplicity and the ability to control key parameters make it one of the most widely studied configurations for examining separated flows. ANTONIO and LACERDA DE BREDERODE (1972) emphasized the importance of the aspect ratio (AR), defined as the width of the test section divided by the height of the step. Their study concluded that when the AR exceeds 10, the flow over the BFS becomes predominantly two-dimensional, and the influence of side walls can be ignored. This finding is essential for ensuring that the flow can be accurately modeled without significant interference from boundary effects, which is critical for applications seeking to isolate the primary separation mechanics. Ötügen (1991) expanded the scope by investigating the impact of the expansion ratio (ER), defined as the ratio of the height of the test section to the difference between the height of the test section and the step. Ötügen's research demonstrated that organized flow structures, such as vortices, are highly sensitive to variations in the expansion ratio, thereby influencing the overall behavior of the separated flow region. The interplay between ER and organized structures provides insight into how geometric factors shape the reattachment of the separated flow downstream. Sujar Garrido et al. (n.d.) contributed to this field by identifying that flow separation over a BFS is governed by both flow conditions (e.g., turbulence intensity, boundary layer thickness) and geometric factors (e.g., ER and AR). Their work highlighted that both the incoming flow's characteristics and the step's geometry must be considered together to fully understand the separation and reattachment processes. Their emphasis on combining these factors helps deepen the understanding of the complex dynamics present in separated flow regimes. Building on this, Chovet et al. (2017) carried out experiments on BFS flows using an ER of 1.04 and an AR of 24, achieving near-ideal two-dimensional flow. Their configuration minimized the influence of the upper wall and side walls, providing a purer insight into flow separation without interference from extraneous factors. Based on this, our own research has adopted similar conditions, ensuring that wall effects are minimized and that flow behavior can be studied in a near-perfect two-dimensional setting. Further investigations have also sought to explore variations in BFS geometry. Armaly et al. (1983) investigated laminar and turbulent flows over BFSs, examining the transition from laminar to turbulent regimes. Their findings indicated that reattachment length varies significantly between laminar and turbulent flow, with turbulence causing earlier reattachment due to increased mixing. This study set the groundwork for understanding how flow regime transitions affect separated flow behavior. Similarly, Driver and Seegmiller (1985) provided valuable experimental data on turbulent BFS flow at higher Reynolds numbers, documenting the detailed flow structure downstream of the step. Their experiments captured critical information about the development of shear layers, the formation of vortices, and the eventual reattachment of the flow. Their work remains a fundamental reference for validating numerical simulations of separated turbulent flow.

I.5 Flow Characteristics

I.5.1 Flow Separation

When the flow encounters the backward step, the boundary layer experiences an adverse pressure gradient, and geometric repture leading to flow separation. The separation occurs just downstream of the step, where the velocity component normal to the surface decelerates and the boundary layer cannot stay attached to the surface.

I.5.2 Recirculation Zone

Following separation, the flow reverses direction and forms a recirculation zone behind the step. This recirculation is typically characterized by low velocities and turbulent eddies shown in fig I.3. The size of the recirculation zone is a key parameter that depends on the Reynolds number Re, step height h, and the free-stream velocity U_∞.

I.5.3 Reattachment Point

The flow reattaches to the wall after the recirculation zone. The location of the reattachment point, denoted L_r, depends on several factors including the step height, Reynolds number, and upstream flow conditions. In typical BFS configurations, the reattachment occurs a few step heights downstream of the separation point. The BFS flow configuration is an important model for studying flow separation, recirculation, and reattachment. Understanding the dynamics of BFS is crucial for applications in fluid dynamics and heat transfer, where controlling these flow features can lead to improved designs and performance.

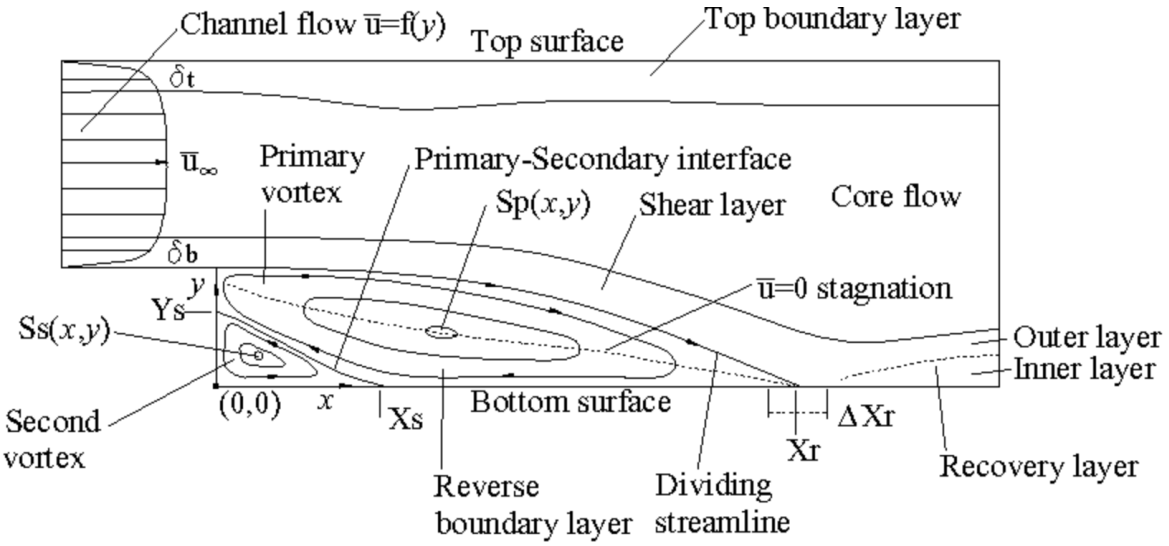

FIGURE I.3: Mean flow structures in the CS plane of symmetry of the turbulent BFS flow.[13]

I.6 Flow Control Strategies

Flow control can be categorized into two primary approaches: **active** and **passive** control (fig I.4). Each method offers different advantages depending on the desired outcomes and flow conditions.

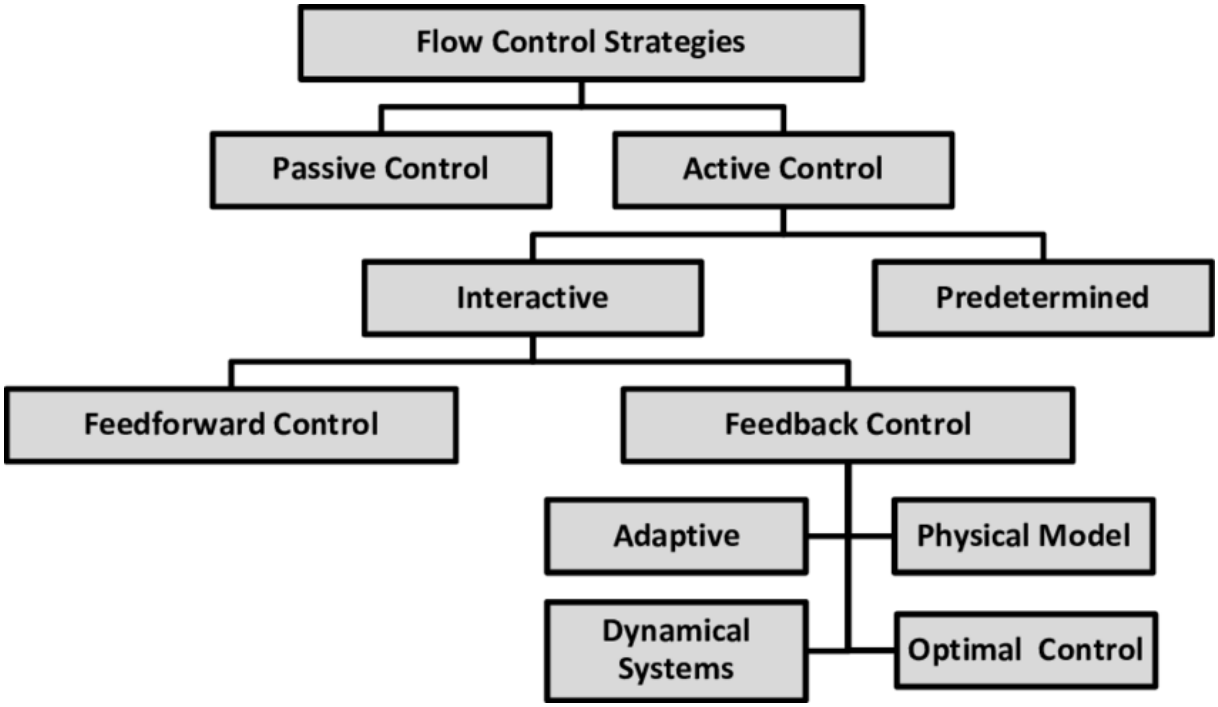

FIGURE I.4: Classification of flow control methods[1]

I.6.1 Passive Flow Control

Passive flow control involves using fixed devices or surface modifications to influence the flow without external energy input. These methods are simple and cost-effective, but they cannot adapt to changing flow conditions. Examples of passive flow control include:

- **Vortex generators**: Small, fixed devices that create vortices in the boundary layer, delaying separation and reducing drag.
- **Riblets**: Microstructures or grooves on a surface that streamline the flow and reduce friction drag.
- **Surface modifications**: Geometric changes, such as bumps or slats, used to influence flow behavior passively.

I.6.2 Active Flow Control

Active flow control, on the other hand, requires external energy input to manipulate the flow. These systems are dynamic and can adapt to changing flow conditions, making them more versatile than passive systems. Examples of active flow control include:

- **Blowing or suction**: Injecting or removing fluid to manipulate the boundary layer, which can energize or thin the flow.
- **Synthetic jets**: Pulsating air jets used to alter the momentum of the flow without adding mass.
- **Plasma actuators**: Devices that use ionized air to produce local forces to change the flow properties.

I.7 Control Methodologies: Open-Loop vs. Closed-Loop

Control systems are integral to modern engineering and technology. They are used in a wide range of applications, from household appliances to complex industrial machinery. Control systems can be broadly classified into two categories: open-loop and closed-loop systems. Understanding these systems is crucial for designing effective and efficient control mechanisms.

I.8 Open-Loop Control Systems

I.8.1 Definition

An open-loop control system operates based on a fixed set of instructions without using feedback to adjust its actions. The control action is predetermined and not dependent on the output of the system. In an open-loop system, the control action is predefined and operates without real-time feedback from the flow field. The controller sends signals to the actuators based on fixed commands, without adjusting for variations in flow conditions.

- **Advantages**: Simpler to implement, as it does not require real-time sensors or feedback mechanisms.
- **Disadvantages**: Cannot adapt to changing flow conditions, which reduces efficiency in dynamic environments.

Example: A fixed-rate blowing strategy on an airfoil where the flow injection is constant regardless of changing flow dynamics.

I.8.2 Characteristics

- No Feedback: The system does not monitor the output.

- Simple Design: Due to the lack of feedback, the design is straightforward.
- Less Accurate: It cannot correct any errors that occur during operation.

I.8.3 Mathematical Modeling

In open-loop control systems, the relationship between the input $R(s)$ and the output $C(s)$ can be represented using transfer functions. The transfer function $G(s)$ of an open-loop system is given by:

$$G(s) = \frac{C(s)}{R(s)}$$

The block diagram representation of an open-loop control system is shown in Figure I.5.

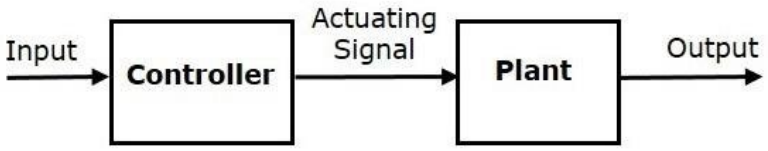

FIGURE I.5: Block Diagram of an Open-Loop Control System

I.8.4 Examples

- Electric Toaster: Operates for a set time period regardless of the actual toasting level.
- Washing Machine: Runs on a preset cycle without considering the cleanliness of the clothes.

I.8.5 Advantages and Disadvantages

Advantages:

- Simplicity in design and implementation.
- Lower cost and fewer components.

Disadvantages:

- Lack of accuracy and precision.
- Cannot adapt to changes or disturbances in the system.

I.9 Closed-Loop Control Methods

I.9.1 Introduction

Closed-loop control systems are a cornerstone of modern engineering and technology. These systems are crucial for maintaining desired system outputs by automatically adjusting the input based on feedback from the system's output. This adaptive capability makes those systems superior in applications where precision and reliability are paramount. From maintaining a stable temperature in an industrial furnace to regulating the speed of an electric motor, closed-loop control is ubiquitous in both everyday appliances and sophisticated technological systems. Frequently referred to as feedback control, is an approach implemented in systems that demand dynamic regulation of output by comparing it to a specified reference value or setpoint. Through continuous monitoring of the actual output and adjusting inputs accordingly, closed-loop control ensures stability and resilience to external disturbances and system changes.

I.9.2 Basic Structure of Closed-Loop Control Systems

A closed-loop control system continuously monitors the output and compares it with the desired reference input. Any deviation from the desired output is used to generate an error signal, which is then processed by the controller to bring the system back to the desired state. The primary components of a closed-loop control system are shown in fig **??**, and include:

- **Reference Input** ($R(s)$): The target or setpoint that the system aims to achieve. This could be a desired temperature, speed, position, or any other measurable quantity.
- **Controller**: The brain of the control system. It receives the error signal (difference between the reference input and the actual output) and determines the appropriate corrective action to minimize this error.
- **Actuator**: This component executes the corrective action determined by the controller. It could be an electric motor, a valve, a heater, etc., depending on the application.
- **Process/Plant**: The system being controlled, such as a mechanical device, a chemical process, or an electrical system.
- **Sensor/Feedback** ($H(s)$): This component measures the actual output of the system and feeds it back to the controller to compare with the reference input.

The closed-loop feedback mechanism is what distinguishes closed-loop systems from open-loop systems. By continuously monitoring the output and making real-time adjustments, closed-loop systems can correct disturbances and changes in the system dynamics, ensuring that the desired performance is maintained.

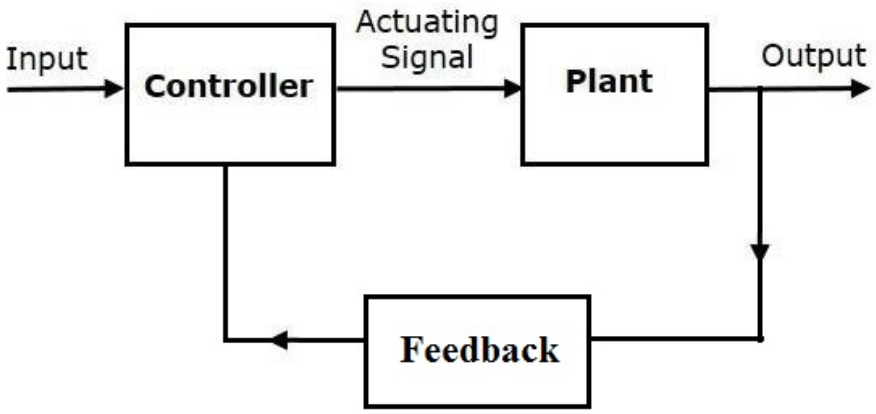

FIGURE I.6: Diagram of a closed-loop control system showing feedback mechanisms.

I.9.3 Mathematical Modeling of Closed-Loop Control Systems

The mathematical representation of closed-loop systems is essential for understanding and designing these systems. The relationship between the input and output of a closed-loop system can be described using transfer functions in the Laplace domain.

Transfer Function

The transfer function $T(s)$ of a closed-loop system describes how the output responds to an input over time:

$$T(s) = \frac{G(s)}{1 + G(s)H(s)}$$

where:

- $G(s)$ is the transfer function of the forward path, including the controller and the plant.
- $H(s)$ is the transfer function of the feedback path, which typically includes the sensor dynamics.

The transfer function $T(s)$ reveals important characteristics of the system such as stability, responsiveness, and how it handles disturbances. The denominator $1 + G(s)H(s)$ is known as the characteristic equation, and its roots (poles) determine the stability of the system.

Error Signal

The error signal $e(t)$ is the difference between the reference input $R(s)$ and the actual output $C(s)$:

$$e(t) = R(s) - C(s)$$

This error signal is what drives the corrective actions in a closed-loop system. The controller processes this error to reduce it to zero or to an acceptable level, ensuring the system output matches the desired reference.

I.9.4 Proportional-Integral-Derivative (PID) Control

PID control is one of the most commonly used closed-loop control strategies due to its simplicity and effectiveness. It combines three types of control actions: proportional, integral, and derivative (fig I.7).

Proportional Control (P)

- Proportional control adjusts the control action directly proportional to the error signal. If the error is large, the control action is large, and vice versa. - The control signal $u(t)$ in proportional control is given by:

$$u(t) = K_p e(t)$$

where K_p is the proportional gain. A higher K_p value increases the system's responsiveness but can lead to overshoot and instability if set too high.

Integral Control (I)

- Integral control aims to eliminate steady-state error by considering the accumulation of past errors. It integrates the error over time, adjusting the control action to address any residual offset. - The control signal $u(t)$ for integral action is:

$$u(t) = K_i \int_0^t e(\tau) d\tau$$

where K_i is the integral gain. While integral control can eliminate steady-state error, it can also lead to increased overshoot and oscillations if not properly tuned.

Derivative Control (D)

- Derivative control predicts future errors by calculating the rate of change of the error. It provides a damping effect, reducing the tendency to overshoot and enhancing system stability. - The control signal $u(t)$ for derivative action is:

$$u(t) = K_d \frac{de(t)}{dt}$$

where K_d is the derivative gain. Derivative control improves system response by counteracting the rate of error change, but it is sensitive to noise in the error signal.

PID Controller

- A PID controller combines the proportional, integral, and derivative actions to provide a comprehensive control strategy:

$$u(t) = K_p e(t) + K_i \int_0^t e(\tau) d\tau + K_d \frac{de(t)}{dt}$$

- The effectiveness of a PID controller depends on the proper tuning of K_p, K_i, and K_d. Various tuning methods, such as Ziegler-Nichols or software-based optimization, can be used to find the optimal values for these gains. - PID controllers are versatile and can be used in a wide range of applications, from temperature control to industrial automation and robotics.[16]

I.10 Proportional-Integral-Derivative (PID) Control

The PID controller combines proportional, integral, and derivative components to effectively regulate system behavior. This controller is extensively used due to its adaptability and simplicity.

I.10.1 PID Control Law

The control action in a PID system is described by:

$$u(t) = K_p e(t) + K_i \int e(t)\, dt + K_d \frac{de(t)}{dt} \tag{I.1}$$

where:

- $e(t) = r(t) - y(t)$ is the error between reference $r(t)$ and output $y(t)$,
- K_p, K_i, and K_d are the proportional, integral, and derivative gains, respectively.

I.10.2 Tuning Techniques

Ziegler-Nichols Method: This heuristic tuning approach adjusts K_p, K_i, and K_d based on inducing oscillations in the system at critical gain. **Trial-and-Error**: Parameters are incrementally adjusted based on the observed response until optimal performance is achieved.

I.11 Adaptive Control

Adaptive control modifies its control parameters in real-time to accommodate varying process characteristics. This makes it suitable for systems with non-stationary behaviors.

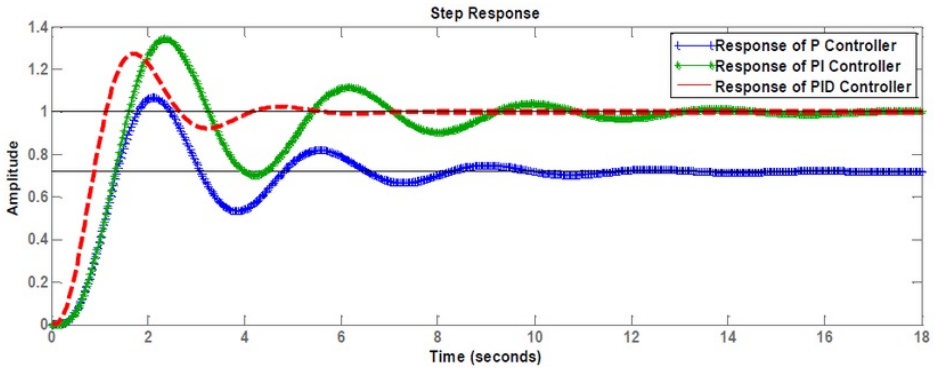

FIGURE I.7: Typical response curve of a system under PID control, showing effects of P, I, and D actions.

I.11.1 Model Reference Adaptive Control (MRAC)

Model Reference Adaptive Control (MRAC) tunes the control parameters based on a specified reference model shown in figI.8, following an adaptive adjustment rule as:

$$\theta(t+1) = \theta(t) + \gamma e(t) x(t) \tag{I.2}$$

where:

- $\theta(t)$ represents the vector of control parameters,
- γ is a gain coefficient,
- $e(t)$ is the error between the system output and the reference model output,
- $x(t)$ includes system state variables.

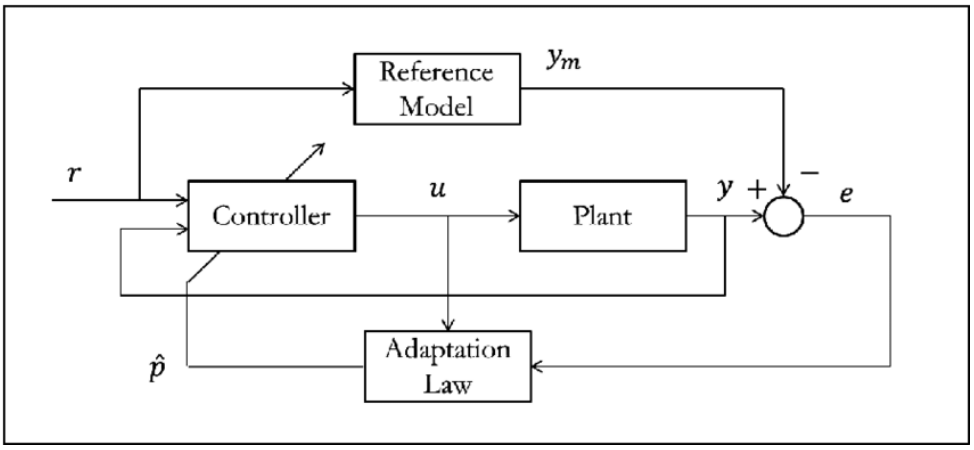

FIGURE I.8: Schematic of Model Reference Adaptive Control (MRAC) system, showing process adaptation.
[4]

I.12 Model Predictive Control (MPC)

Model Predictive Control (MPC) optimizes control actions over a specified horizon by using predictive models to account for future system behavior. MPC adjusts parameters dynamically for optimal system performance.

I.12.1 Optimization Formulation

The objective in MPC is to minimize:

$$\min_{u} \sum_{k=0}^{N} \left(y_k - r_k\right)^2 + \lambda \sum_{k=0}^{N} u_k^2 \tag{I.3}$$

subject to system dynamics:

$$x_{k+1} = Ax_k + Bu_k, \quad y_k = Cx_k \tag{I.4}$$

where:

- N is the prediction horizon,
- λ penalizes control effort,
- A, B, and C represent system matrices.

I.13 Linear Quadratic Regulator (LQR)

The Linear Quadratic Regulator (LQR) minimizes a quadratic cost function to provide optimal control for state-space systems, balancing control effort and accuracy.

I.13.1 Cost Function for LQR

The LQR objective function is defined as:

$$J = \int_0^\infty \left(x^T Q x + u^T R u\right) \, dt \tag{I.5}$$

where:

- x is the state vector,
- u is the control input,
- Q and R are weight matrices for states and inputs, respectively.

The control law that minimizes J is given by:

$$u = -Kx \tag{I.6}$$

where K is computed by solving the Riccati equation.

I.14 Sliding Mode Control (SMC)

Sliding Mode Control (SMC) forces system dynamics to follow a predefined sliding surface, ensuring robust performance under disturbances and model uncertainties.

I.14.1 Sliding Mode Control Law

The sliding surface is defined as:

$$s(x) = 0 \tag{I.7}$$

The control action for SMC is:

$$u = u_{eq} - k\,\mathrm{sign}(s(x)) \tag{I.8}$$

where:

- u_{eq} is the equivalent control,
- $k\,\mathrm{sign}(s(x))$ is the discontinuous control component.

I.14.2 Machine Learning Control (MLC)

Machine Learning Control (MLC) represents an advanced approach to closed-loop control, particularly suited for complex, non-linear systems where traditional control methods may fall short. MLC uses data-driven techniques to develop and adapt control strategies.

Concept of MLC

- MLC employs machine learning algorithms to learn control policies directly from data, without requiring an explicit mathematical model of the system. - This approach is especially valuable for systems with high dimensionality, non-linear dynamics, and unknown or time-varying characteristics. - Unlike traditional control methods, which rely on a fixed control law, MLC can continuously adapt to changes in the system and the environment.

Implementation of MLC

- - **Training Phase**: In the initial phase, the control system collects data from the plant under various operating conditions. This data is used to train a machine learning model, such as a neural network, genetic programming, or reinforcement learning algorithm.
- - **Learning Phase**: The machine learning model learns the optimal control strategy by minimizing a cost function that represents the desired system behavior. The cost function may include terms for tracking accuracy, stability, and control effort.
- - **Execution Phase**: The trained model is deployed in real-time to control the plant. It processes sensor feedback and determines the appropriate control action to achieve the desired performance.

Advantages of MLC

- Adaptability : MLC can adapt to new or changing system dynamics, making it robust to uncertainties and disturbances. - Complexity Handling : MLC can manage systems with complex, non-linear interactions and multi-input-multi-output (MIMO) configurations, where traditional control methods may struggle. - Model-Free Approach: Unlike model-based control strategies, MLC does not require an explicit mathematical model of the system, making it suitable for systems where modeling is difficult or impossible.

Applications of MLC

- MLC has been successfully applied in various fields, including fluid dynamics for controlling turbulent flows, automotive systems for adaptive cruise control, and robotics for learning-based control of complex maneuvers. - In turbulent flow control, for example, MLC can optimize the control of flow separation and mixing layers, leading to improved aerodynamic performance and energy efficiency.

I.14.3 Challenges and Considerations in Closed-Loop Control

While closed-loop control offers significant advantages, it also presents challenges that need to be addressed for successful implementation:

- Stability: Ensuring system stability is crucial, especially when dealing with high-gain controllers or systems with significant delays. Stability analysis and controller tuning are essential to prevent oscillations and instability.
- Complexity: Designing closed-loop control systems for non-linear and high-dimensional systems can be complex. Advanced control strategies like MLC require a deep understanding of both control theory and machine learning techniques.
- Computational Resources : Real-time implementation of complex control algorithms, especially those involving machine learning, requires significant computational power. Efficient algorithms and hardware are necessary to achieve the desired performance.
- Noise Sensitivity: Sensors and feedback signals are often subject to noise and disturbances. Controllers, especially those with derivative actions, need to be designed to handle noise effectively without degrading system performance.

Closed-loop control, or feedback control, continuously adjusts the control inputs based on real-time sensor data. The system measures the flow conditions (e.g., turbulence, separation), and the actuators respond dynamically to optimize the flow behavior.

- **Advantages**: Highly adaptive, providing optimal control under varying conditions by adjusting based on real-time feedback.
- **Disadvantages**: More complex and costly to implement due to the need for real-time sensors, controllers, and actuators.

Example: In a closed-loop system for an aircraft wing, sensors detect the onset of flow separation, and the actuators adjust the blowing or suction rate to counteract the separation.

I.15 Hybrid Control

In some cases, hybrid control systems are used, combining open-loop control for baseline actions and closed-loop feedback to fine-tune the system when necessary.

I.16 Applications of Flow Control

Flow control strategies are widely applied in various industries:

- **Aerodynamics**: Reducing drag and preventing flow separation over aircraft wings, car bodies, and turbine blades.
- **Hydrodynamics**: Minimizing resistance on ship hulls and underwater vehicles to improve performance.
- **Energy Systems**: Enhancing heat transfer in cooling systems or power generation by optimizing fluid flow.
- **Applications in Aviation and Industry** Flow control has broad applications, particularly in the aviation industry. A small reduction in drag, such as 1%, translates to significant fuel savings for large aircraft like the Boeing 747. Moreover, flow control is used to improve efficiency in various industries, including automotive, turbomachinery, and even energy production systems.

I.17 General Insights

Closed-loop control systems are essential in applications where precision, adaptability, and robustness are required. The continuous feedback mechanism allows these systems to correct errors and adapt to changing conditions, providing superior performance compared to open-loop systems. Traditional methods like PID control offer simplicity and effectiveness for many applications, while advanced techniques like Machine Learning Control provide powerful solutions for complex, non-linear systems. Understanding and implementing closed-loop control is fundamental for the design of modern automated systems [8]. Within active flow control, there are different strategies for controlling the actuators: **open-loop** and **closed-loop** control.

- **Performance** Open-loop systems are generally less accurate as they do not account for disturbances or changes in the system. Closed-loop systems, however, offer high precision due to their feedback mechanism, allowing them to adapt and correct any errors.

- **Use Cases** Open-loop systems are suitable for simple applications where accuracy is not critical. In contrast, closed-loop systems are used in applications requiring high precision and adaptability, such as in industrial automation and robotics.

To summarize, flow control can be achieved through either passive or active methods:

- **Passive control** uses fixed, energy-free devices like vortex generators or riblets.
- **Active control** adapts to flow conditions, using strategies such as blowing, suction, or plasma actuators.

These methods are crucial for optimizing performance in systems where controlling fluid behavior is critical to efficiency. Flow control remains a vital tool in modern engineering, offering solutions that range from simple passive methods to advanced active technologies. As research advances, flow control will continue to play a key role in improving performance, safety, and environmental sustainability in numerous applications.

I.18 Socio-Economic Implications of Separated Flow Phenomena

I.18.1 Energy Efficiency and Costs

Separated flow phenomena can significantly influence the drag force experienced by vehicles and aircraft. When flow separates from a surface, such as an aircraft wing or car body, it creates a turbulent wake that increases drag. This effect can lead to higher fuel consumption and operational costs. For example, reducing drag in automobiles through improved aerodynamic design can lead to better fuel efficiency, which is both economically advantageous and environmentally beneficial.

Implications

- **Automobiles:** Car manufacturers invest heavily in aerodynamic testing and design to minimize drag. Improved aerodynamics can lead to substantial savings in fuel costs over a vehicle's lifetime.
- **Aerospace:** In aviation, drag reduction can lead to lower operational costs for airlines and improved range and performance for aircraft.

Example

The design of the Airbus A380 involved extensive wind tunnel testing and computational fluid dynamics (CFD) simulations to reduce drag (fig I.9). This led to improvements in fuel efficiency and reduced operating costs for airlines.

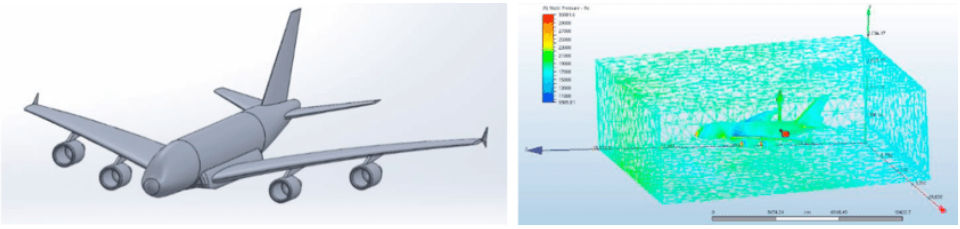

FIGURE I.9: Computational fluid dynamics (CFD) simulation on Airbus A380 aircraft model, [23].

I.18.2 Infrastructure and Maintenance

Separated flows can induce vibrations and additional stresses in structures such as bridges, towers, and buildings. These effects can lead to accelerated wear and tear, increased maintenance costs, and potential safety risks. Understanding and mitigating these effects are crucial for ensuring the longevity and safety of infrastructure.

Implications

- **Bridges:** Flow-induced vibrations can lead to fatigue and structural damage over time. Engineers use flow simulations to design bridges that minimize these effects.
- **Buildings:** Tall buildings and skyscrapers must account for wind-induced flow separation to ensure stability and comfort for occupants.

Example

The collapse of the Tacoma Narrows Bridge in 1940 was partly due to vortex shedding, a type of flow separation. This event highlighted the importance of understanding aerodynamic effects on structures [28].

I.18.3 Environmental Impact

Improving aerodynamic efficiency not only reduces fuel consumption but also decreases greenhouse gas emissions. By enhancing vehicle and aircraft designs to minimize drag and manage separated flows better, industries can contribute to environmental sustainability.

Implications

- **Automotive Industry:** Advanced aerodynamics in electric and hybrid vehicles can reduce energy consumption and emissions.
- **Aerospace Industry:** Efficient aircraft designs lead to reduced carbon footprints and align with global sustainability goals.

Example In wind tunnel tests as shown in fig I.10, the ŠKODA OCTAVIA Hatchback and Sedan models achieved remarkably low drag coefficients of 0.24 and 0.26, respectively.

This comparison highlights the effectiveness of the aerodynamic design implemented in both models, positioning the OCTAVIA as one of the most aerodynamically efficient vehicles in its class. The outstanding aerodynamic characteristics of the new ŠKODA OCTAVIA are the result of many years of development, with significant input from experts across various engineering fields. By implementing targeted strategies, ŠKODA's aerodynamics team successfully achieved these low Cd values. Here are some of the key measures taken:

- **Body Shape Optimization:** Streamlining the exterior design to minimize air resistance across both the Hatchback and Combi versions.
- **Enhanced Underbody Design:** Reducing turbulence with a smooth underbody layout that improves airflow efficiency.
- **Aerodynamic Components:** Incorporating spoilers, diffusers, and other design features to manage airflow and further decrease drag.

These aerodynamic improvements underscore the OCTAVIA's position as a highly efficient family car with both elegance and advanced engineering. [22]

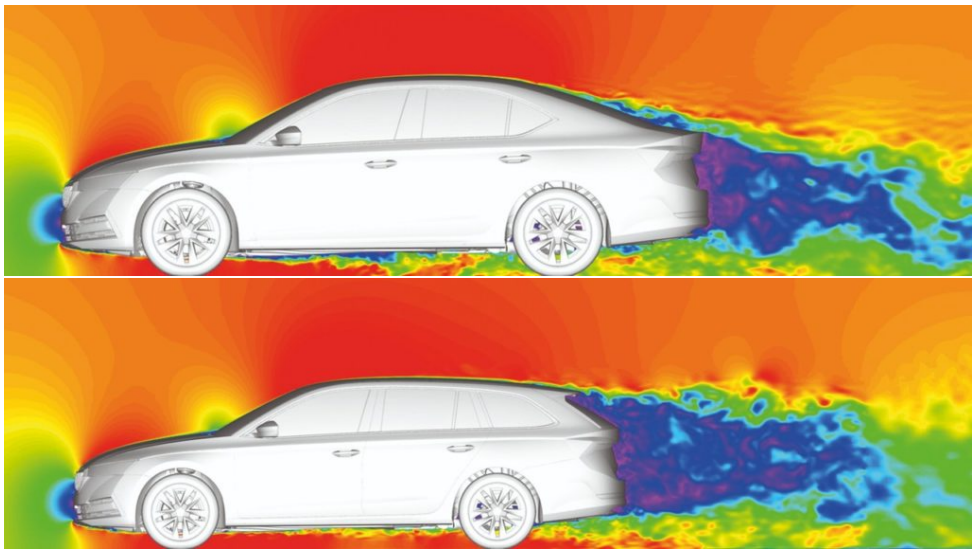

FIGURE I.10: Comparative Study between ŠKODA OCTAVIA Hatchback and Sedan Models

I.18.4 Safety and Performance

Better understanding and management of separated flow phenomena can significantly enhance the safety and performance of vehicles and aircraft. Reducing adverse effects such as turbulence and vortex-induced vibrations can prevent accidents and improve operational reliability.

Implications

- **Aircraft Safety:** Improved aerodynamic designs reduce the risk of stalls and improve overall flight safety.
- **Vehicle Performance:** Enhanced aerodynamic properties can lead to better handling and stability in vehicles.

I.19 Bio-Inspired Flow Control Techniques

Nature has long provided engineers with solutions to complex problems through the concept of biomimicry, which involves emulating the forms, structures, and processes found in the natural world. In the field of flow control, biomimetic techniques harness the highly efficient and adaptive designs observed in animals, plants, and other organisms to optimize aerodynamic and hydrodynamic performance. These bio-inspired strategies have been successfully applied across various industries, from aviation to renewable energy, improving efficiency and sustainability.

I.19.1 Sharkskin-Inspired Riblets

One of the most widely known examples of bio-inspired flow control is the use of riblets, which are directly inspired by the micro-structures found on sharkskin. Sharks are among the fastest swimmers in the ocean, and their skin is covered in tiny, grooved structures known as riblets. These riblets reduce drag by controlling the turbulent boundary layer of water that flows over their bodies, allowing them to swim efficiently with minimal resistance. Researchers have applied this concept to the design of aircraft surfaces, maritime vessels, and even swimsuits to reduce drag and improve fuel efficiency. In aviation (fig I.11), riblet films applied to the surfaces of aircraft can result in drag reduction, leading to lower fuel consumption and enhanced performance. Studies have shown that these riblet surfaces can reduce skin friction drag by as much as 10%, making them a promising solution for improving the aerodynamic performance of high-speed vehicles and vessels.

FIGURE I.11: Aeroshark - Lufthansa Group Innovation Runway

Aircraft	**Drag Reduction and Benefits**	**Fuel Savings**	**Emission Reduction**	**Cost Savings**
Boeing 747-400	0.8% drag reduction confirmed for one Boeing 747-400, per annum:	approx. 300 t	> 900 t	> €160,000
Boeing 777F	Expected 1% drag reduction on each Boeing 777F, per annum:	370 t	1,170 t	> €200,000
Global Fleet	Estimated potential for the global commercial fleet at 1% drag reduction, per annum:	2 m. t	6.3 m. t	approx. €1 bn

TABLE I.1: The AeroSHARK Effect: Comparative Benefits of Drag Reduction on Aircraft

The riblet film technology can be applied to any aircraft, with significant advantages in terms of efficiency. The film weighs approximately 180 g/m^2, ensuring it does not add considerable load to the aircraft. It offers durability of more than four years and demonstrates a return on investment (ROI) within less than two years, making it a highly cost-effective solution for commercial fleets.

[17]

I.19.2 Humpback Whale Tubercles

Another remarkable bio-inspired flow control technique comes from the study of humpback whales (figI.12). The leading edges of the whale's flippers feature bumpy, uneven ridges called tubercles, which help the massive mammals maneuver gracefully through water. These tubercles delay flow separation along the leading edge of the whale's flippers, allowing the whale to maintain lift at higher angles of attack and reduce drag during tight turns. Engineers have translated this natural design into the development of airfoils for wind turbines, aircraft wings, and underwater vehicles. By incorporating tubercles along the leading edge of airfoils, researchers have been able to enhance the lift and reduce the drag of these structures, particularly at high angles of attack. This improvement allows for greater control, efficiency, and stability in the operation of wind turbines, helping them perform better in low wind conditions and withstand turbulent flows. [24]

I.19.3 Insect Wing Corrugation

The wings of insects such as dragonflies and bees provide another example of bio-inspired flow control. These wings are not smooth like those of birds but instead feature corrugated surfaces. The corrugations allow insects to maintain lift and maneuverability even at low Reynolds numbers, where airflow is typically more unsteady and prone to separation.

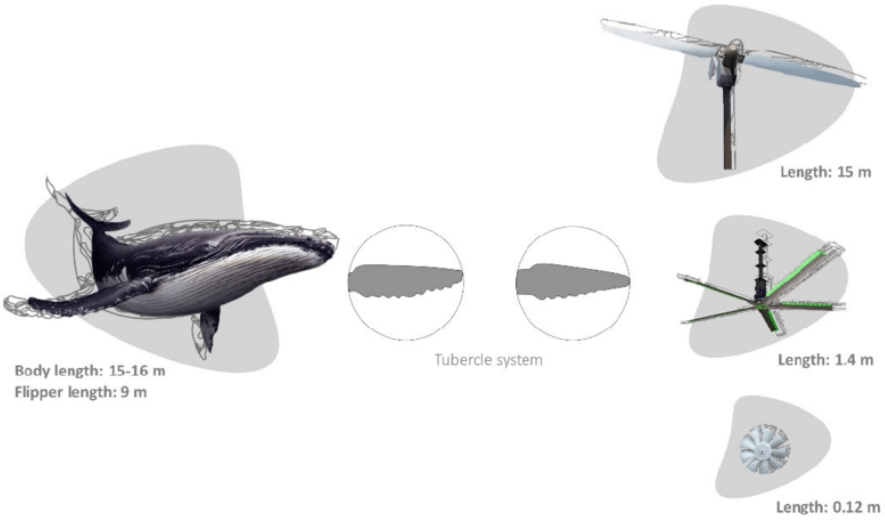

FIGURE I.12: Biomimetic scaling of the tubercle effect. Tubercle system of humpback whale fin provided several bio-inspired designs at different dimensional scales: Wind turbine blade (15 m), indoor ventilation fans (1.40 m) and fans (12 cm) developed by the Whalepower Corporation. Images adapted from

The corrugation on insect wings provides a lightweight, stiff structure that maximizes lift while minimizing drag. This design has inspired engineers to create corrugated airfoils for micro air vehicles (MAVs) and drones, which operate at low Reynolds numbers similar to those of insects. By mimicking the natural structure of insect wings, these vehicles can achieve enhanced stability and aerodynamic performance, making them more efficient and capable of functioning in complex environments, such as urban areas or tight spaces.

I.19.4 Bird Feather Aerodynamics

Birds offer yet another source of inspiration for flow control, particularly through the study of their feathers. During flight, birds can adjust their feathers to optimize lift and reduce drag. For instance, during landing, many birds raise their wing feathers to create slots that increase the airflow over the wing, delaying flow separation and increasing lift at lower speeds. This technique allows birds to land with precision and minimal energy expenditure. Aircraft designers have incorporated similar slot mechanisms into modern airplane wings, particularly through the use of leading-edge slats and trailing-edge flaps. These devices enhance the lift generated by the wing, especially during takeoff and landing when additional lift is needed. By controlling the airflow over the wings, engineers can improve the aircraft's performance and safety during critical flight maneuvers.

I.19.5 Penguin Air Bubble Shedding

Penguins, renowned for their agile swimming abilities, provide another bio-inspired innovation in flow control. When penguins swim at high speeds, they release air bubbles trapped in their feathers, creating a lubricating layer of air between their bodies and the water. This technique drastically reduces frictional drag, allowing penguins to reach speeds much higher than would otherwise be possible. Inspired by this natural phenomenon, researchers have investigated the use of air bubbles for drag reduction in ships and submarines. By introducing micro-bubbles into the boundary layer, engineers can reduce the frictional resistance of water flowing over the surface of the vessel. This technique has been found to reduce drag by as much as 80% in some cases, resulting in significant energy savings for marine transportation.

I.19.6 Lotus Leaf and Superhydrophobic Surfaces

The lotus leaf is another example from nature that has inspired advances in flow control, particularly in the development of superhydrophobic surfaces. The surface of the lotus leaf is covered in microscopic structures that create a highly water-repellent, self-cleaning surface. When water droplets land on a lotus leaf, they form nearly spherical beads that roll off the surface, taking dirt and debris with them. This natural property has inspired the creation of artificial superhydrophobic surfaces, which have applications in reducing drag in both air and water. In aerodynamics, superhydrophobic coatings have been used to reduce skin friction drag by minimizing the wetted surface area, thus decreasing the resistance faced by vehicles traveling through air or water. These coatings are also valuable in creating low-maintenance surfaces that resist contamination and corrosion, further improving the efficiency and lifespan of vehicles and machinery.

I.19.7 Mechanosensors and Turbulence Detection in Eagles

The mechanosensors in eagles' wings (shown in figI.13) are an exceptional adaptation that enhances their flight capabilities. Located at the base of their feathers, these sensors are sensitive to changes in air pressure, shear forces, and flow dynamics, allowing the eagle to precisely detect even minor fluctuations in turbulence. This sensitivity is crucial for maintaining stability during flight, especially in turbulent conditions or when navigating through rapid changes in air currents.

For instance, when airflow separates or becomes turbulent, the mechanosensors detect these shifts and trigger an immediate response. The eagle can then adjust the position and orientation of its feathers, optimizing the aerodynamic profile of its wings. By aligning the feathers to reduce drag and optimize lift, the eagle can fly more efficiently, even under challenging conditions like gusty winds or while performing high-speed maneuvers.

This ability to respond dynamically to mechanical stimuli ensures that eagles can maintain control and adapt swiftly to environmental changes, which is essential for hunting, migrating, and avoiding predators. These sensory systems play a significant role in the eagle's flight performance, offering a level of precision that few other animals can achieve.[21].

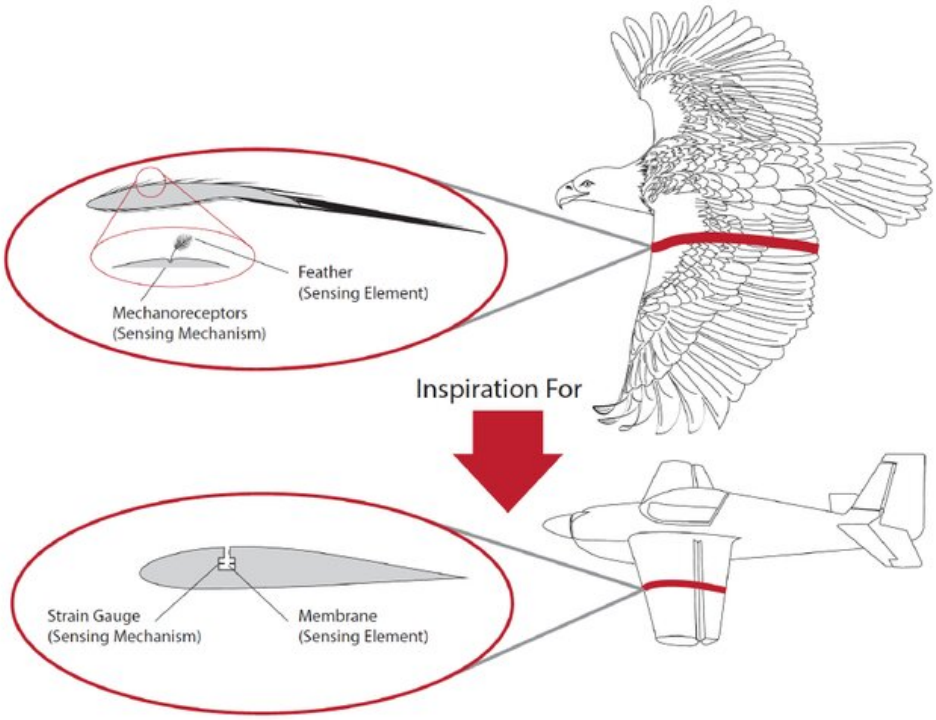

FIGURE I.13: o-inspired pressure sensing for MAV attitude control.

I.19.8 Bio-Inspired Flow Control Applications

Inspired by this natural phenomenon, our engineering work leverages the concept of mechanosensors to develop advanced systems for detecting turbulence and flow separation. The eagle's ability to detect and react to changes in airflow has informed the design of artificial sensors that mimic these biological mechanisms. By placing sensors along surfaces such as wings or fuselages, we aim to monitor air pressure and flow dynamics in real-time, much like how an eagle senses the air passing over its wings. These bio-inspired mechanosensor systems can detect separated flow, boundary layer behavior, and fluctuations in wall pressure, providing essential data for real-time adjustments to aerodynamic control systems. This real-time feedback enables engineers to develop more adaptive flow control strategies that improve stability, reduce drag, and enhance overall performance in both aircraft and other aerodynamic applications.

I.19.9 Dynamic of Separated Flow and Wall Pressure Measurement

In fluid dynamics, separated flow occurs when the boundary layer detaches from the surface of a wing or fuselage, leading to unstable flow conditions, turbulence, and increased drag. Understanding the dynamics of separated flow is critical for optimizing the aerodynamic performance of vehicles. To achieve this, we use wall pressure sensors, inspired by

the eagle's mechanosensors, to monitor pressure variations in real-time and detect the onset of flow separation. These wall pressure sensors are embedded in aerodynamic surfaces and measure the variations in pressure caused by changes in airflow behavior. By detecting the regions of separated flow, engineers can implement active flow control strategies, such as synthetic jets or plasma actuators, to reattach the boundary layer and maintain smooth, streamlined flow. This approach is directly inspired by how eagles adjust their wing feathers to respond to changes in the air around them. With real-time wall pressure data, we can effectively manage flow separation, reduce drag, and increase lift, much like how eagles dynamically optimize their flight to handle turbulence. The combination of advanced sensor technologies and bio-inspired control strategies marks a significant step forward in modern aerodynamic design, enabling more efficient and adaptive systems.

By drawing inspiration from the natural flight mechanisms of eagles, particularly their use of mechanosensors to detect turbulence, we have developed innovative flow control systems that mimic these biological processes. The application of real-time wall pressure measurement and active flow control techniques allows for improved performance, reduced fuel consumption, and greater stability in aircraft and other aerodynamic systems.

II Numerical Characterization for Separated Flow over BFS

Chapter abstract

This chapter outlines the approach taken to simulate this complex flow phenomenon, including the hypotheses formulated to guide our modeling process and the numerical techniques employed to capture the turbulent behavior and separation effects accurately. The model's validity is tested against experimental data, allowing us to assess the accuracy and reliability of our simulations in reproducing critical flow characteristics observed in BFS scenarios. This section provides a detailed account of our methodology, assumptions, and the comparative analysis with experimental results, serving as a foundation for our investigation into BFS turbulent flows.

II.1 Introduction

We focused on studying the flow over a (BFS) in a turbulent regime at $Re_h = 89100$. The BFS is the most preferred geometry in academic and industrial studies of the separated flow for its simplicity, (Duriez et al., n.d.) and it offers adequate conditions to create the separation by geometric rupture by studding it with an angle of 90°. (Antonio Lacerda De Brederode, 1972.) focused on the aspect ratio for BFS (AR=the wide of the test section/high step). They conclude that an aspect ratio greater than ten results in a two-dimensional flow, as the effect of side walls becomes negligible. Also, (Ötügen, 1991) studied the influence of the expansion ratio (ER = high of test section / (high of test section - high step)) on organized structures. (Sujar Garrido et al.,2014.) assured that BFS depends on two parameters: flow conditions (boundary layer, turbulence) and geometric ones (ER and AR). (Chovet et al., 2017) worked on BFS with an effective nominal two-dimensional flow with an ER = 1.04 and AR = 24, resulting in negligible inference of the upper wall and side walls, and we conducted our research under the same conditions as (Chovet et al., 2017). And we assessed the DES model's accuracy in capturing turbulent flow dynamics, downstream of the BFS. Specifically,we ensure the accuracy of

our numerical data by validating it through experiments conducted under the same operating and geometrical conditions. More recent advancements in the field have focused on numerical simulations and high-fidelity modeling. Le et al. (1997) used direct numerical simulation (DNS) to study turbulent flow over a BFS. Their results offered a detailed view of the flow structures, including vortex shedding and turbulent reattachment. This work demonstrated the power of computational techniques in resolving small-scale features of the flow, furthering our understanding of separation dynamics. In addition, Ryu and Sung (2006) performed large-eddy simulations (LES) on BFS flows, comparing the results to experimental data. Their work revealed insights into how turbulent eddies and flow instabilities affect reattachment lengths and vortex formation. LES has since become a widely accepted tool for simulating turbulent separated flows, providing a bridge between DNS and traditional Reynolds-Averaged Navier-Stokes (RANS) models. In conclusion, the backward-facing step remains a critical geometry for studying separated flow, particularly in turbulent regimes. Numerous studies have explored the effects of aspect ratio, expansion ratio, and flow conditions on the separation and reattachment processes. With the continued use of experimental techniques and advances in computational fluid dynamics (CFD), future research promises to further refine our understanding of flow separation over complex geometries like the BFS.

II.2 NUMERICAL MODELING

II.2.1 Hypotheses

Before conducting any numerical simulation, it is essential to formulate our hypothesis, which serves as the foundation for our research to draw meaningful conclusions. As we are working under the same operating conditions as [5] (experimental), we suppose that:

- Two-dimensional flow: When the aspect ratio is greater than ten [3], the flow is predominantly two-dimensional, and the transversal dynamics become negligible, effectively minimizing the effects of the side walls. In addition, our study aims to establish a closed-loop control system capable of predicting and managing the most significant flow dynamics. To achieve this, we focused on the longitudinal and normal dynamics where the most critical flow behaviors are observed in experiments. Consequently, we opted for two-dimensional simulations, as the transversal dynamics are less significant in our case.
- Walls are adiabatic.
- The fluid is air with a density of $1.225\,\mathrm{kg/m^3}$ and a dynamic viscosity of $1.7894 \times 10^{-5}\,\mathrm{kg/(m \cdot s)}$.
- Incompressible flow.
- Isothermal flow (experimental work was conducted at a fixed temperature).
- Turbulent flow at $\mathrm{Re_h} = 89100$ and $\mathrm{Re_h} = 31500$ for comparison with experimental wall pressure coefficients.

- Turbulent intensity equals 0.6% (as measured in experimental conditions).
- Boundary layer thickness measured at $0.2h$ before the backward-facing step (BFS), $\delta/h = 0.5060$ (as measured in experimental work, showing equivalent values at the same location).

II.2.2 Simulation domain

We conducted our simulation using the same geometrical and operating conditions, as those employed in the experiments at (Chovet et al., 2019), we worked with the height step value, h = 0.083 m as shown in fig II.1.

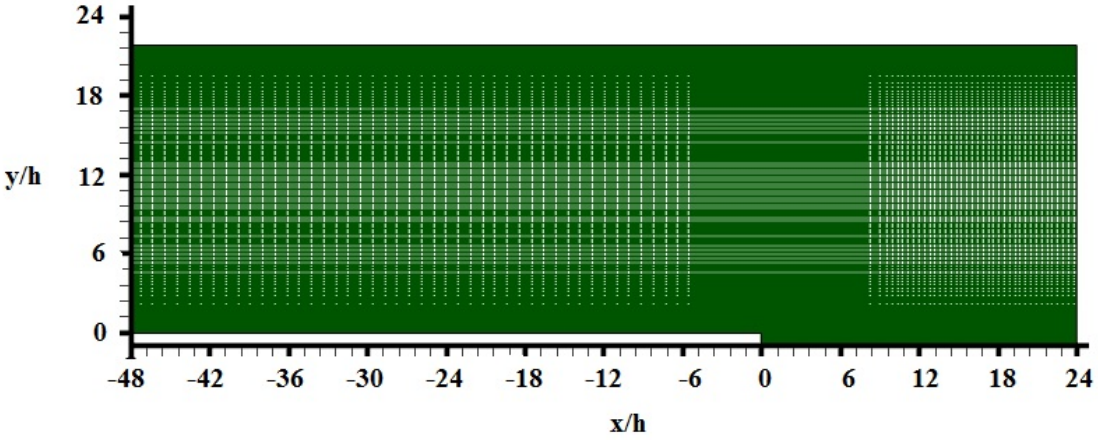

FIGURE II.1: Computational Domain with Coordinates

II.2.3 Meshing

In our case, the geometry is not complex, and we chose a structured mesh for our study without hesitation. In 2D, the elements are quadrilaterals, as shown in fig II.2, and this approach offers the following advantages:

- Economic in terms of the number of elements, as it presents a lower number of cells compared to an equivalent unstructured mesh.
- When the mean flow is aligned with the mesh, a structured mesh reduces the risk of numerical errors.

We refined the mesh near both the vertical and horizontal walls. This type of meshing is widely used in the literature for backward-facing step (BFS) geometries as well as for vertical and horizontal walls, such as in the meshing over two inline square cylinders [30]. To accurately capture the boundary layer, we employed the y^+ approach to achieve an appropriate wall resolution, targeting a value of $y^+ = 1$ to ensure that the mesh resolves the viscous sublayer in all cases. Additionally, all meshes were generated by varying the cell-to-cell growth ratio, as shown in fig II.3 at the BFS corner. The choice

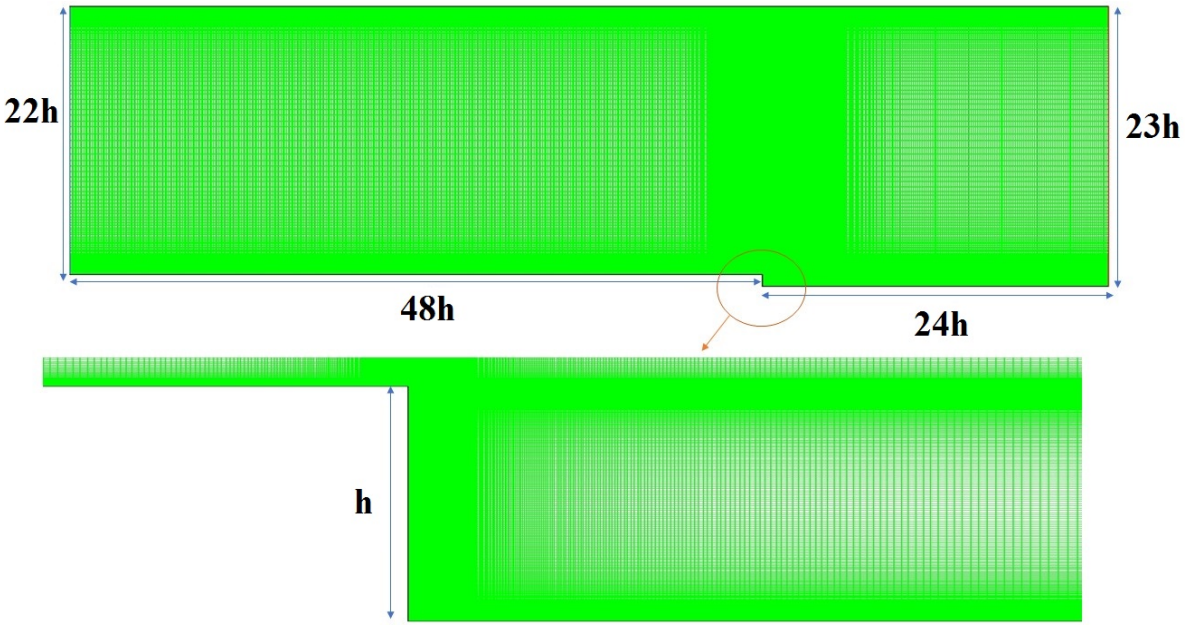

FIGURE II.2: Visualization of Mesh within the Computational Domain.

of mesh size is crucial to balancing accuracy and computational efficiency. Therefore, we conducted a sensitivity analysis to determine the optimal mesh size for our simulations. We assessed the mesh quality using various criteria, including skewness, aspect ratio, and orthogonality. We achieved a high-quality mesh with smooth transitions between the different zones, ensuring accurate numerical predictions of the flow dynamics over the BFS.

In fig II.4, the plot shows how the viscous coefficient changes with the number of nodes used in the meshing. Initially, the viscous coefficient fluctuates significantly as the number of nodes increases, indicating a lack of convergence. At around 580,000 nodes, the viscous coefficient stabilizes and shows minimal variation with further increases in the number of nodes, indicating that the solution has reached a converged state where further refinement does not significantly affect the results. Fig II.5 illustrates the wall shear stress downstream of the BFS, plotted against x/h for various mesh resolutions. It offers insights into the internal and external reattachment lengths, with reattachment points identified by values approaching zero, indicating where the flow reattaches after separation. The dashed lines indicate experimental values for $x/h = 0.71$ (Xr in experiment) and $x/h = 5.37$ (Lr in experiment). As the mesh resolution increases, the curves converge, becoming closer to the experimental values. Meshes with more than 550,000 nodes are particularly well-aligned and closely match the experimental values at both Xr and Lr.
Consequently, selecting 580,000 nodes offers a good balance between computational cost and accuracy, as this choice is informed by the stabilization of both the viscous coefficient and the convergence of wall shear stress values, making it the optimal mesh resolution for this study.

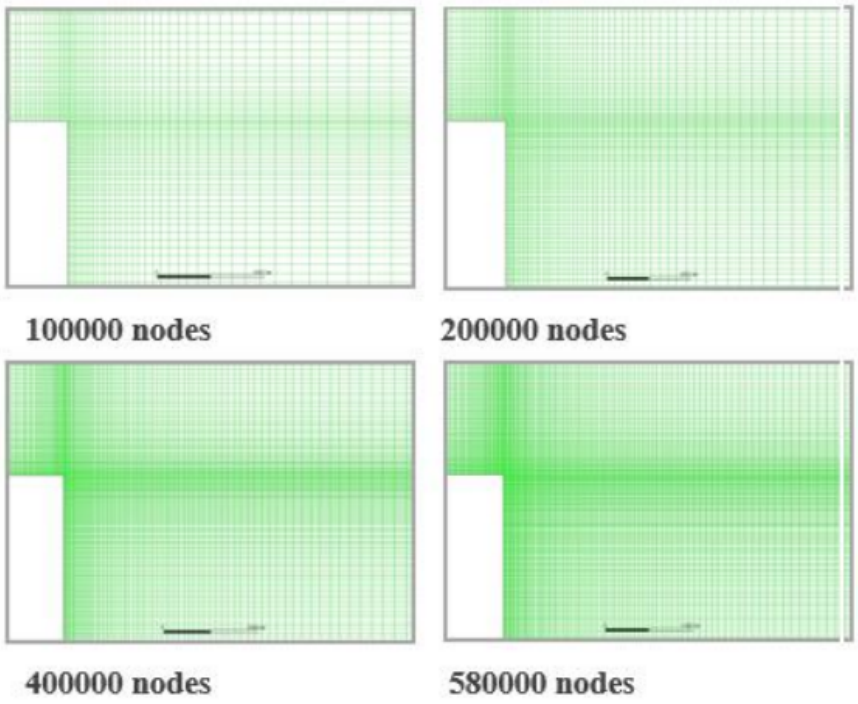

FIGURE II.3: Examples of Analyzed Meshes

FIGURE II.4: Meshing Independence study using viscous coefficient.

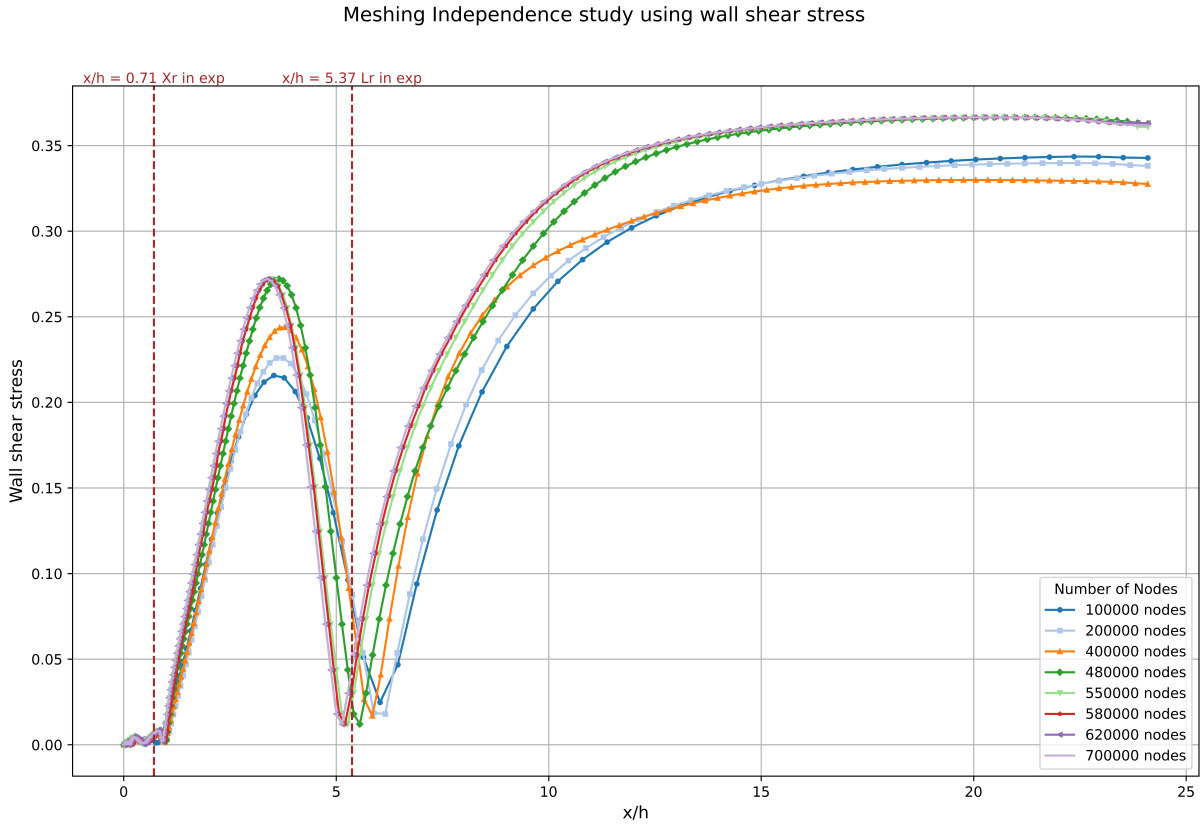

FIGURE II.5: Meshing Independence study using wall shear stress.

II.2.4 Numerical Models

To perform simulations in our study, we used *Ansys Fluent* due to its versatility and wide range of available numerical models, with finite volume discretization. The momentum equations were solved using the MUSCL third-order scheme, while the other equations were solved using second-order schemes. Additionally, residual values were set to 10^{-6} for better precision, ensuring higher accuracy in the numerical solutions. In the context of 2D unsteady isothermal flow, the governing equations consist of the continuity equation for mass conservation and the momentum equations. The continuity equation ensures that mass is conserved in the flow, and it can be expressed as: **Continuity Equation (Mass Conservation)**

$$\frac{\partial u}{\partial x} + \frac{\partial v}{\partial y} = 0 \tag{II.1}$$

The momentum equations, which describe the forces acting on the fluid, are essential for capturing the dynamics of the flow. **Momentum Equations**

- **x-momentum Equation**

$$\frac{\partial u}{\partial t} + u\frac{\partial u}{\partial x} + v\frac{\partial u}{\partial y} = -\frac{1}{\rho}\frac{\partial p}{\partial x} + \nu\left(\frac{\partial^2 u}{\partial x^2} + \frac{\partial^2 u}{\partial y^2}\right) \tag{II.2}$$

- **y-momentum Equation**

$$\frac{\partial v}{\partial t} + u\frac{\partial v}{\partial x} + v\frac{\partial v}{\partial y} = -\frac{1}{\rho}\frac{\partial p}{\partial y} + \nu\left(\frac{\partial^2 v}{\partial x^2} + \frac{\partial^2 v}{\partial y^2}\right) \tag{II.3}$$

Choosing the appropriate turbulence model is especially important, as turbulence plays a crucial role in many fluid flows. However, selecting a more complex model may not always lead to better results, as it may require more computational resources and time. Overall, a systematic approach that considers the physical phenomena being studied, and the available computational resources is necessary to select an adequate numerical model. Several researchers have investigated different turbulence models to reproduce the important flow features on BFS, observed in the experiments. [26] conducted a study on Large Eddy Simulation (LES), Detached Eddy Simulation (DES), and the Reynolds Stress Model (RSM). They concluded that while LES and DES are the most accurate, RSM also has positive aspects, particularly in handling complex three-dimensional flows and capturing anisotropic turbulence effects. Also, [20] used the LES model to show the influence of a periodic perturbation on BFS. [18] found that partially averaged Navier-Stokes (PANS) gives acceptable predictions in BFS but is less accurate than the DES model. Additionally, the study by [25] on separation behind the BFS showed that DES variants agree well with measured skin friction and velocity profiles when a sufficiently fine mesh is applied, unlike RSM. [2] found that the Transition-SST model effectively captures the laminar-turbulent transition, providing accurate predictions in flow separation scenarios. [29] concluded that the Improved Delayed Detached Eddy Simulation (IDDES) model offers significant improvements over traditional DES and RANS models, particularly in predicting heat transfer and reattachment lengths in BFS flows. Other models designed to include laminar-turbulent transition and separation, such as Gamma-Reynolds and RMS, also offer significant potential for accurately predicting flow characteristics in BFS scenarios. These models account for the transition between laminar and turbulent flow, providing more comprehensive results in certain conditions. These findings demonstrate the importance of selecting an appropriate turbulence model based on the flow characteristics and objectives of the simulation. **DES (Detached Eddy Simulation)** DES is a hybrid turbulence model that combines the benefits of Reynolds-Averaged Navier-Stokes (RANS) and Large Eddy Simulation (LES) models. The DES model uses RANS equations in the near-wall regions and switches to LES equations in the outer regions by a comparison of the turbulent length scale L_t with the grid spacing $\Delta_{\max}$. The model selects the minimum of both and switches between RANS and LES mode by replacing ϵ in the k-equation by:

$$\epsilon = \frac{k^{3/2}}{L_t} \rightarrow \epsilon = \frac{k^{3/2}}{\min(C_{DES}\Delta_{\max}, L_t)} \tag{II.4}$$

The modified equation ensures a smooth transition between the RANS and LES regions in hybrid turbulence models. In regions where the grid is fine, the LES approach dominates, while in coarser grid regions, the RANS approach is used. This allows for better prediction of both attached and separated flows, making it a popular choice for simulating complex flow phenomena. The DES model involves solving a modified set of Navier-Stokes equations, which account for the effects of turbulence on the flow.

II.2.5 Numerical Modeling Results

Flow Topology

The results using the DES model at $Re_h = 89100$ from the simulation are in good agreement with the experimental data (EXP), particularly in the external reattachment length (L_r), and internal separation length (X_r), as presented in Table II.1. In fig II.6, the

Models	EXP	DES Mean Values
L_r/h	5.37	5.2870
X_r/h	0.71	0.6820
δ/h	0.53	0.5010

TABLE II.1: Comparison between experimental and numerical reattachment length.

X velocity contours show that the BFS creates a recirculation zone downstream of the step, characterized by negative velocities. After the reattachment point, a new boundary layer forms, and the velocity becomes positive again, indicating the recovery of the flow. These negative velocities in the recirculation zone and subsequent recovery of the flow are common features observed in the flow past a BFS. Additionally, in fig II.7 (Y velocity), we see that after the sudden expansion followed by a contraction, separation is induced, leading to the formation of a recirculation zone downstream of the step. Negative normal velocities are observed in this recirculation zone, causing boundary layer separation and the formation of a shear layer at the edge of the step. This shear layer is susceptible to various types of instabilities, such as vortex shedding. In unsteady flows past a BFS, the dynamics of the shear layer and the formation of vortices oscillate over time due to flow unsteadiness, which can be observed as fluctuations in the velocity vectors. The formation and shedding of vortices, which can interact with the channel walls, result in a recirculation zone downstream of the step.

Fig II.8 displays the unsteady velocity magnitude over time in a flow over a backward-facing step (BFS). The velocity magnitudes are shown with color variations, from low (purple) to high (yellow), allowing visualization of fluctuations in flow velocity and patterns of recirculation and separation. In each plot, the flow dynamics near the step demonstrate a region of increased velocity magnitude downstream, where the flow detaches and reattaches. The high-velocity zones in yellow indicate regions where the flow accelerates after separation. These regions appear consistently downstream of the step, highlighting turbulent mixing and unsteady flow behavior, while the purple areas closer to the step and below it show zones of lower velocity, likely due to recirculation and separation effects caused by the BFS. The differences among the three frames suggest the unsteady nature of the flow, with subtle shifts in the position and intensity of the high-velocity areas. These fluctuations are characteristic of turbulent flow over a BFS, where the fluid dynamically interacts with the geometric change, leading to periodic changes in flow separation, reattachment, and vortex formation. This sequence of plots, representing different instances in time, provides insight into the temporal variations in velocity

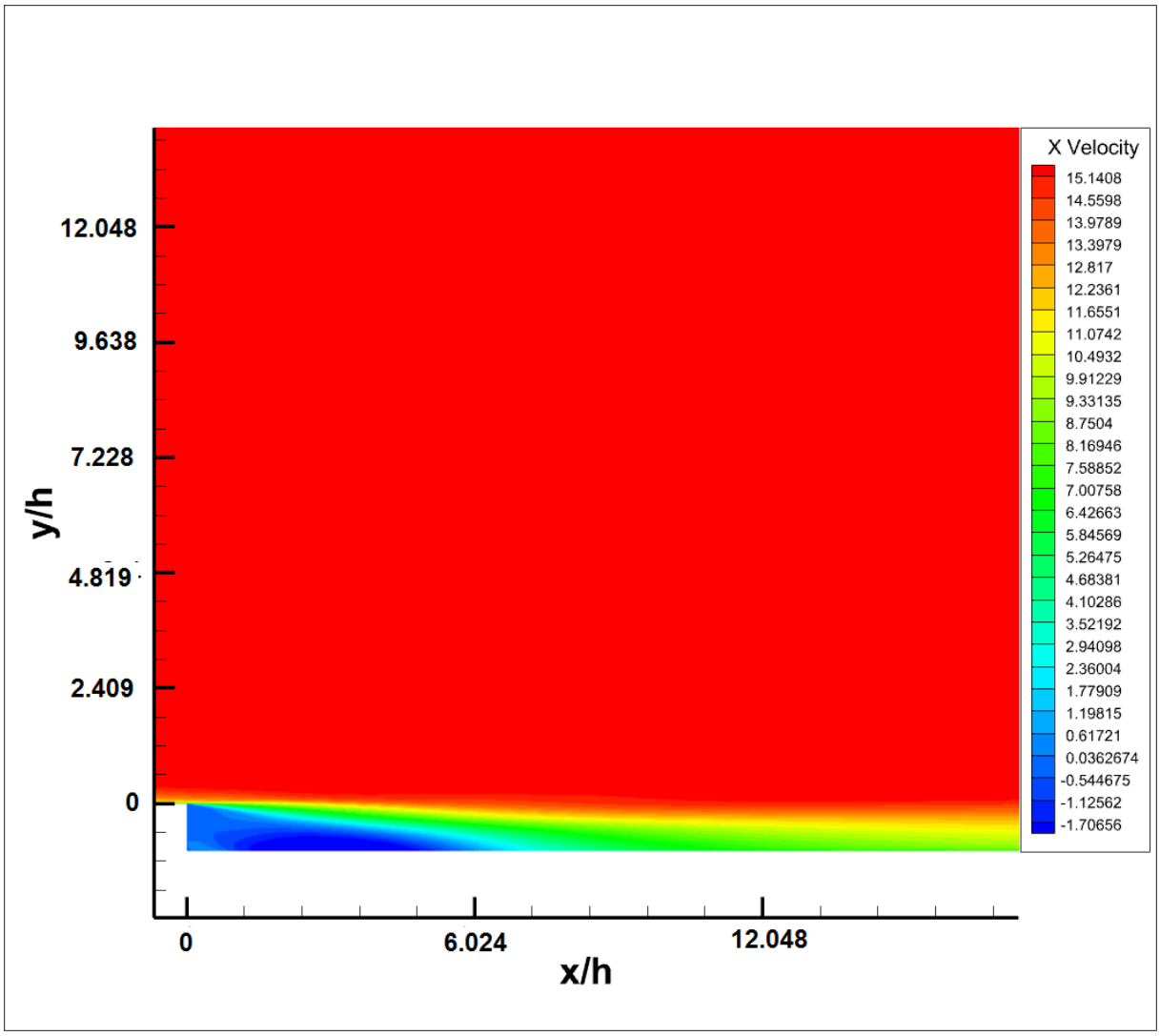

FIGURE II.6: Contour of mean flow longitudinal velocity

magnitude, capturing the dynamic evolution of the flow structure over the BFS and illustrating how velocity and recirculation zones change in response to the unsteady flow conditions. Fig II.9 represents the contour of vorticity magnitude over a (BFS) reveals the distribution and intensity of rotational flow effects as fluid flows over the step. The color bar on the right indicates the vorticity magnitude, with values ranging from low (blue) to high (red). The flow shows low vorticity across most of the domain, represented by the broad blue area, suggesting a stable flow far from the step. However, near the bottom left, where the flow interacts with the step, we observe a rapid transition from blue to green and even red, indicating high vorticity zones. This region of increased vorticity is typical over a BFS, as the sudden change in geometry causes flow separation and recirculation. These high-vorticity zones highlight the shear layers and turbulent effects immediately downstream of the step, where the fluid adjusts to the change in boundary conditions, creating vortices and rotational motion. This vorticity distribution is crucial for understanding flow dynamics over the BFS, especially in predicting areas of instability

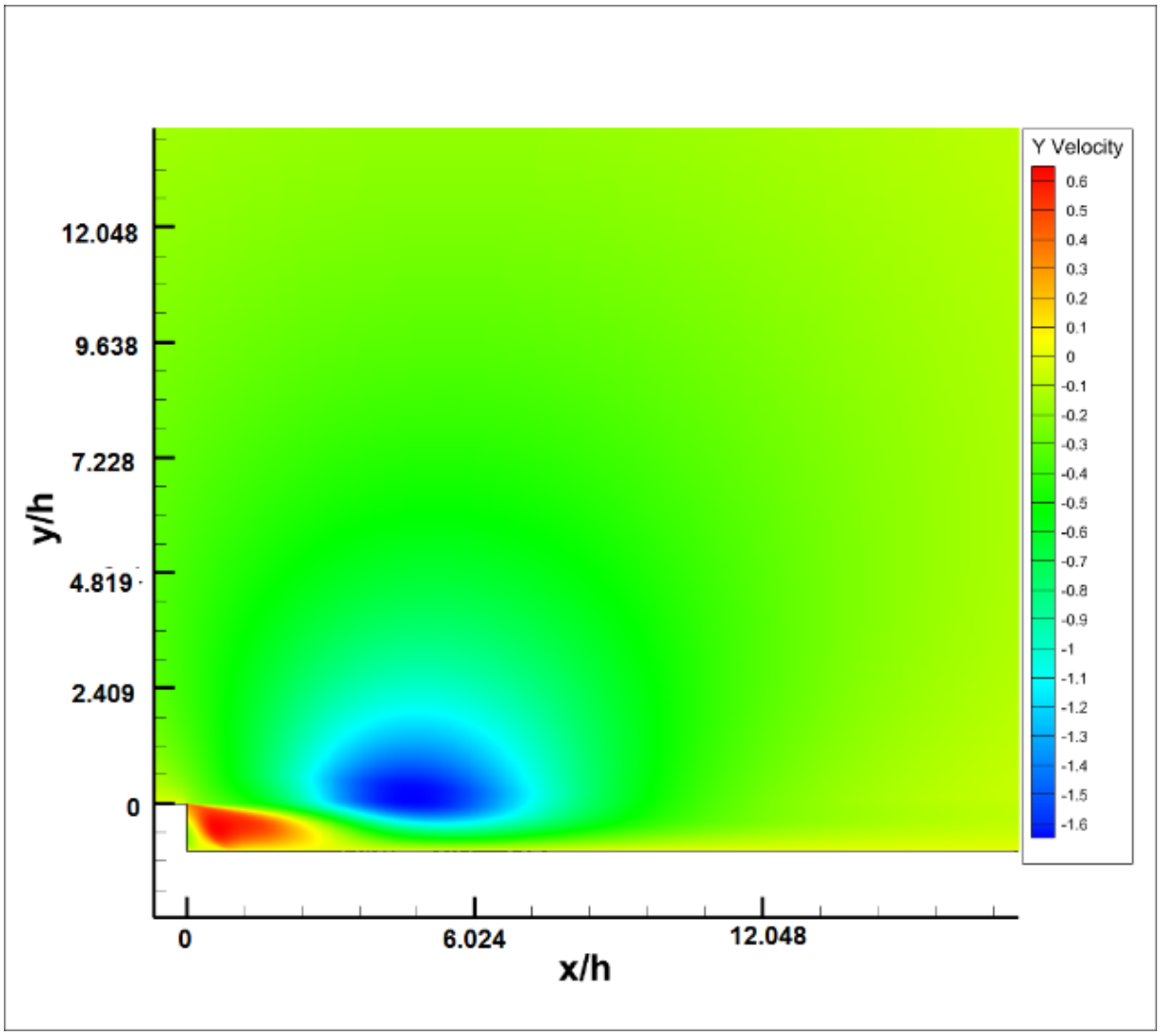

FIGURE II.7: Contour of mean flow normal velocity

and the potential for turbulent mixing near the step. The two contour plots depict the production and dissipation rates of turbulent kinetic energy (k) over a (BFS), highlighting the regions of energy generation and loss within the flow field.

Fig II.11, which shows the production of k, we see a concentration of production near the step at the lower left, where the flow encounters the geometric discontinuity. This region, indicated by the transition from blue to green and then yellow, suggests that the turbulent kinetic energy is being generated due to shear forces as the flow interacts with the step and reattaches downstream. The high production here aligns with areas of flow separation and recirculation typical in BFS geometries, marking the origin of turbulence in this scenario.

Fig II.10 shows the dissipation rate of k, denoted as epsilon (ϵ), which represents the rate at which turbulent kinetic energy is converted into thermal energy and lost from the system. Similar to the production plot, the dissipation rate is concentrated near the step

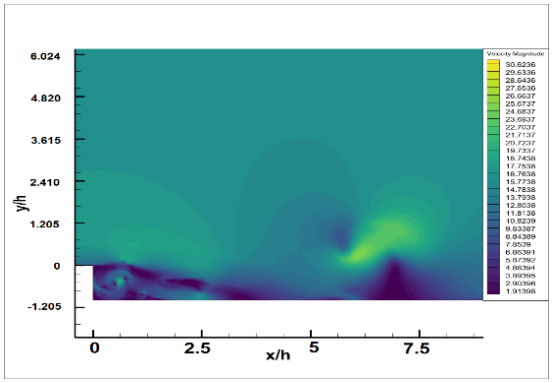

(A) Magnitude velocity at 0.550122s

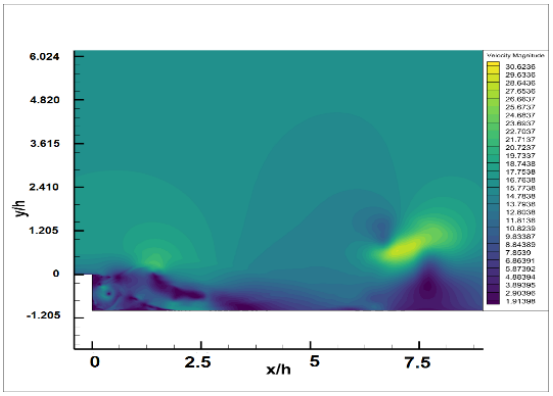

(D) Magnitude velocity at 0.55509s

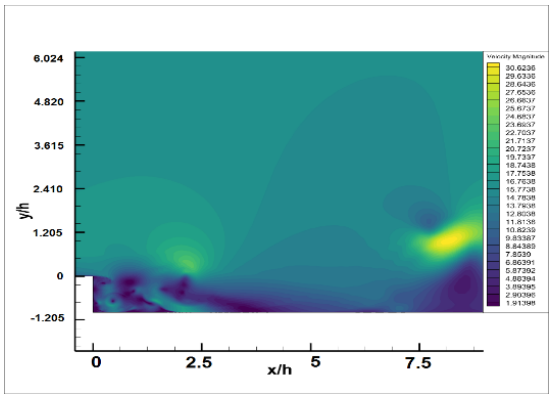

(B) Magnitude velocity at 0.56058s

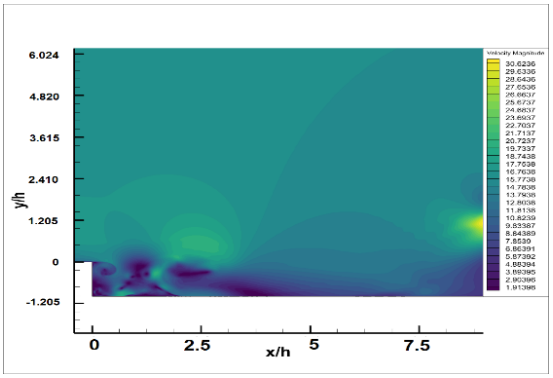

(E) Magnitude velocity at 0.565025s

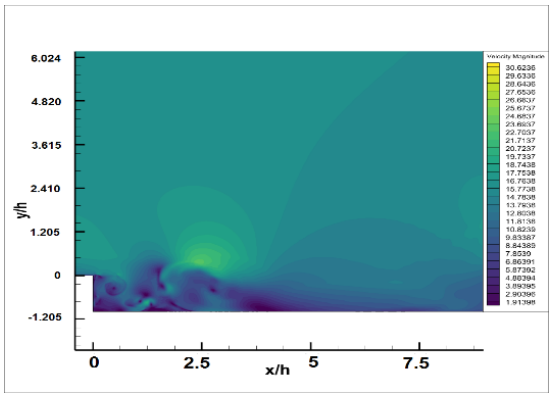

(C) Magnitude velocity at 0.570447s

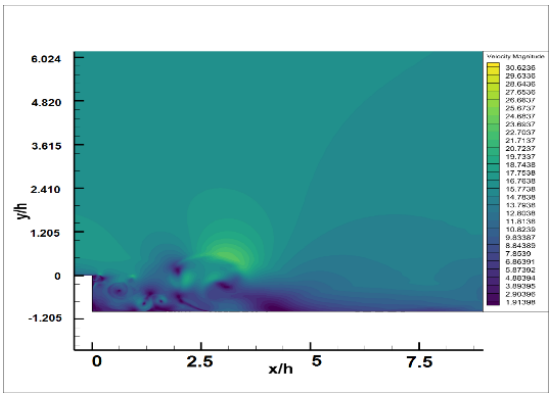

(F) Magnitude velocity at 0.575415s

FIGURE II.8: Snapshots of Instantaneous Magnitude Velocity at Different Time Instants, Showing Dynamic Behavior over BFS

and decreases as we move downstream. The transition from blue to green and yellow close to the step boundary indicates areas of intense turbulent energy dissipation, where energy transfer from larger turbulent eddies to smaller scales eventually leads to viscous dissipation.

Together, these plots offer insights into the turbulent energy dynamics within the flow over the BFS. The proximity of high production and dissipation regions near the step shows the balance between energy generation due to flow interactions with the step and

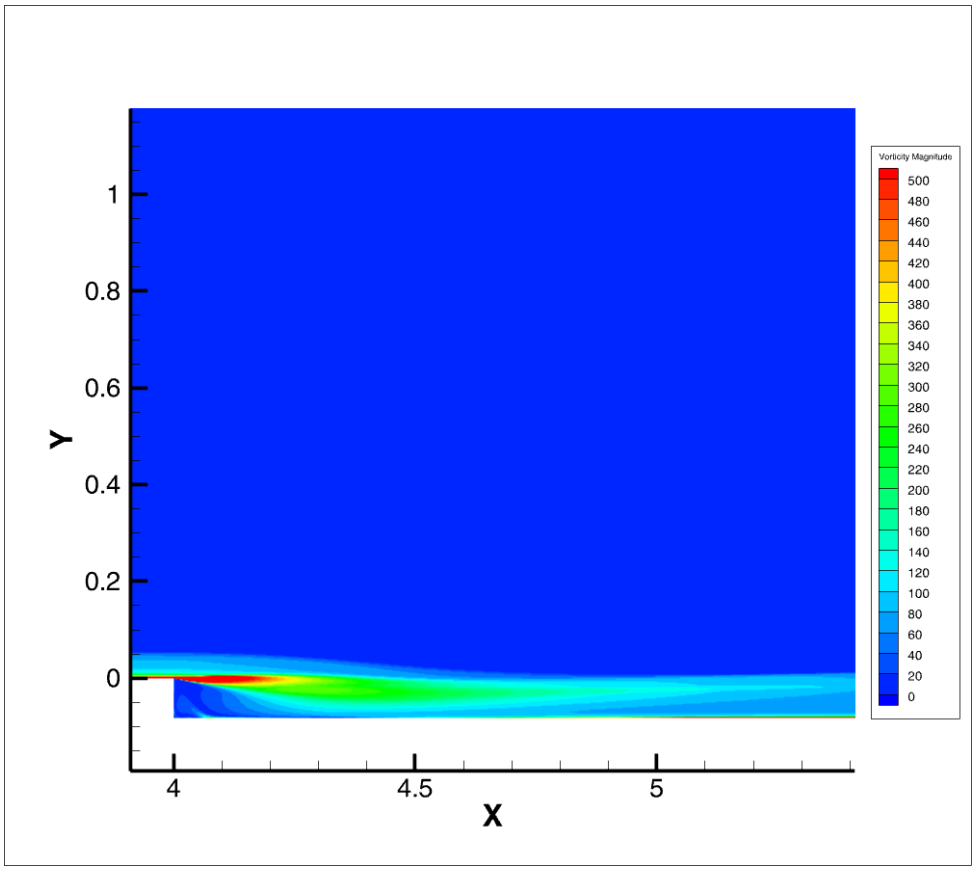

FIGURE II.9: Contours of mean vorticity magnitude

subsequent dissipation as turbulence is smoothed out, contributing to the stability of the downstream flow. This balance is crucial for understanding the nature of turbulence in separated flows and the efficiency of energy transfer within the fluid dynamics of this geometry. Fig II.12 illustrates the distribution of dynamic pressure across a region, with colors ranging from blue (low pressure) to red (high pressure) as indicated by the scale on the right. The lowest pressures, shown in blue, concentrate at the bottom left, suggesting a potential boundary or stagnation zone. As we move upward and to the right, dynamic pressure increases, transitioning through green, yellow, and finally into orange and red, which indicate high-pressure areas. The semi-circular patterns near the left side hint at regions of pressure waves or recirculating flow, while the sharp gradient from blue to green at the bottom highlights a boundary layer or a zone of rapid pressure change, suggesting complex flow dynamics in this region. This pressure distribution could reveal important insights into the flow behavior, especially in areas with steep gradients and high-pressure zones, which are key to understanding fluid behavior in the simulated or experimental setup.

Wall Pressure Coefficient

The coefficient of pressure (C_p) is a critical parameter in this study, highlighting the mean flow topology. We compared our results of the wall pressure coefficient after BFS with the

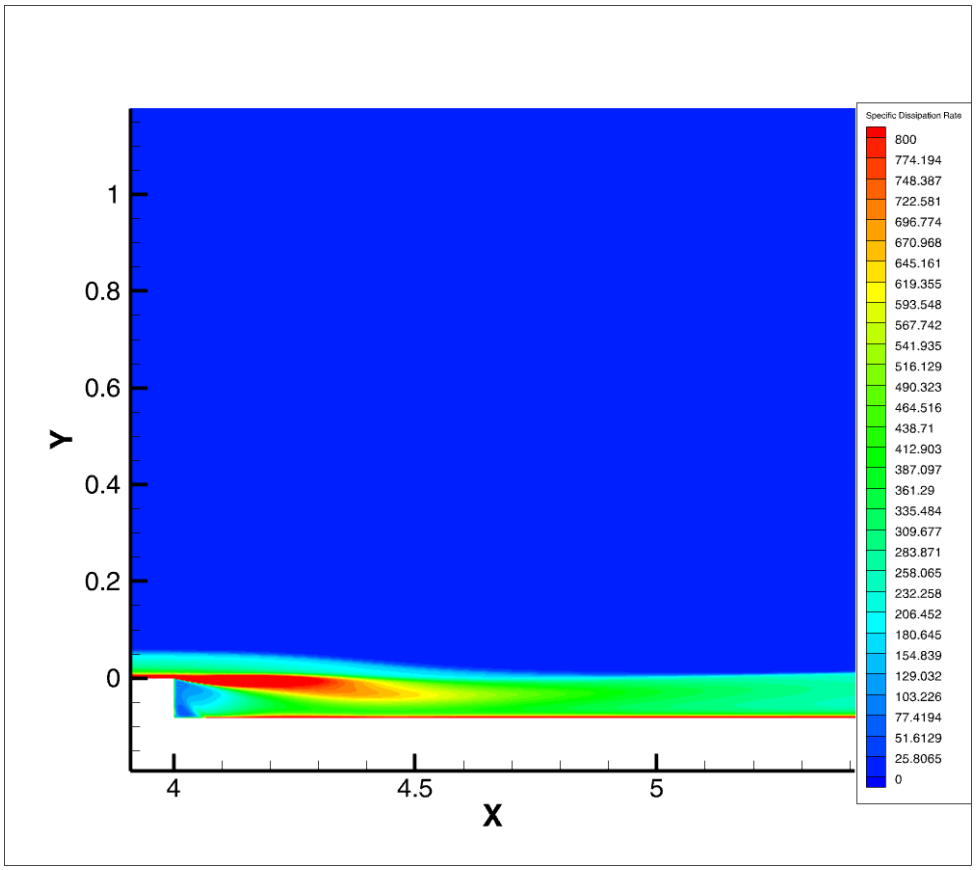

FIGURE II.10: Contours of desipation

experimental results measured by (Chovet et al., 2019) using 20 pressure sensors Kulite XCQ–062 at $Re_h = 31500$, shown in fig II.13. A low-pressure level was observed in both results. A zero value of C_p was noted at $x/h \approx 4$ for the experiment and near 3.5 for the DES model's mean values, with a maximum value of C_p near 0.25 for both results. After the external reattachment length of 5.62, the pressure gradient becomes adverse as the flow expands. The DES model effectively captures the overall trend and qualitative behavior of the flow, demonstrating its ability to detect depressions and the relationship between wall dynamics and flow characteristics. The strong qualitative agreement between numerical and experimental results suggests that the model accurately represents the essential physics of the flow.

II.3 Spectral analysis

Spectral analysis, particularly through the use of the Fast Fourier Transform (FFT), plays a vital role in fluid mechanics by allowing for the examination and decomposition of complex time-dependent or spatial signals into their fundamental frequency components. This method is crucial for identifying and quantifying periodic or quasi-periodic phenomena within fluid flows, such as vortices, pressure waves, and instabilities. For example, in oscillatory flows around bluff bodies like cylinders, periodic vortex shedding can create a

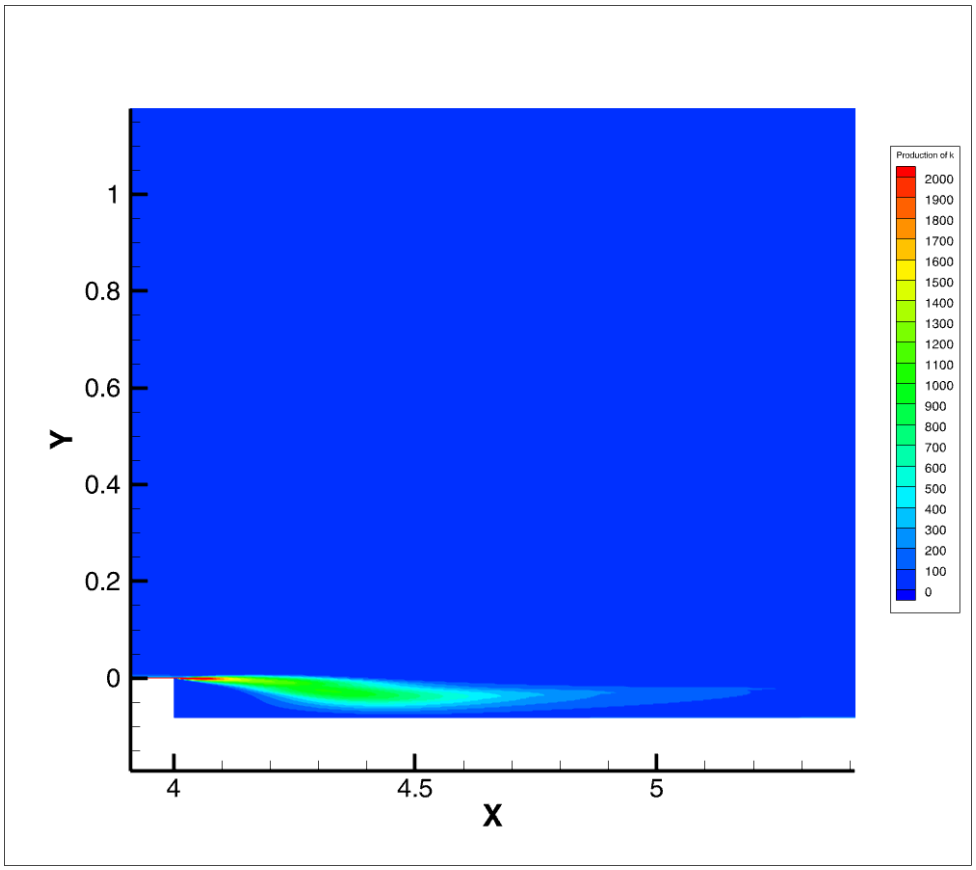

FIGURE II.11: Contours of production of k

Kármán vortex street. By applying FFT to experimental or numerical data, such as velocity or pressure time series, dominant frequencies associated with these flow structures can be identified. These periodic phenomena often manifest at specific frequencies, and analyzing them in the frequency domain helps researchers better understand the stability and nature of the flow. The FFT is particularly effective in quantifying periodic behavior by isolating energy peaks in the frequency spectrum, offering insight into how much of the flow's energy is carried by these periodic structures, which is crucial in the study of turbulent or transitional flows. When turbulence emerges, new frequency components appear, signaling the development of chaotic behavior. This is essential for understanding flow transitions and monitoring changes in the frequency spectrum. Moreover, FFT is widely used to analyze vortex shedding, aeroacoustics, and flow-induced vibrations, providing critical information for the design of structures and systems like bridges, wind turbines, and jet engines. One of the key benefits of FFT in fluid mechanics is its efficiency in handling large datasets, such as those generated in computational fluid dynamics (CFD), where time-dependent simulations produce vast amounts of data. By reducing complex flow behavior into simpler periodic components, FFT aids in the interpretation and quantification of flow dynamics, contributing to the advancement of more accurate models and predictions. Thus, FFT-based spectral analysis is indispensable for fluid mechanics researchers looking to decode periodic flow phenomena and apply that understanding to practical engineering solutions. The best region to show the low-pressure fluctuations,

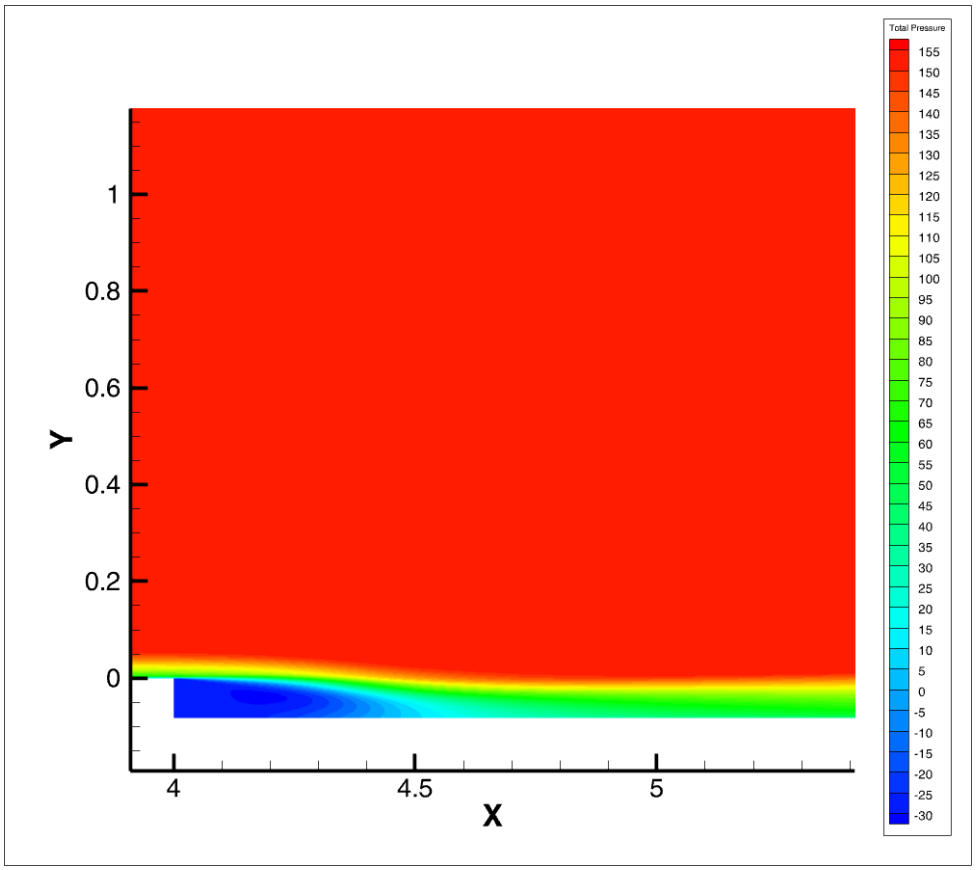

FIGURE II.12: Contours of total presssure

where the dynamic is dominated by both low and high frequencies, is at $x/L_r < 0.3$ or exactly at $x/h = 1.5$, under the shear layer, and we evaluated the wall pressure in this region. Our spectral analysis results, presented in Fig II.14, indicate the presence of two distinct instabilities in the flow past the studied object. The first instability, visible as a peak marked with a green cross in the plot, is characterized by a low Strouhal number ($St = \frac{f \cdot L_r}{U_\infty} \approx 0.12$) and corresponds to the flapping instability (oscillation of the shear layer). This instability is in agreement with previous studies reported in the literature by [6] and [10]. The second instability, shown as a small accumulation of energy marked with a blue cross in the plot, has a higher Strouhal number ($St \approx 1$) and is associated with the formation and shedding of vortices, as reported in the literature by [7] and [10]. Our results are in excellent agreement with these previous studies.

II.4 Proper Orthogonal Decomposition (POD)

Proper Orthogonal Decomposition (POD) is a statistical technique widely used in fluid dynamics to extract the most energetic modes from a complex flow field. It is often employed to reduce the dimensionality of a system, making it easier to analyze and simulate. POD is particularly useful for identifying coherent structures in turbulent flows, and it

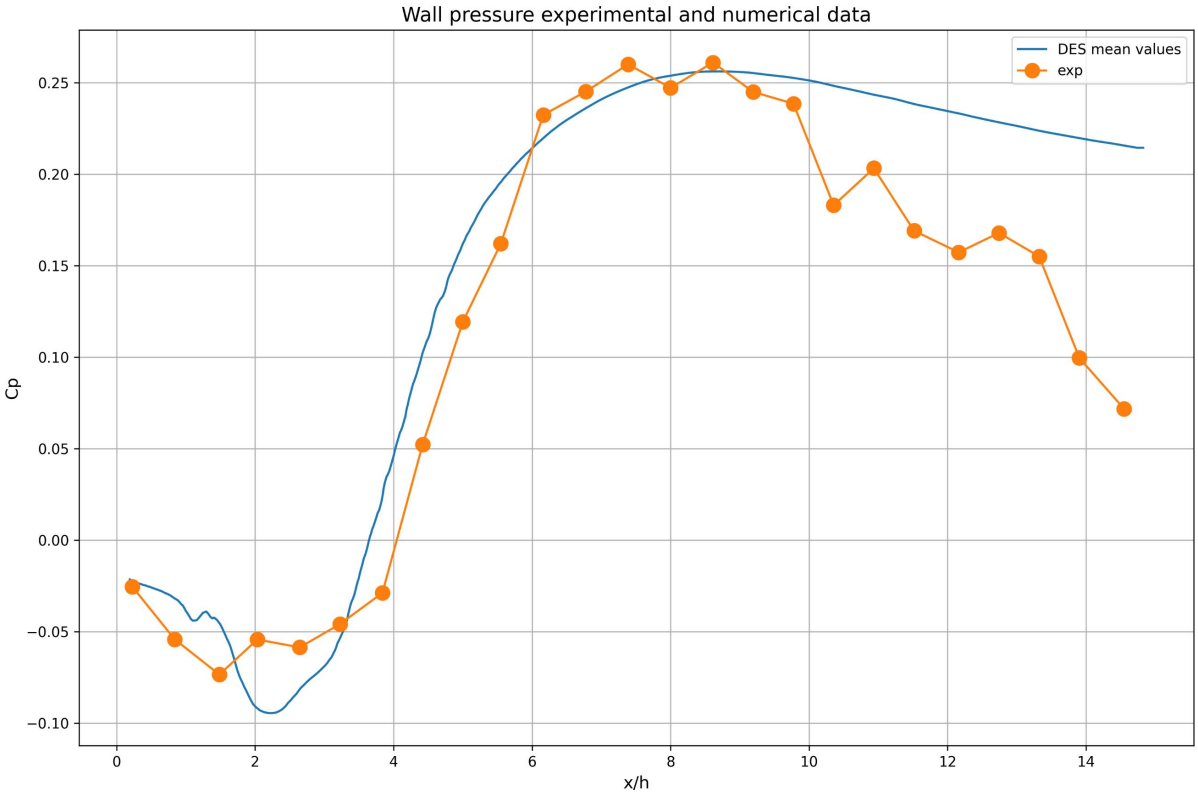

FIGURE II.13: Comparison of the wall pressure coefficient between experimental and DES model results.

provides a means of decomposing a flow field into a set of orthogonal modes ranked by their energy content.

II.4.1 Mathematical Definition of POD

Given a set of velocity fields $u(x,t)$ from a simulation or experiment, POD seeks to represent the velocity field as a linear combination of orthogonal spatial modes $\phi_i(x)$ and corresponding temporal coefficients $a_i(t)$. The decomposition is expressed as:

$$u(x,t) = \sum_{i=1}^{N} a_i(t)\phi_i(x), \tag{II.5}$$

where:

- $u(x,t)$ is the velocity field at position x and time t,
- $a_i(t)$ are the time-dependent POD coefficients,
- $\phi_i(x)$ are the spatial POD modes,
- N is the number of modes used for the decomposition.

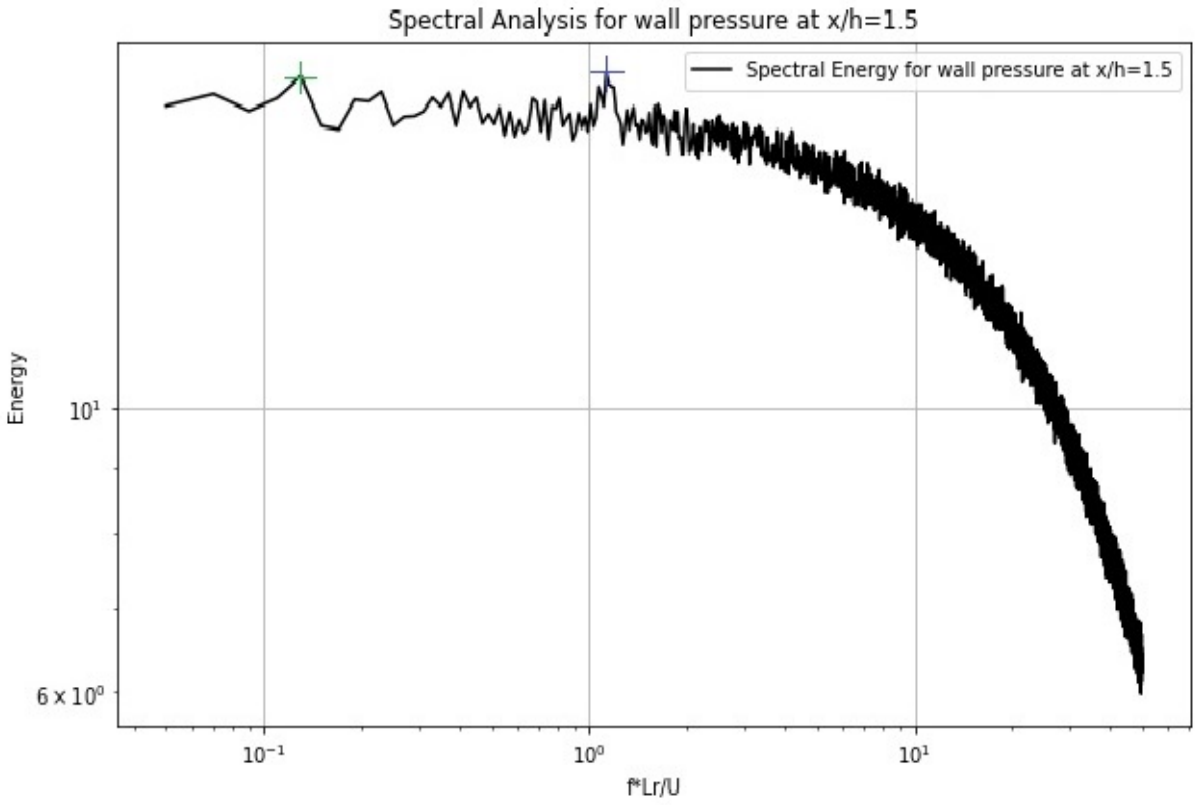

FIGURE II.14: Non-dimensional power spectra of fluctuating wall pressure measured at $x/h = 1.5$ for our current study at $Re_h = 89,100$.

The spatial modes $\phi_i(x)$ are orthogonal, meaning that:

$$\int \phi_i(x)\phi_j(x)\,dx = \delta_{ij}, \tag{II.6}$$

where δ_{ij} is the Kronecker delta, which equals 1 if $i = j$ and 0 otherwise.

II.4.2 Energy Maximization and Eigenvalue Problem

The primary goal of POD is to find a set of orthogonal modes that maximize the total kinetic energy of the flow. This problem can be formulated as an eigenvalue problem, where the velocity correlation matrix $\mathbf{R}$ is diagonalized:

$$\mathbf{R}\phi_i(x) = \lambda_i\phi_i(x), \tag{II.7}$$

where:

- $\mathbf{R}$ is the two-point correlation tensor of the velocity field,
- λ_i are the eigenvalues representing the energy content of each mode,
- $\phi_i(x)$ are the eigenfunctions or modes corresponding to the eigenvalues.

The eigenvalues λ_i are sorted in descending order, meaning that the first mode $\phi_1(x)$ captures the largest amount of energy, followed by the second mode $\phi_2(x)$, and so on.

II.4.3 POD for Reduced-Order Modeling

POD is frequently used for reduced-order modeling (ROM), where the most energetic modes are retained to approximate the flow field with a reduced set of modes. Instead of using all N modes, only the first few modes, say M (where $M < N$), are used:

$$u(x,t) \approx \sum_{i=1}^{M} a_i(t)\phi_i(x). \tag{II.8}$$

This truncated sum provides a low-dimensional approximation of the flow field, which is computationally efficient and retains the most critical flow features.

II.4.4 Snapshot Method for POD

One common approach to implementing POD in computational fluid dynamics (CFD) is the snapshot method, introduced by Sirovich (1987). In this method, the velocity field is sampled at discrete time steps, creating a set of snapshots. The POD modes are then computed from these snapshots. Given M snapshots of the velocity field $\{u(x,t_1), u(x,t_2), ..., u(x,t_M)\}$, the temporal correlation matrix $\mathbf{C}$ is constructed:

$$C_{ij} = \int u(x,t_i)u(x,t_j)\,dx, \tag{II.9}$$

and the eigenvalue problem is solved for the correlation matrix $\mathbf{C}$:

$$\mathbf{C}a_i = \lambda_i a_i. \tag{II.10}$$

The spatial modes $\phi_i(x)$ are then computed using the time-dependent coefficients a_i and the snapshots:

$$\phi_i(x) = \frac{1}{\lambda_i}\sum_{j=1}^{M} a_i(t_j)u(x,t_j). \tag{II.11}$$

II.4.5 Applications of POD

POD has numerous applications in fluid dynamics, including:

- Identifying coherent structures in turbulent flows.
- Flow field reconstruction from limited data.
- Reduced-order modeling for efficient simulation.
- Noise reduction in experimental data.

The efficiency of POD lies in its ability to capture the dominant flow features with a minimal number of modes, allowing for significant data compression and simplification of complex systems. After applying the POD method to our dataset, a key observation is that Mode 1 is the most energetically dominant. This finding is illustrated in the histogram shown in Figure II.15, where the energy contribution of each mode is displayed. Additionally, the cumulative energy plot in Figure II.16 shows that the combination of all modes accounts for the entirety of the energy in the system. The contour of Mode 1,

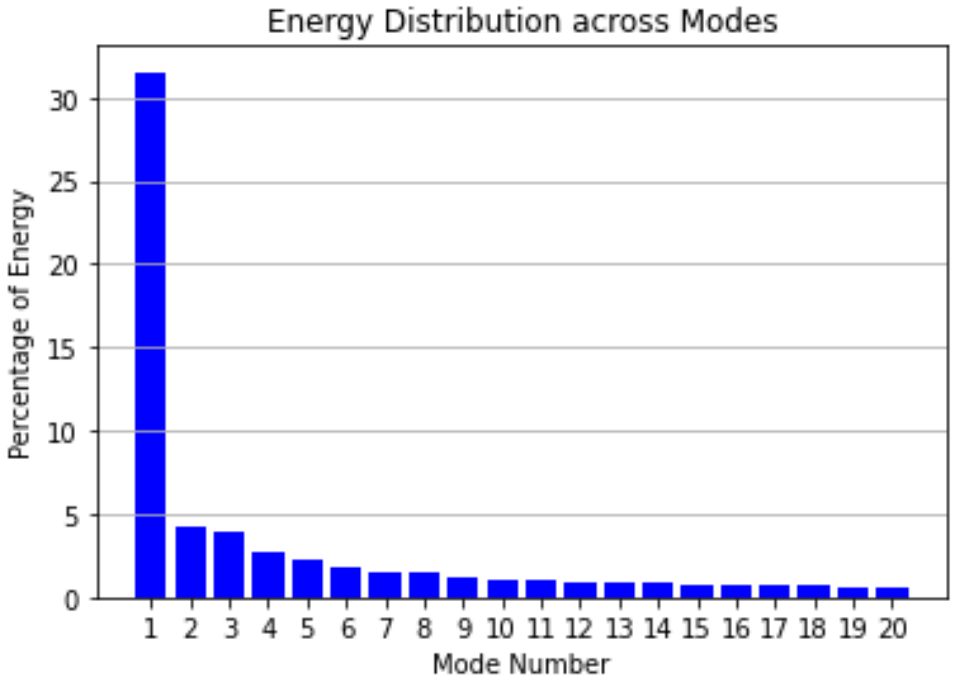

FIGURE II.15: Histogram showing the energy percentage for each mode.

displayed in Figure II.17, reveals distinct oscillations in the shear layer. A notable feature is the bulbous structure that narrows and expands, with the oscillations reaching their minimum negative value between $x/h = 1.8$ and $x/h = 3.5$. This oscillatory behavior plays a crucial role in the dynamics of the separated flow over the BFS. Targeting control strategies on this particular dynamic could potentially improve flow performance and reduce drag.

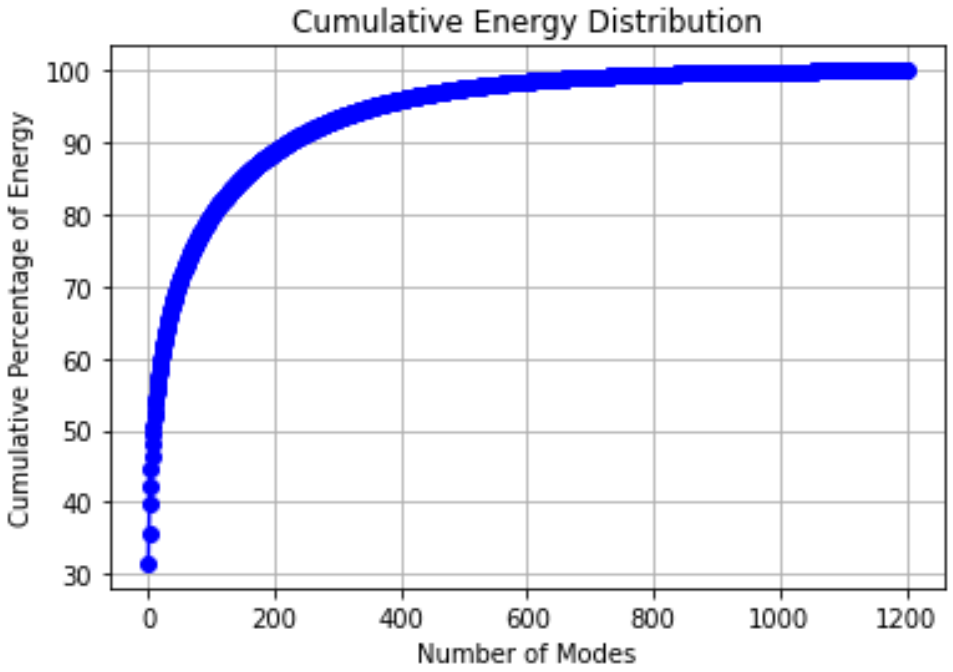

FIGURE II.16: Cumulative energy percentage across all modes.

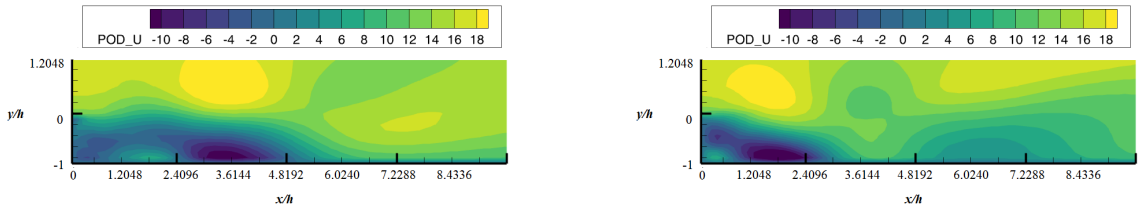

(A) reduced order x velocity at t_1 (B) reduced order x velocity at t_2

FIGURE II.17: reduced order x velocity at different instants

III Open and Closed Loop Control for Flow Optimization

Chapter abstract

This chapter explores a numerical study using ANSYS Fluent to compare different methods of controlling separated flow over (BFS), specifically active flow control with continuous and pulsed jets, against a new approach. The new method involves a closed-loop control system that uses wall pressure measurements to activate flow control only when the separation bubble is at its largest. This timing-based control helps manage airflow more intelligently and reduces energy use. The study shows that this new method not only controls the flow effectively but also saves energy compared to traditional continuous and pulsed jet techniques. These findings suggest that this new approach could be more efficient in various aerodynamic applications.

III.1 Introduction

The control of flow over a (BFS) has been a significant area of research due to its complex flow dynamics and practical importance in various engineering applications. Flow separation and reattachment commonly occurring in BFS configurations present challenges such as increased drag and unsteady flow behavior, which can adversely affect system performance and stability. To address these challenges, a wide range of active flow control techniques have been developed, each offering unique advantages and insights into managing flow separation and enhancing flow stability. This chapter synthesizes recent advancements in the active control of BFS flow, drawing from various studies that have explored different methodologies and techniques. These studies collectively contribute to the understanding of BFS flow control, providing a comprehensive view of the field's progress and identifying areas where further research is needed. The synthesis of the literature focuses on the development and application of active control methods aimed at reducing flow separation and improving flow stability over (BFS). Key contributions include the reduction of complex models to low-order feedback controllers, the application of advanced control strategies such as closed-loop control and magnetic actuation,

and the implementation of experimental techniques for validating control effectiveness. In particular, the study by [9] highlights the importance of model reduction in designing efficient feedback controllers for aerospace applications, while [19] and [12] demonstrate the effectiveness of active and closed-loop control strategies in managing flow dynamics. Through a detailed comparison of these studies, we aim to provide a comprehensive review of the advancements in active flow control over a BFS, identifying the strengths and limitations of each approach. We also explore emerging techniques such as pulsed jets actuation and visual feedback control, offering insights into potential future directions for research and application in this field.

III.2 Simulation

Among the types of control devices used by [7], the Murata Blowing Control Device is a specific example of a pulsed air jet actuator as shown in fig. III.1. This device is designed to manipulate airflow over surfaces by generating high-frequency pulsed air jets. Such devices are used to control phenomena like boundary layer separation, which can enhance aerodynamic performance by reducing drag or increasing lift. To replicate the

FIGURE III.1: Murata micro blower.

experimental work in the numerical simulation. We have correctly added a channel with the same dimensions as the Murata device shown in fig III.2 in the numerical domain shown in fig III.3 and positioned it $0.2h$ before the corner of the BFS, as shown in Fig. III.4 and Fig. III.5. This placement is crucial as it aligns with the experimental setup, ensuring that the flow characteristics influenced by the pulsed jet actuator are accurately modeled in the simulation. The positive pulsed signal control with different frequencies alternates between 0 and $V_{\text{jets,max}}$, with a period of $T = \frac{1}{f}$. The signal remains at $V_{\text{jets,max}}$ for the positive half-cycle of the sine wave and at 0 for the negative half-cycle. as shown in Fig. III.6, was introduced in ANSYS Fluent as a User-Defined Function (UDF) according to the equation:

The velocity profile of the pulsed signal is defined as:

$$V_{\text{jets}}(t) = \begin{cases} V_{\text{jets,max}}, & \text{if } \sin(2\pi ft) \geq 0, \\ 0, & \text{if } \sin(2\pi ft) < 0, \end{cases}$$

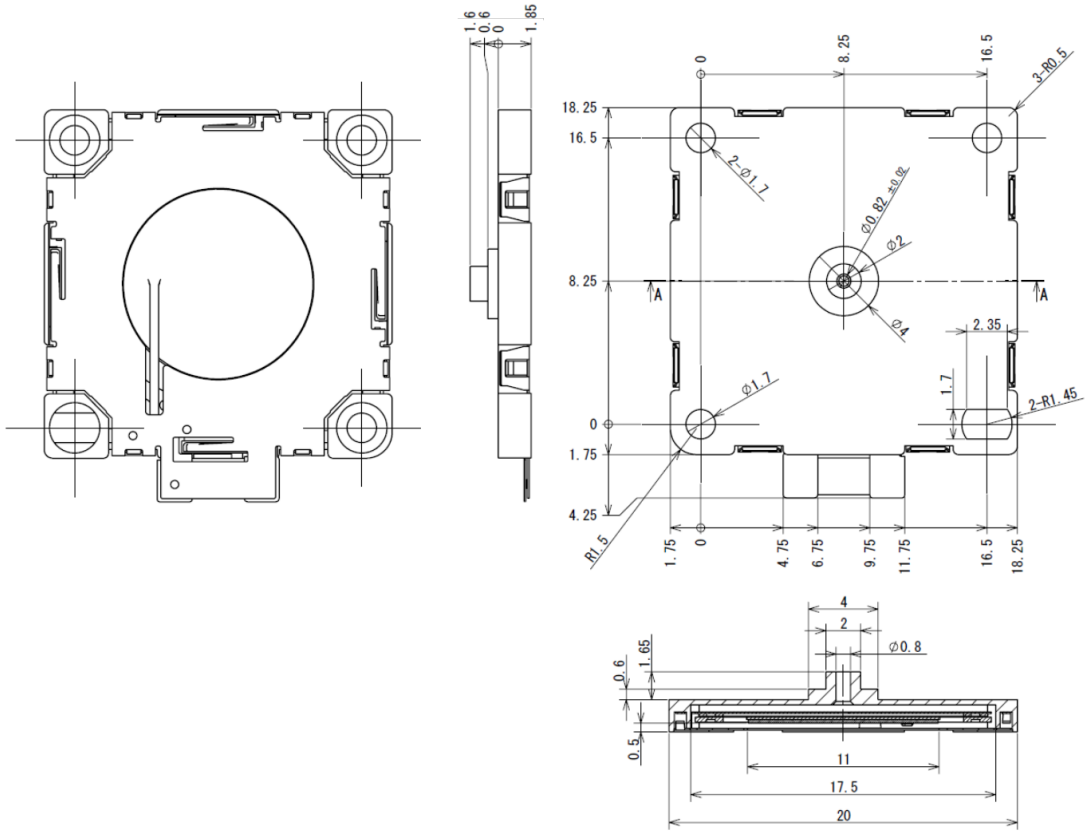

FIGURE III.2: Real Murata micro blower dimensions.

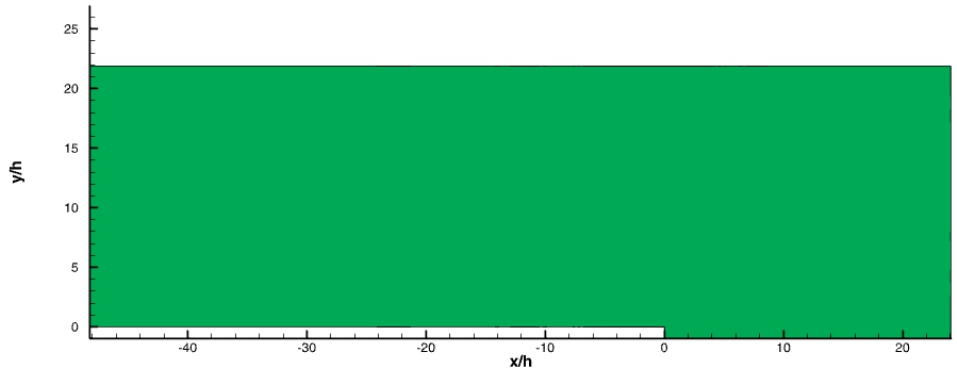

FIGURE III.3: Numerical domain.

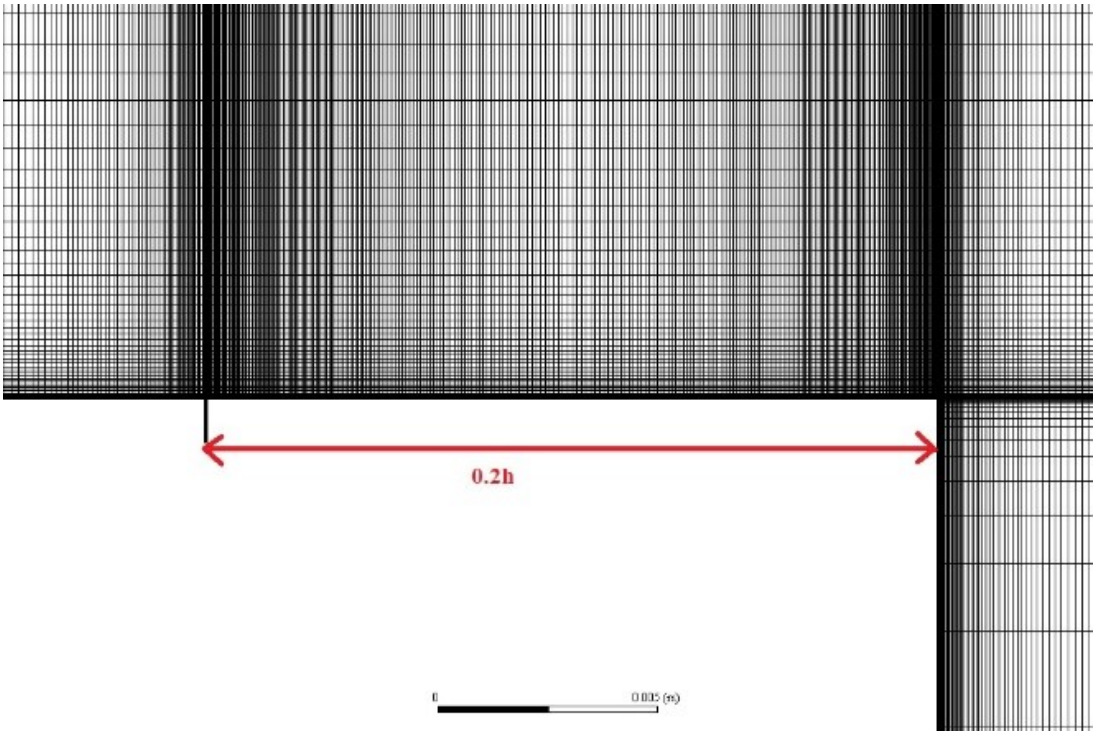

FIGURE III.4: Position to place the actuator same as experimental configuration.

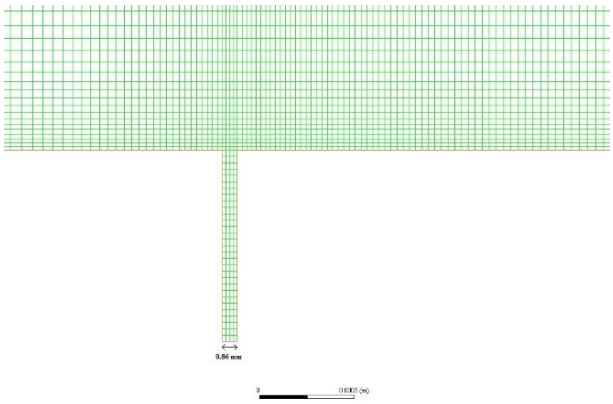

FIGURE III.5: Actuator simulated by inlet channel.

where:

- $V_{\text{jets}}(t)$: The velocity of the jets at time t (in m/s),
- $V_{\text{jets,max}}$: The maximum velocity of the jets (in m/s),
- f: The frequency of the pulsed signal (in Hz),
- t: Time (in seconds).

III.3 Results and Discussion

Figure III.8 presents a low-order vorticity field obtained through Proper Orthogonal Decomposition (POD) by retaining the most significant dynamic modes. This results in a prominent bulbous structure that expands and contracts, effectively illustrating the movement of the shear layer. Figure III.9 presents a contour plot illustrating the relationship and correlation between the wall pressure at $x/h = 1.5$ and both the x-velocity and y-velocity components. The plot shows a strong linear correlation between the wall pressure and these velocity components, indicating a significant direct relationship between them. Figure III.10 shows the unsteady wall pressure values at $x/h = 1.5$ and the shear layer flapping illustrated with two positions, 0 and 1. The analysis confirms that a wall pressure threshold of -57.78 is an effective threshold for predicting the position of the shear layer based on wall pressure measurements. Figure III.11 illustrates the mean values of wall shear stress downstream of a backward-facing step (BFS) under different frequencies of pulsed signal control. The plot reveals noticeable differences in the wall shear stress for various pulse frequencies, indicating that the frequency of the control signal significantly influences the flow behavior.

In Figure III.13, which shows the mean values of wall shear stress downstream of the BFS for different flow control methods, it is evident that the flow without control results in the largest reattachment length. Continuous active flow control demonstrates significant effectiveness in reducing the recirculation zone, achieving great results in minimizing the reattachment length. However, both pulsed and closed-loop control methods exhibit almost the same efficiency in controlling the flow while optimizing energy usage. Specifically, the pulsed control method saves approximately 50% of energy compared to continuous control, while the closed-loop method saves around 61% of energy as shown in fig III.12 , delivering the same performance in reducing the recirculation zone as the continuous method but with much higher energy efficiency.

III.4 Conclusion

This chapter investigates the control of separated flow over a backward-facing step (BFS) through numerical simulations using ANSYS Fluent, incorporating both continuous and pulsed active flow control methods, along with an innovative closed-loop approach. A key aspect of this work involved simulating a channel with the same dimensions as the Murata blower device used in Chovet's experimental setup. This allowed for accurate replication

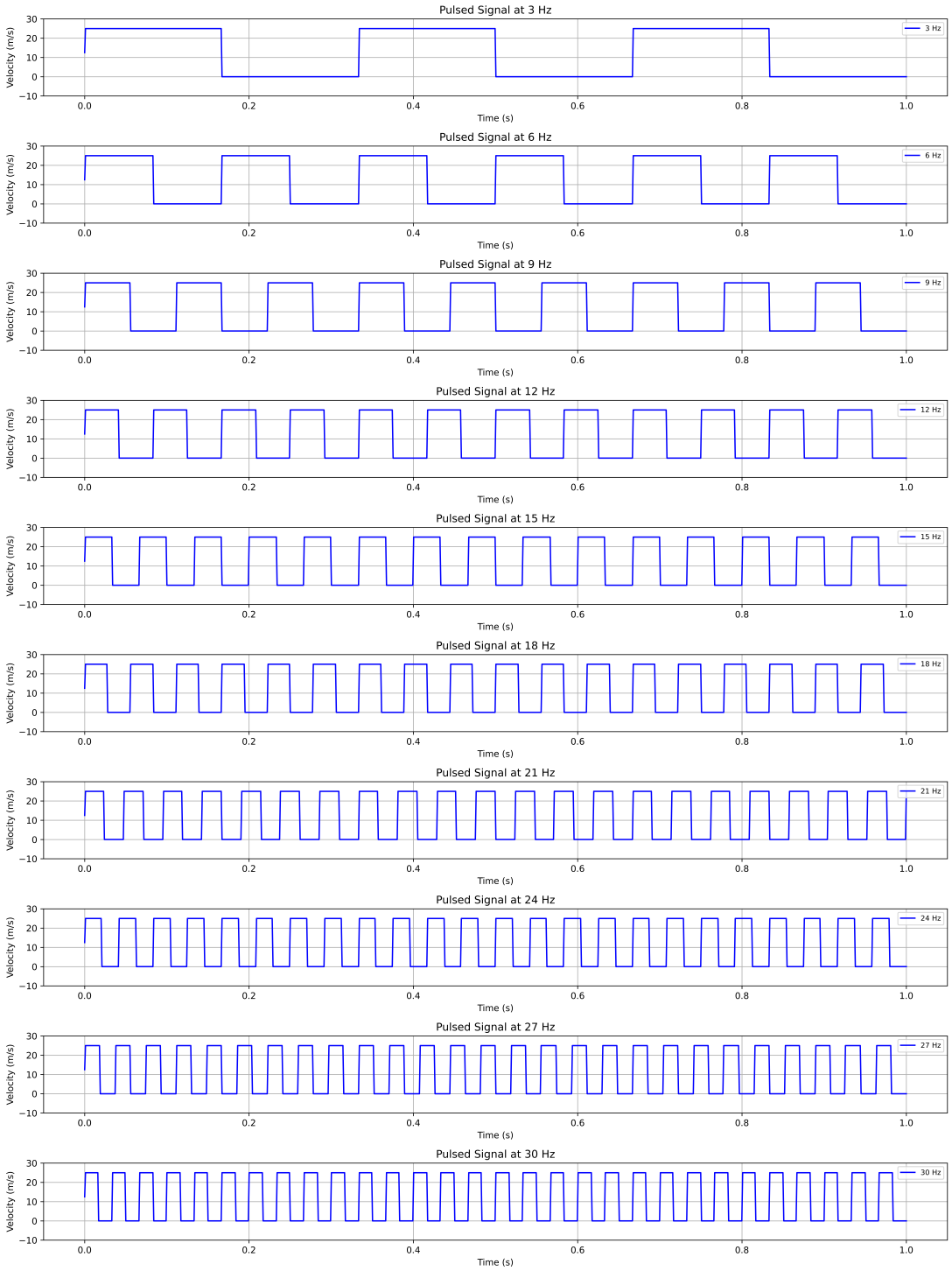

FIGURE III.6: Pulsed signals at different frequencies.

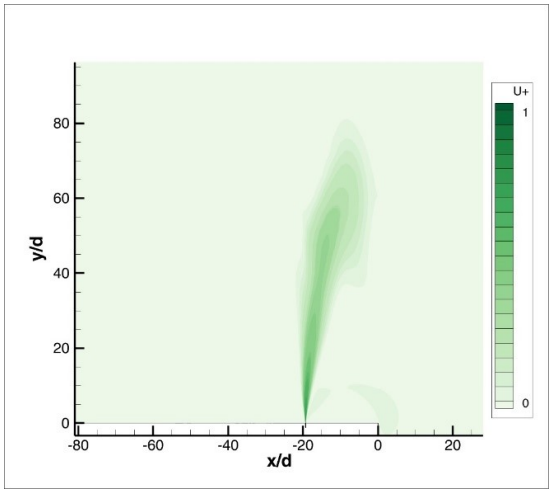

(A) Mean Flow of Pulsed Jets with $V_{\text{jets}} = 25m/s$

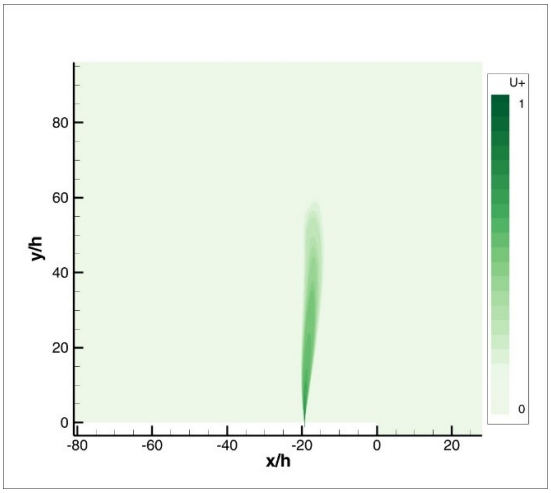

(B) Mean Flow of Pulsed Jets with $V_{\text{jets}} = 18m/s$

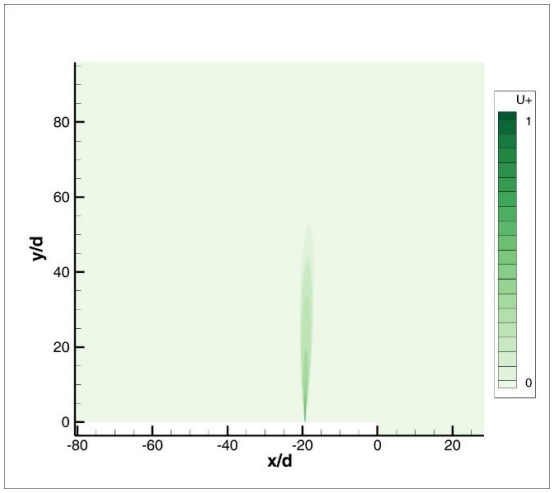

(C) Mean Flow of Pulsed Jets with $V_{\text{jets}} = 10m/s$

FIGURE III.7: Steady jet mean velocity fields U+ normalized by the maximum jet velocity, (a) Ve=10m/s, (b) Ve=18m/s , (c) Ve=25m/s.

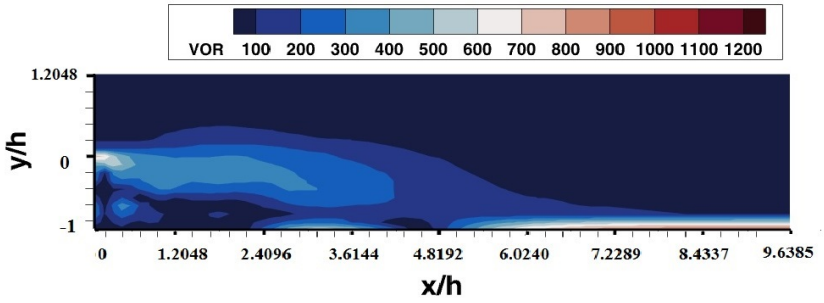

FIGURE III.8: Low-order vorticity contour of separated flow over BFS.

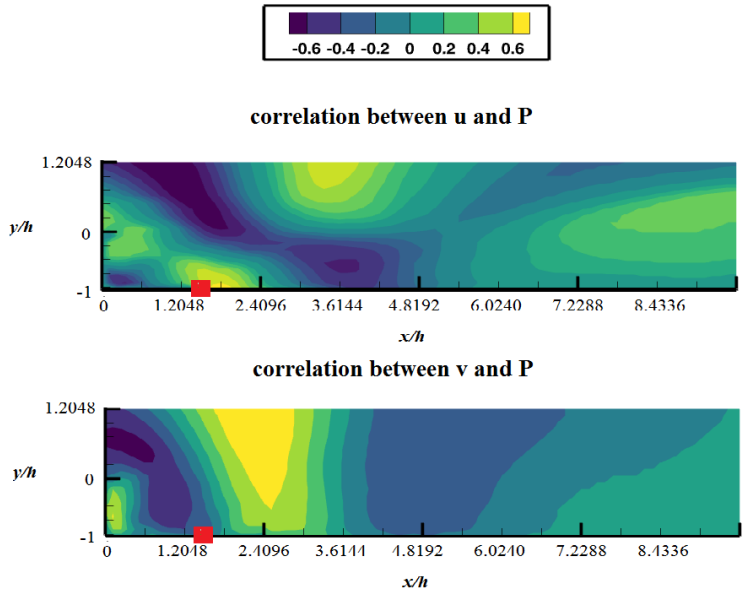

FIGURE III.9: Correlation contour between wall pressure at $x/h = 1.5$ and velocity field.

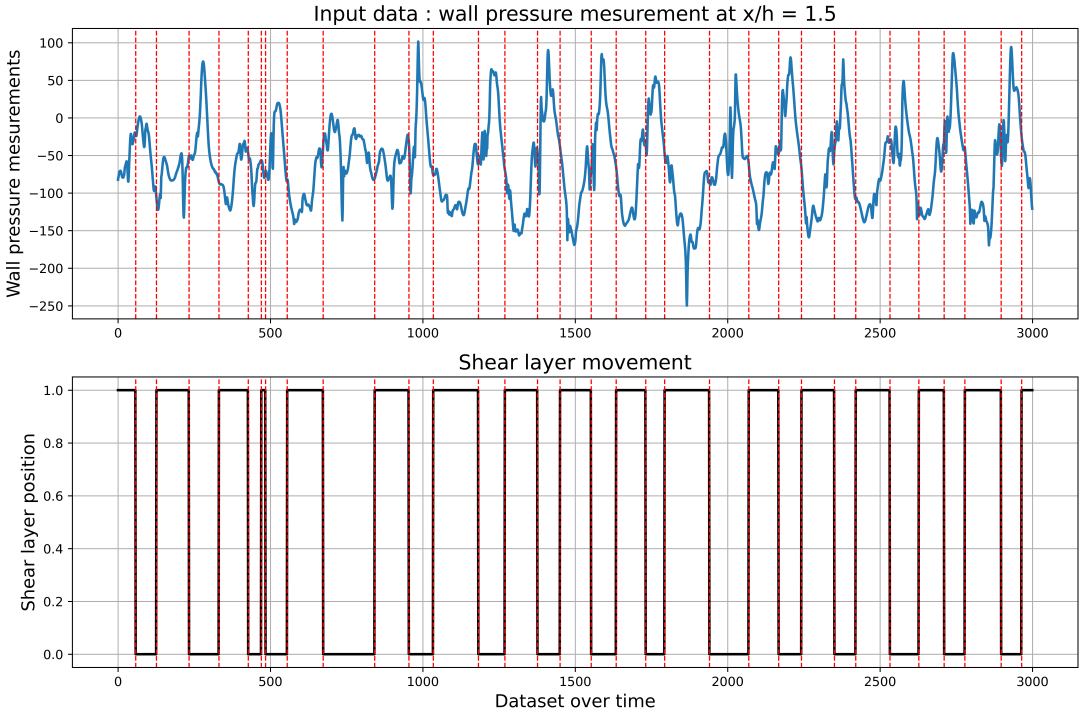

FIGURE III.10: Unsteady wall pressure values at $x/h = 1.5$ and the shear layer flapping illustrated with two positions, 0 and 1.

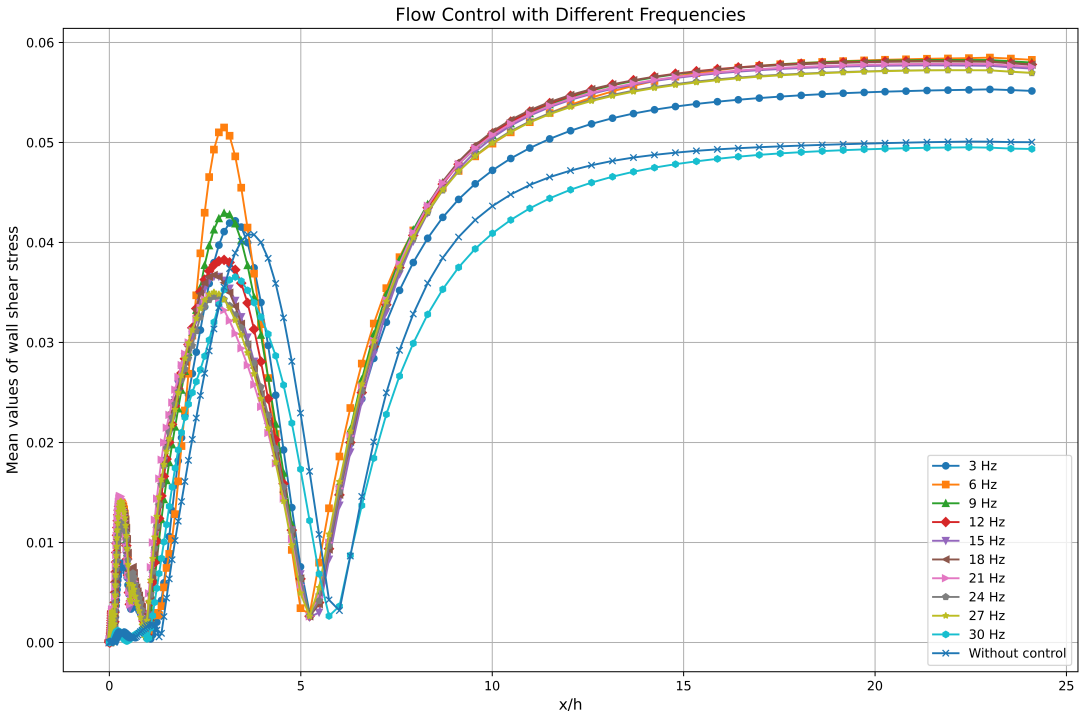

FIGURE III.11: Mean values of wall shear stress downstream of the BFS for different frequencies of pulsed signals.

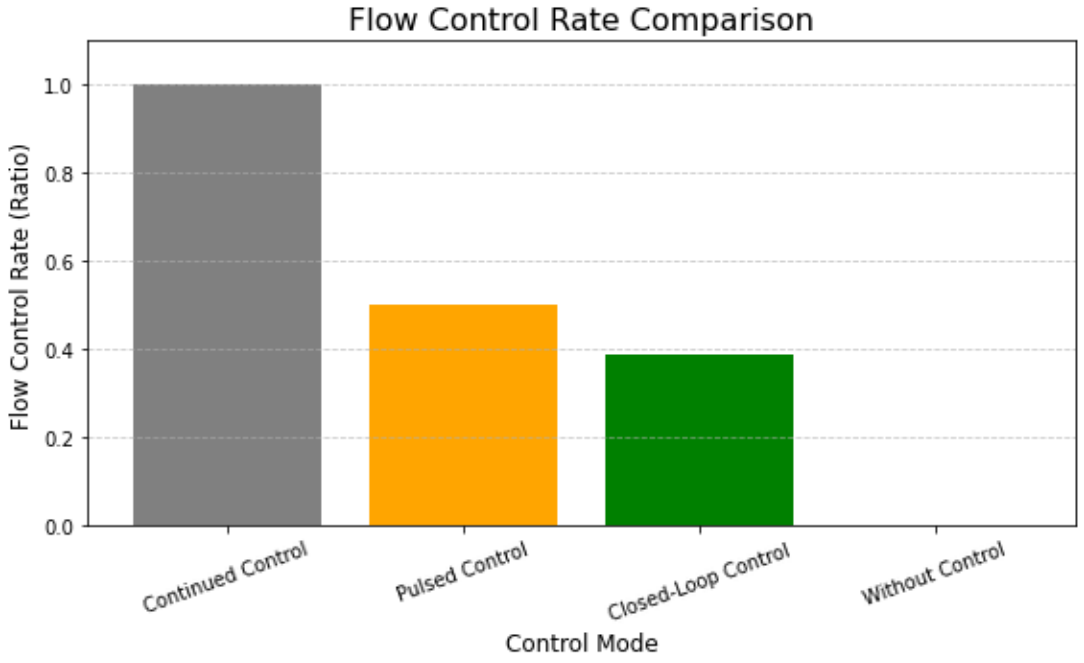

FIGURE III.12: Flow control rate comparison across different flow control approaches.

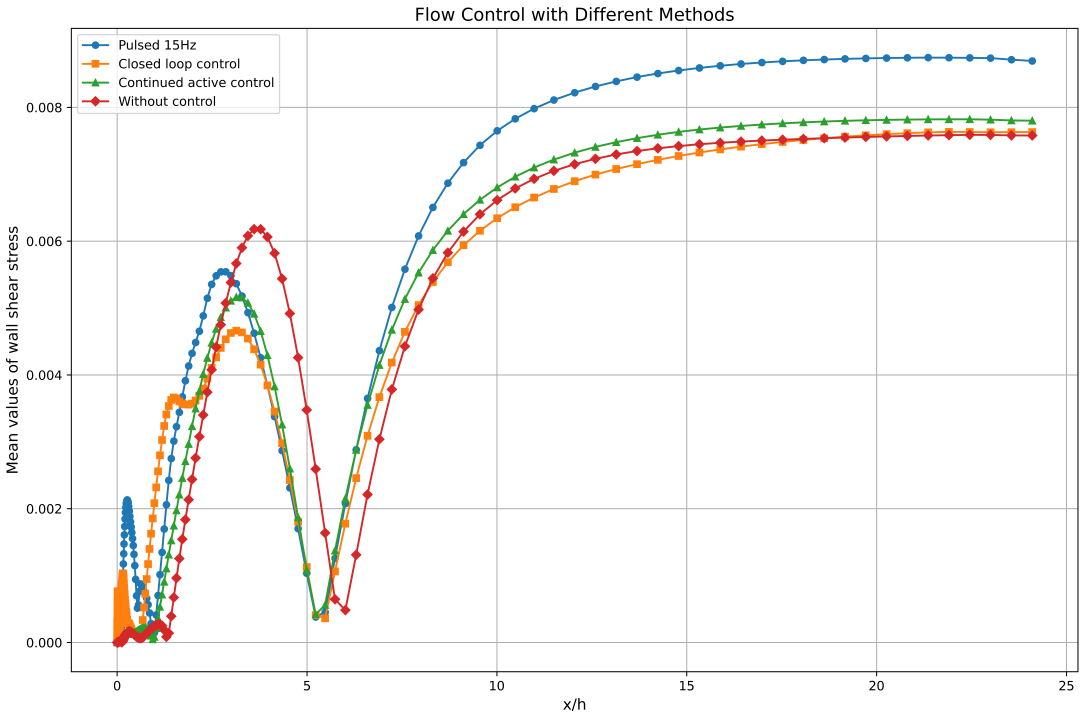

FIGURE III.13: Mean values of wall shear stress downstream of the BFS for different methods of control.

of the experimental conditions, ensuring the results closely mirrored real-world scenarios. By employing wall pressure measurements to activate the closed-loop control system only during periods of maximum flow separation, the study demonstrated substantial energy savings compared to traditional continuous and pulsed jet control methods. The closed-loop approach achieved a 60% reduction in energy consumption while maintaining the same efficiency in controlling flow separation as continuous methods. The pulsed control method, which saves 40% of energy, further underscored the importance of aligning control frequencies with natural shear layer dynamics to optimize flow control. The simulation using the Murata blower dimensions provided validation of the numerical model's accuracy, supporting the applicability of these findings to practical aerodynamic scenarios. This work contributes valuable insights into intelligent flow management and highlights the potential for energy-efficient adaptive control systems in complex flow environments.

IV Predicting Separated Flow Patterns with Machine Learning Techniques

Chapter abstract

This chapter aims to improve flow control strategies by predicting separated flow dynamics only through wall pressure measurements using artificial intelligence and numerical data. Initially, we identify numerical models that accurately replicate separated flow dynamics. Notably, the Detached Eddy Simulation (DES) model strongly agrees with experimental data, particularly in the turbulent regime at Reh= 89100, downstream of backward-facing steps.
After completing a correlative analysis, it reveals a significant correlation between various wall pressure points and the velocity field, prompting the adoption of deep learning techniques such as Recurrent Neural Networks with Long Short-Term Memory (LSTM). These neural networks, tailored for time-dependent data, demonstrate high accuracy with a low Mean Squared Error (MSE) of 13.48% using ten wall pressure points in predicting detailed flow dynamics over the backward-facing step.
To enhance predictions, Proper Orthogonal Decomposition (POD) is utilized to reduce system complexity while retaining essential dynamics, resulting in a lower MSE of 5.07%. Additionally, we identify the ideal wall pressure measurement region that accurately captures the entire dynamic behavior, achieving an acceptable MSE of 23.48% with only three wall pressure points. This research aids in developing efficient flow control strategies with limited pressure data and offers valuable insights for closed-loop flow control applications.

IV.1 Study Area and Mesh Generation

In this part, we have selected a rectangular area (fig IV.1) that includes the important zone containing the recirculation zone and the shear layer, which is crucial for our research because they greatly affect how the flow behaves and the overall characteristics of the BFS. By focusing on these specific areas, we hope to better understand the complex dynamics and fundamental mechanisms of the phenomenon of separation flow.

We have chosen a specific zone within the BFS. This zone spans from $(x/h = 0)$ to $(x/h = 9.6385)$ along the x-axis and from $(y/h = -1)$ to $(y/h = 1.2048)$ along the y-axis. To analyze this zone effectively, we have created a mesh with 1600 elements, forming a matrix of dimensions $(80, 20)$, to discretize and represent the flow fields accurately within the selected zone, enabling us to conduct detailed investigations and gather valuable data for our research.

We have selected multiple points (fig IV.2) along the wall to measure the wall pressure. By strategically choosing these locations, we can accurately capture and analyze the variations in wall pressure along the surface (vertical and horizontal wall around the recirculation zone) to show the interaction and relationship between wall pressure and the separated flow on BFS dynamics.

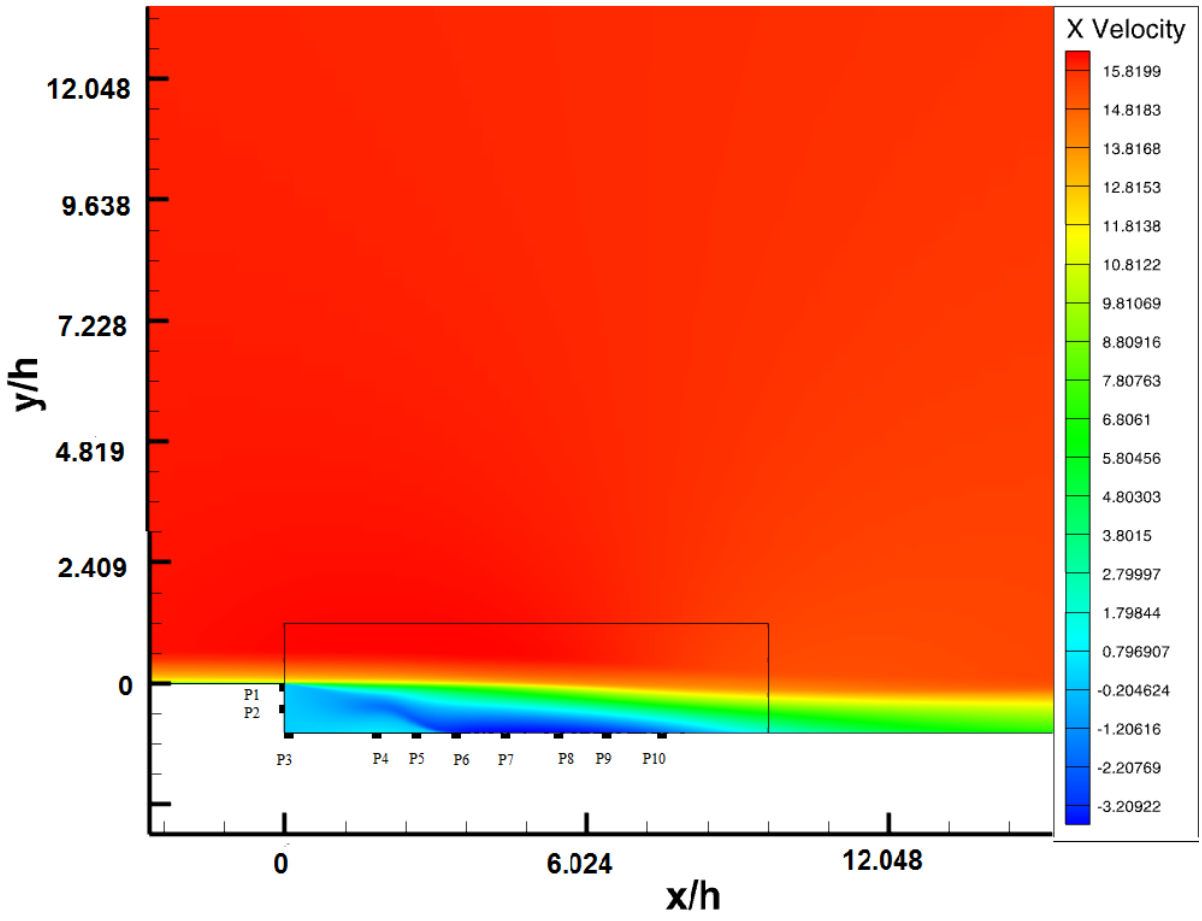

FIGURE IV.1: Chosen rectangular zone with mesh for study.

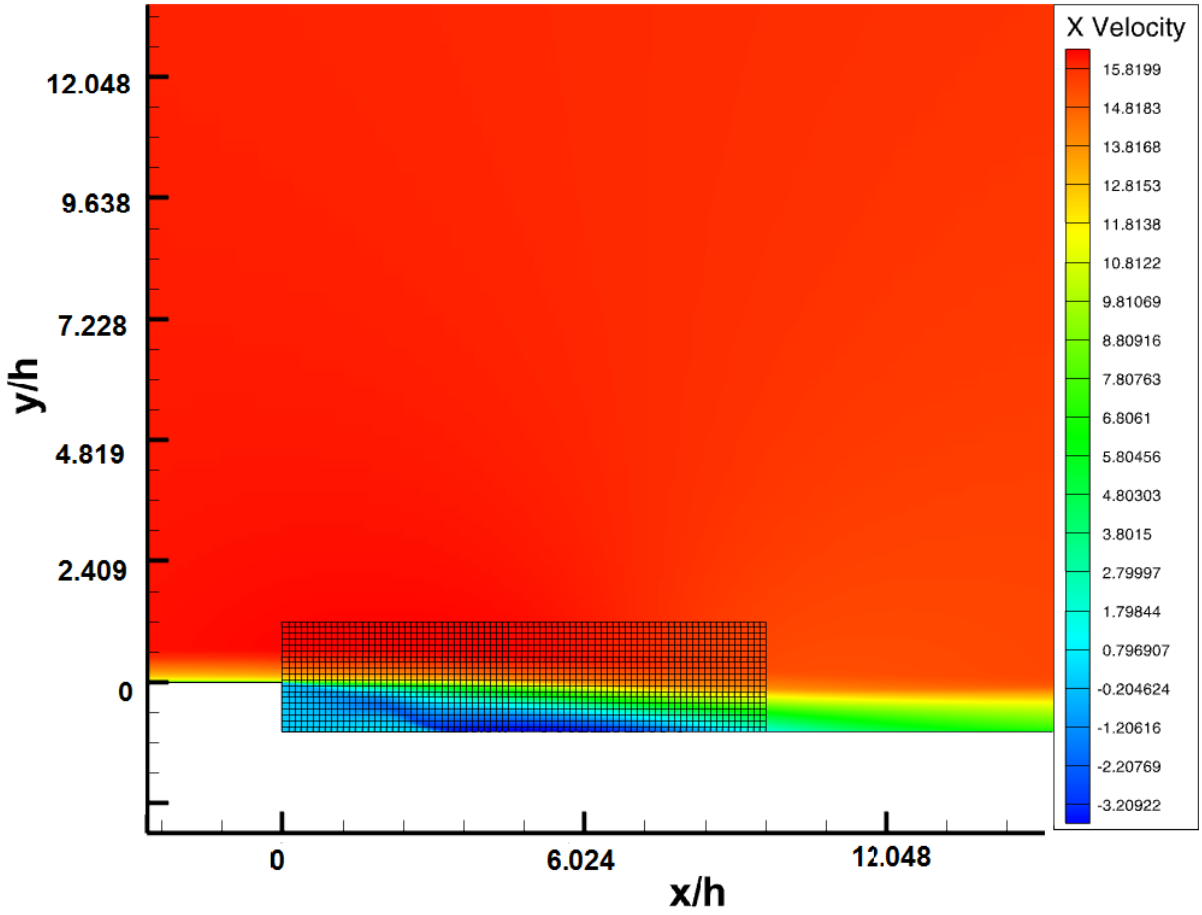

FIGURE IV.2: Chosen ten points wall pressure for study.

IV.2 Correlative Study between Wall Pressure and Velocity Field

Before diving into machine learning analysis between wall pressure and velocity field, it is essential to conduct a correlation study and examine the relationship between the variables involved to determine if there is a linear association between them. This preliminary investigation allows us to understand the degree of dependency between the variables by assessing the strength and direction of the relationship. This correlation analysis is a crucial step before moving to machine learning, as it assesses the feasibility of the learning process by identifying significant features and relationships within the variables. We conducted individual correlation studies between each point of wall pressure and the corresponding velocity fields (X-velocity and Y-velocity). This analysis was performed for all points of wall pressure along the surface, by examining the correlation between a

specific pressure point and the velocity field. We repeated this process for each point of wall pressure, allowing us to understand how changes in pressure relate to variations in the X-velocity and Y-velocity throughout the entire dataset. Using Python programming and its libraries to perform a correlation analysis between wall pressure and velocity. Initially, we imported necessary libraries such as numpy and pandas to handle data processing. We loaded the wall pressure data as a vector from a file and loaded the velocity data and coordinates from multiple files. Using the pandas library, for each coordinate point, we calculated the correlation between the pressure vector and the velocity components. The correlation coefficient, ranging from 0 to 1, indicates the strength of the relationship. These results were then written to an output file, which enabled us to create a contour plot visualizing the correlation strength at each point. This visualization illustrates how velocity at various points relates to wall pressure, providing valuable insights into the flow dynamics and ensuring that the machine learning model is trained on the most relevant and influential data. In fig IV.3, which represents the correlation with the X-velocity, along the horizontal walls, a positive correlation is observed near all pressure points, while a negative correlation is observed above these points. Regarding the vertical walls, specific locations exhibit distinct correlation characteristics. At Point 1, located at the summit of the BFS, a positive correlation is prominent. However, at Point 2, the correlation with the velocity field is weak. At Point 3, positioned at the corner, there is a moderate positive and negative correlation, apparent across all velocity fields. Furthermore, fig IV.4 shows correlations with Y-velocity on the horizontal wall. Points are in positive correlation with the zone above and negative correlation in the zone before, and zones of strong correlation are near the wall in correlation with the points after the recirculation zone. Correlation with vertical wall pressure is weaker than with the horizontal wall. Additionally, we can observe that points under the shear layer (point 4, point 5, point 6, and point 7) have the strongest correlation with both X and Y velocity.

IV.3 Methodology of Machine Learning Using neural network Algorithm

The recent years have witnessed remarkable progress in machine learning, particularly deep learning, where foundational work by Ivakhnenko and Lapa (1965), Ivakhnenko (1971), Bengio (2009), and more recently by Carrio, Sampedro, Rodriguez-Ramos, and Campoy (2017), as well as Khan and Yairi (2018), have paved the way for broad applications in information extraction across varied datasets. Among the emerging architectures, the Recurrent Neural Network (RNN) is notable, as highlighted by Robinson and Fallside (1987), Werbos (1988), Williams (1989), and Ranzato et al. (2014).

IV.3.1 Challenges in Sequential Data Processing

The temporal limitations of Convolutional Neural Networks (CNN) and Deep Neural Networks (DNN) when processing sequential data, such as text, audio, and video, are well-documented by Fukushima (1980), LeCun et al. (1989), Weng et al. (1993), Rawat and Wang (2017), Guo et al. (2017), and Sharma and Singh (2017). Addressing these

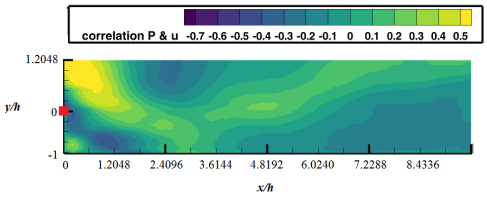

(A) correlation between u and $P1$

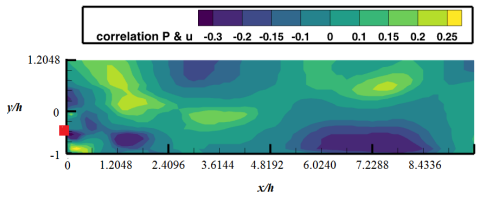

(B) correlation between u and $P2$

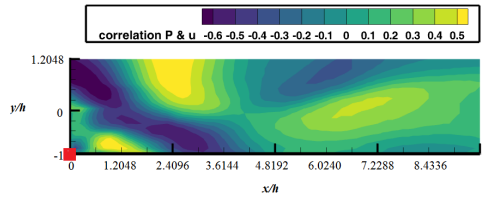

(C) correlation between u and $P3$

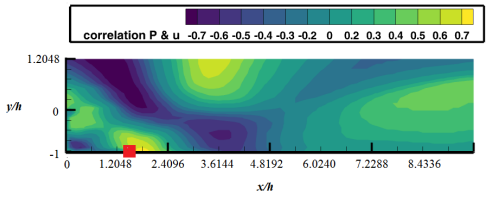

(D) correlation between u and $P4$

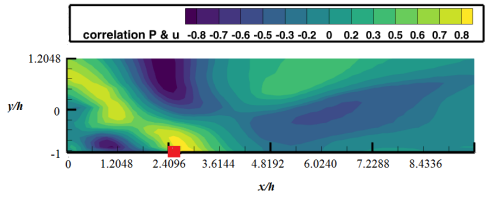

(E) correlation between u and $P5$

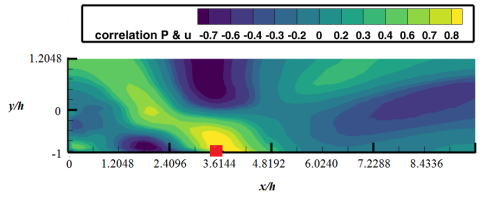

(F) correlation between u and $P6$

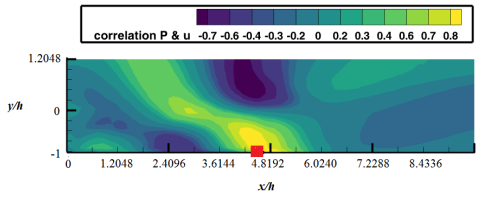

(G) correlation between u and $P7$

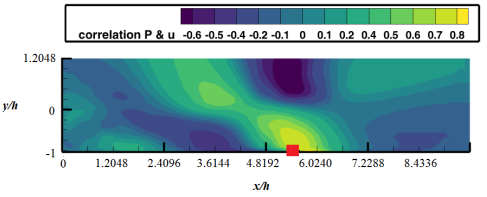

(H) correlation between u and $P8$

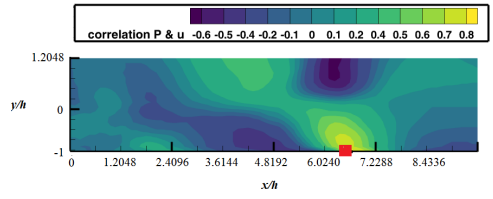

(I) correlation between u and $P9$

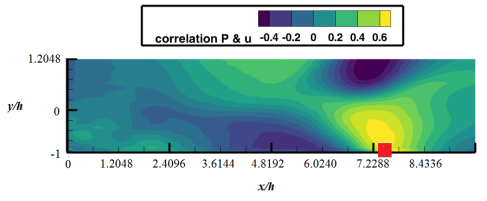

(J) correlation between u and $P10$

FIGURE IV.3: Correlation between u and wall pressure points.

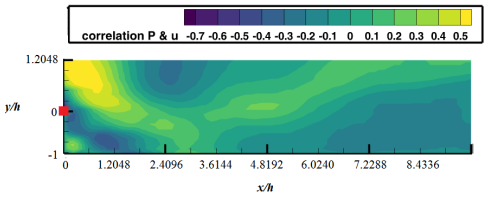

(A) correlation between v and $P1$

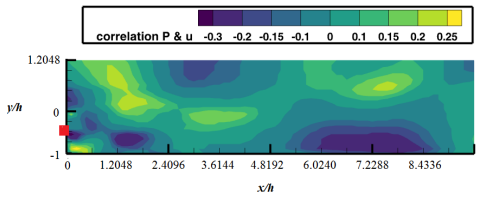

(B) correlation between v and $P2$

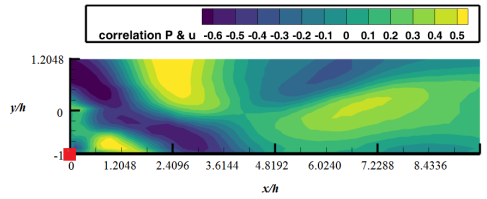

(C) correlation between v and $P3$

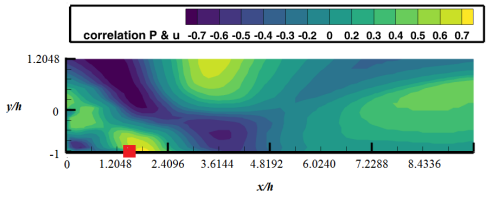

(D) correlation between v and $P4$

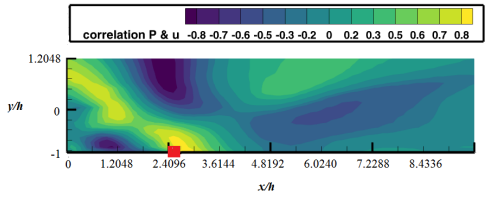

(E) correlation between v and $P5$

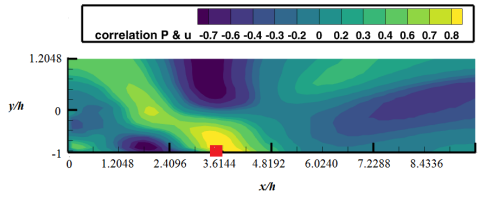

(F) correlation between v and $P6$

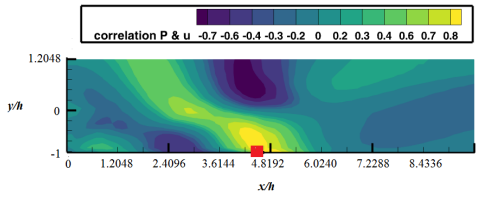

(G) correlation between v and $P7$

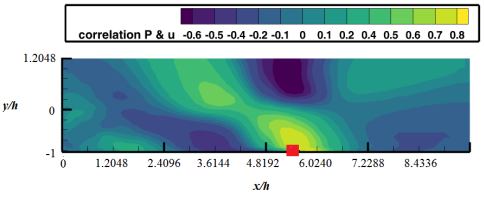

(H) correlation between v and $P8$

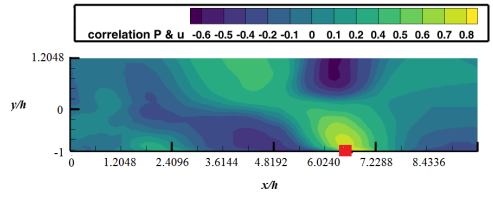

(I) correlation between v and $P9$

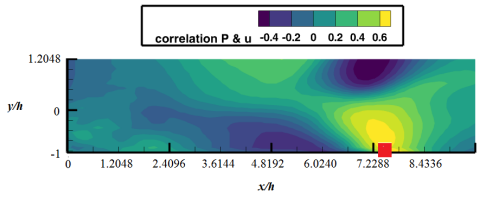

(J) correlation between v and $P10$

FIGURE IV.4: Correlation between v and wall pressure points.

challenges, discrete-time RNNs are often emphasized due to their capacity for temporal data processing. The cyclic connections within RNN architecture, which facilitate the integration of historical and current data, were described by Pearlmutter (1989), Brown et al. (2004), and Gallagher et al. (2005).

Standard RNNs, such as the fully connected models presented by Elman (1990), Jordan (1986), and Chen and Soo (1996), have achieved success in specific applications but struggle with long-term dependencies. This limitation was addressed in the seminal work of Hochreiter and Schmidhuber (1997) with the introduction of Long Short-Term Memory (LSTM) networks.

IV.3.2 LSTM Networks for Temporal Data

LSTM networks, a specialized RNN architecture, are designed to manage long-term dependencies and mitigate the vanishing gradient problem. They utilize a unique memory cell, regulated by input, forget, and output gates, allowing the model to retain essential information while discarding irrelevant data. LSTMs have proven effective across various tasks, including natural language processing, speech recognition, sentiment analysis, and time series forecasting, making them ideal for contexts where sequence comprehension is essential, such as unsteady flow datasets (Fernández et al., 2007; He & Droppo, 2016; Hsu et al., 2016; Sak et al., 2014; Qu et al., 2017; Altché & Fortelle, 2017; Palangi et al., 2015; Mallinar & Rosset, 2018).

IV.3.3 Enhanced LSTM Models

Further advancements in LSTM models include integrating optimization algorithms to enhance performance. Kumar and Selvaraj (2023) demonstrated improved accuracy by combining LSTM with the Black Widow Optimization Algorithm (BOA) and the Mayfly Optimization Algorithm (MOA), showing significant enhancements in model efficiency.

IV.3.4 Machine Learning in Fluid Dynamics

The application of artificial intelligence in fluid dynamics has been explored extensively. For instance, Fadla et al. (2016) utilized electrochemical sensors for real-time stochastic reconstruction of separated flows, accurately capturing low-frequency flapping modes in transitional flow regimes at an inflow Reynolds number of 1735. This model integrates electrochemical sensors with Particle Image Velocimetry (PIV) and uses Proper Orthogonal Decomposition (POD) and Linear Stochastic Estimation (LSE) to create a low-order model that effectively reduces flow separation.

Similarly, Talele et al. (2021) applied Computational Fluid Dynamics (CFD) alongside Artificial Neural Networks (ANN) to predict flow patterns around bluff bodies at high Reynolds numbers, demonstrating ANN's capacity to predict vortex generation and flow separation behavior.

IV.3.5 Artificial Neural Networks in Flow Prediction

Studies like Rajabi and Kavianpour (2012) have utilized ANN models with Direct Numerical Simulation (DNS) data to predict turbulent flow over a backward-facing step (BFS), revealing high accuracy in capturing complex flow dynamics across various Reynolds numbers. Singh et al. (2017) further employed ANN to predict turbulent separated flows over airfoils, improving lift, surface pressure, and flow separation predictions.

While ANNs are powerful for static and temporal data, they face limitations in sequential contexts compared to architectures like RNNs and LSTMs. Focused Time-Delay Neural Networks (FTDNN), demonstrated by Giannopoulos and Aider (2020), show that shallow architectures with time-delay inputs can capture temporal dependencies effectively, though selection of time-delay parameters can be challenging.

IV.3.6 Proposed Approach

This study proposes leveraging LSTM networks, particularly suited for sequential data due to their memory capabilities, to predict velocity fields from measured wall pressure in flow dynamics. To reduce system complexity while preserving dynamic information, we apply Proper Orthogonal Decomposition (POD), simplifying the dataset for efficient machine learning application. The integration of LSTM with POD offers a streamlined model capable of handling temporal dependencies in large datasets.

IV.3.7 Conclusion

LSTM networks, with their inherent ability to capture long-term dependencies, present a promising approach for predictive flow dynamics. By combining LSTM with POD, our research aims to improve predictive accuracy and computational efficiency, thereby advancing the application of neural networks in fluid dynamics modeling.

IV.3.8 LSTM Key Concepts

- **Memory Cell:** The core element of an LSTM is the memory cell, which maintains information over time. It acts as a conveyor belt, passing along relevant information and selectively forgetting unnecessary information.
- **Gates:** LSTMs utilize three types of gates to control the flow of information within the memory cell.
- **Cell State:** The memory cell maintains the cell state, which carries information over time. The input gate and forget gate determine which information is added and forgotten, respectively, in the cell state.
- **Hidden State:** The hidden state is the output of the LSTM at a given time step. It is derived from the cell state and passes through the output gate to produce the final output.

During training, the LSTM adjusts its internal parameters using backpropagation through time (BPTT) to minimize the error between predicted and actual outputs. This process enables the network to learn and capture complex temporal patterns within sequential data. By leveraging the memory cell and gating mechanisms, LSTMs can effectively handle long-term dependencies, mitigating the vanishing gradient problem. These key concepts encapsulate the fundamental aspects of LSTMs and their mechanisms for processing sequential data.

IV.3.9 Structure of the LSTM Model

The LSTM model used in our study is structured as follows:

- **Input Layer:** Receives wall pressure data points as input extracted as time-dependent data.
- **LSTM Layer:** Captures temporal dependencies in the data.
- **Dense Layers:** Fully connected layers that transform the LSTM outputs into the desired format.
- **Output Layer:** Produces the predicted velocity field corresponding to the input wall pressure measurements.

IV.3.10 Machine Learning Process

1. Load the pressure and velocity data in Python from the specified paths.
2. Reshape and preprocess the data to prepare it for input into the LSTM network. This includes reshaping the pressure data to match the expected input shape of the LSTM and performing standard scaling on both the pressure and velocity data.
3. Build the LSTM model using the Sequential API of TensorFlow's Keras. The model consists of LSTM layers followed by densely connected layers with various activation functions.
4. Compile the model by specifying the loss function ('mean squared error') and optimizer ('adam').
5. Define early stopping criteria to monitor the validation loss and stop training if the loss doesn't improve after a certain number of epochs.
6. Train the model on the input data and target output using the fit() function. The training data is split into training (80%) and validation sets (20%), and the early stopping criteria are applied.
7. Evaluate the trained model on the test set using the evaluate() function.
8. Save the trained model to a file.
9. Predict the output on the test set and calculate the mean squared error (MSE) between the predicted and actual values.

10. Plot the training and validation loss over the epochs using the matplotlib library.

IV.3.11 Prediction Process

In the prediction phase, the saved model is loaded, and new input vectors (wall pressure) are provided. The trained model, which contains the coefficients, equations, and memories of the LSTM model, processes these inputs and generates the corresponding output matrices representing the velocity field.

1. Load the Saved Model: The trained LSTM model is loaded from the saved .h5 file.
2. Load and Preprocess Pressure Data: New wall pressure data is loaded and preprocessed as required.
3. Predict Velocity Field: The model uses the input pressure data to predict the velocity field.
4. Save Predicted Data: The predicted velocity fields are saved to files for further analysis.

IV.3.12 Hyperparameters Used in the Neural Network

We employed several hyperparameters to optimize the performance of our LSTM neural network:

- **Learning Rate:** Controlled by the Adam optimizer, which adaptively adjusts the learning rate during training to ensure efficient convergence.
- **Number of Layers and Neurons:** The model includes one LSTM layer with 16 units, followed by four dense layers with 32, 128, 512, and 1600 units, respectively. This configuration was chosen to balance model complexity and performance.
- **Batch Size:** Set to 32, which determines the number of samples processed before the model's internal parameters are updated.
- **Epochs:** Set to 1000, defining the number of complete passes through the training dataset. Early stopping was implemented to prevent overfitting, halting training when validation loss ceased to improve.
- **Activation Function:** The ReLU (Rectified Linear Unit) activation function was applied to the dense layers, enabling the model to learn complex, non-linear relationships in the data by allowing for a broader range of outputs.

IV.4 Results and Discussion

IV.4.1 Training Velocity Magnitude with Ten Points of Wall Pressure

Fig IV.5 illustrates the workflow of a machine learning model that uses wall pressure data to predict velocity magnitude. The process begins with the collection of wall pressure measurements at ten (10) points. These measurements, along with corresponding velocity magnitude data, are used to train an LSTM neural network. Once trained, the model can predict the velocity magnitude using only the wall pressure points as input. The diagram effectively demonstrates the input-output relationship and the role of the machine learning model in transforming wall pressure data into meaningful velocity predictions. Training a model consisting of 3000 datasets has given promising results. The training process resulted in a minimal loss of 5.10%, showcasing the model's ability to effectively learn from the provided data. Furthermore, during the validation phase, the model demonstrated a slightly higher loss of 8.48%, as shown in fig IV.6, which remains within acceptable limits. When applied to predict instantaneous snapshots of velocities, the model exhibited accurate predictions, successfully preserving the correct topology of the contours as demonstrated in fig IV.7. The MSE is estimated to 13.486%, to be within acceptable values. Although there is a small difference in the actual velocity values, the overall topology remains accurate. The positions of shedding and vortex formations are correctly predicted, which is critical for our objective. Achieving higher precision would require a substantial amount of data and more powerful computational resources. These outcomes suggest that the trained model is robust and capable of capturing the underlying patterns within the data. In fig IV.8, spectral analyses were conducted for both the original velocity data and the predicted normal velocity. Remarkably, the spectral plots exhibit striking similarities, particularly in the peaks (the Strouhal number adjacent to 1 and at low frequencies 0.1). This quantitative agreement underscores the reliability of our predictions, providing strong confirmation of the presence of instabilities in both the original and predicted datasets.

IV.4.2 Training Reduced Order Velocity Field with Wall Pressure

In the Mode 1 contour, we observed a distinct oscillation in the shear layer, which is clearly visible in fig IV.9. We observed a bulb that narrows and expands, with oscillations reaching a minimum negative value between $x/h = 1.8$ and $x/h = 3.5$. This dynamic is the most significant and important in the separated flow dynamics on BFS. Targeting control of this specific dynamic could yield valuable results, enhancing overall performance and reducing drag forces.

The quantification of this oscillation using spectral analysis revealed a frequency of approximately 5 oscillations per second. Remarkably, this observed frequency closely corresponds to the Strouhal number of 0.12, a frequency associated with flapping dynamics as reported in the existing literature. Consequently, our analysis suggests that the dominant

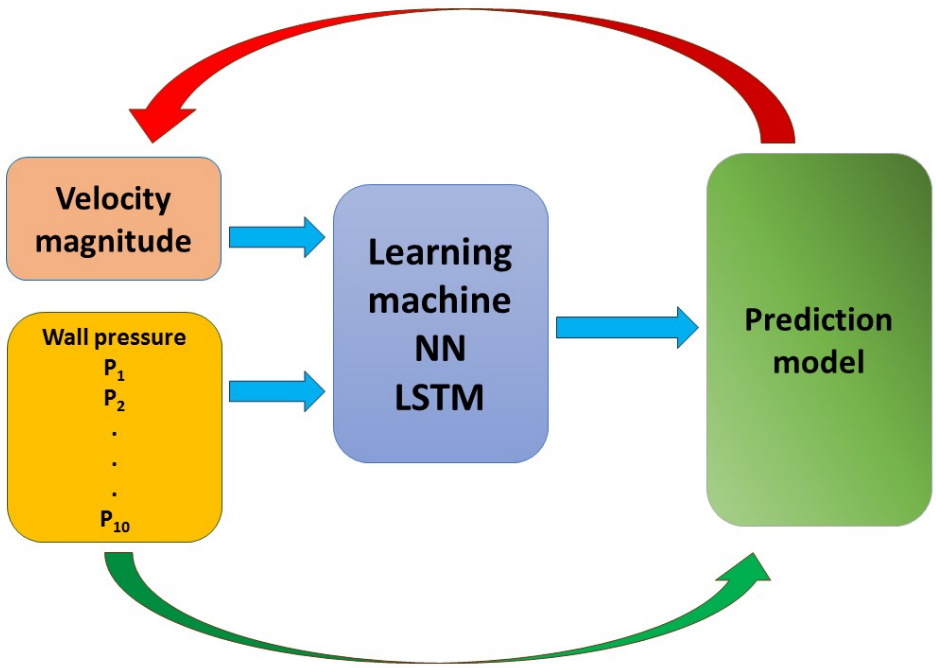

FIGURE IV.5: Machine learning model with velocity field and ten wall pressure points.

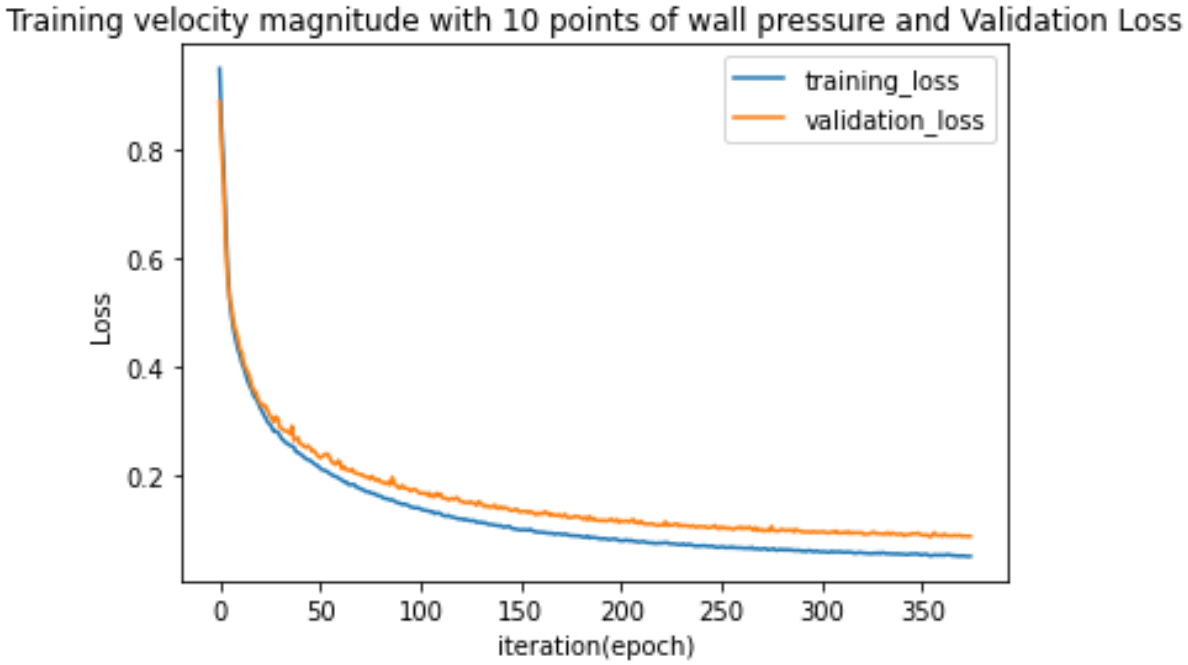

FIGURE IV.6: Training velocity magnitude with 10 points of wall pressure.

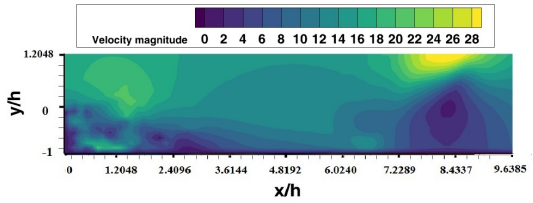

(A) Original velocity magnitude contour at t instant.

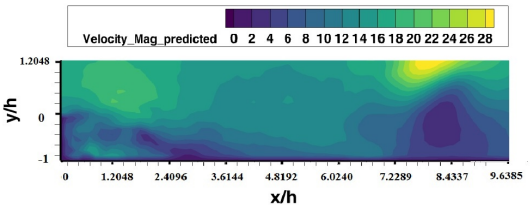

(B) Predicted velocity magnitude contour at t instant.

FIGURE IV.7: Predicting velocity magnitude contour with ten points of wall pressure at the same instant.

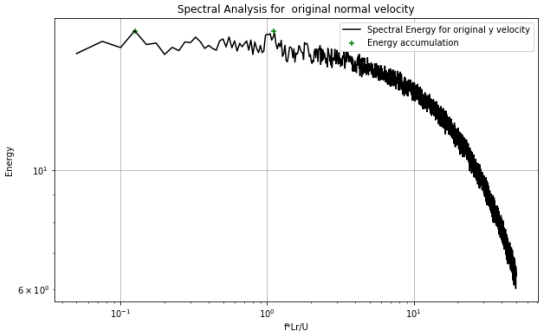

(A) Non-dimensional power spectra of fluctuating normal original velocity measured at $x/h = 1.5$ at $Re_h = 89100$.

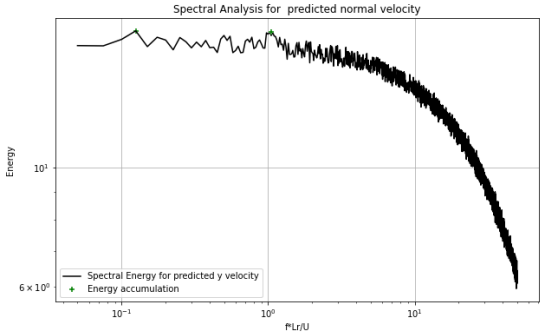

(B) Non-dimensional power spectra of fluctuating normal predicted velocity measured at $x/h = 1.5$ at $Re_h = 89100$.

FIGURE IV.8: Non-dimensional power spectra of fluctuating normal velocity for original and predicted values measured at $x/h = 1.5$ at $Re_h = 89100$.

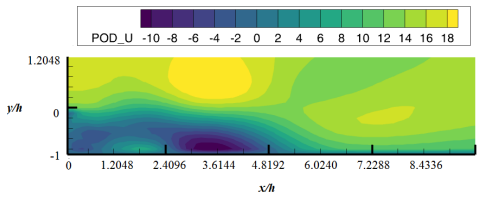

(A) POD X velocity mode 1 at t_1.

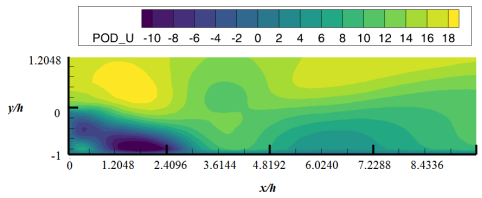

(B) POD X velocity mode 1 at t_2.

FIGURE IV.9: Contours at different instants of reduced order at Mode 1 of X velocity.

dynamic behavior captured in POD Mode 1, as shown in fig IV.10, is primarily representative of the flapping instability. Fig IV.11 illustrates a machine learning model enhanced

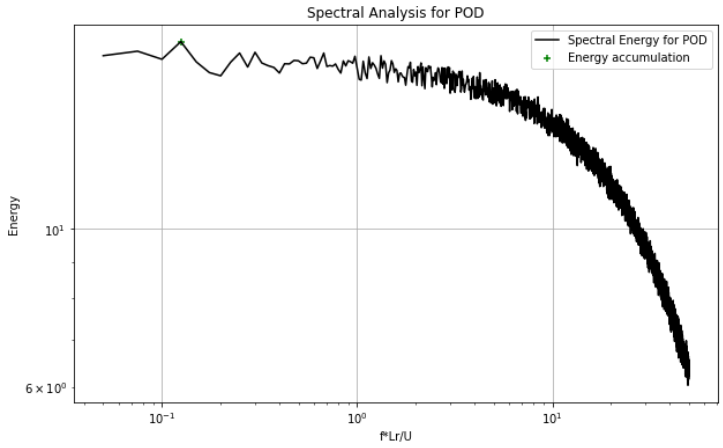

FIGURE IV.10: Non-dimensional power spectra of fluctuating reduced order X Velocity (POD Mode 1) measured at $x/h = 1.5$ for our current study at $Re_h = 89100$.

with POD for greater accuracy, designed to predict low-order velocity using wall pressure data. Initially, wall pressure measurements and X velocity data are collected. The X velocity data undergoes POD to reduce the dynamics' dimensionality while preserving its most significant features. This step makes the data more manageable and improves the performance of the machine learning model. The reduced data and the wall pressure measurements are then used to train an LSTM neural network. Once trained, the model can predict the low-order velocity using only the wall pressure points as input. The training process resulted in a minimal loss of 5.35%, and the validation loss was 9.08% as shown in fig IV.12, which remains within acceptable limits. Notably, the model exhibited accurate predictions, successfully preserving the correct topology of the reduced order of X velocity contours at different instants, as demonstrated in fig IV.13. The MSE is estimated to 5.064%. Also, spectral analysis for predicted reduced order X velocity showed a good agreement with the original one (fig IV.14).

IV.4.3 Study of the Best Region of Wall Pressure Measurement for Prediction

In this part, we use three-point combinations of wall pressure that predict velocity with less mean squared error (MSE). We chose three points to see that the combination of different places (such as vertical and horizontal walls) of measurements is necessary to get maximum information.

1. **Dataset Preparation:** Collect the dataset that includes wall pressure measurements and corresponding velocity values.
2. **Feature Selection:** Select the three points (by combining three from the ten points defined before) for predicting velocity based on wall pressure.

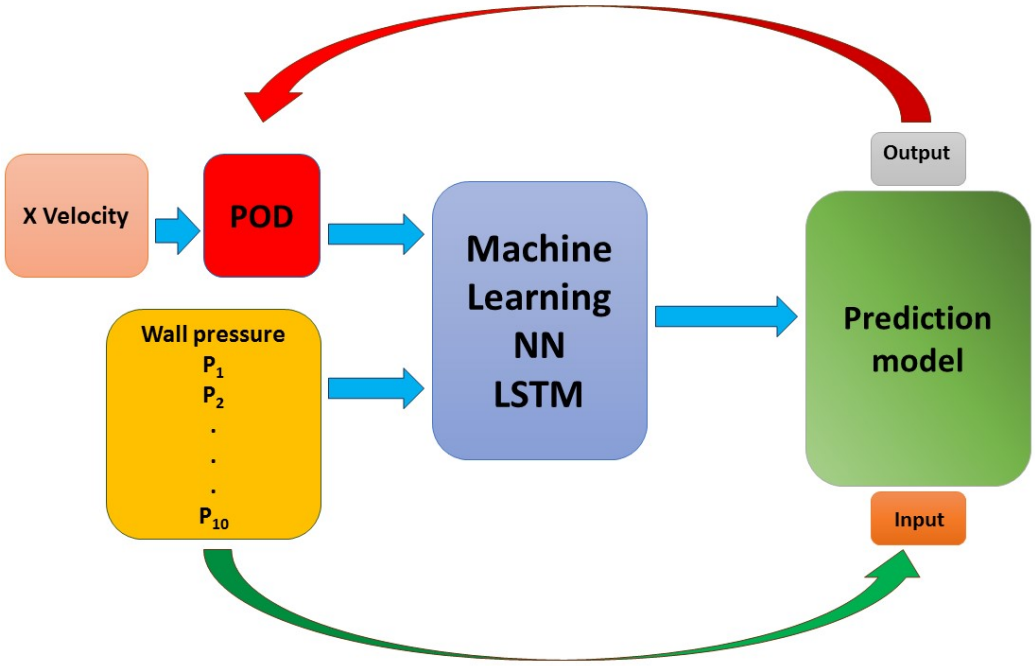

FIGURE IV.11: Machine learning model with reduced order longitudinal velocity and ten wall pressure points.

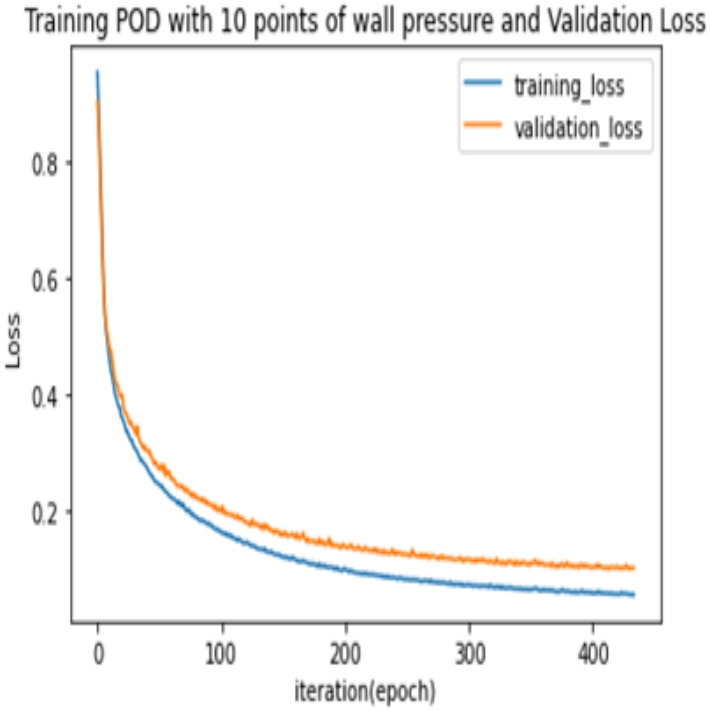

FIGURE IV.12: Training POD with 10 points of wall pressure.

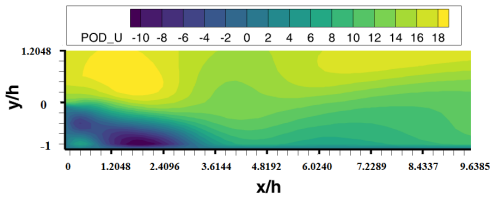

(A) Original POD mode 1 at t_1.

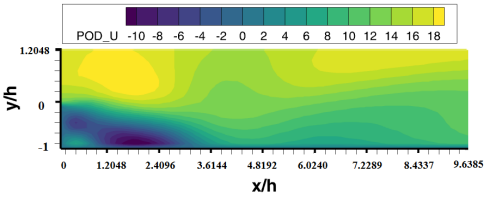

(B) Predicted POD mode 1 at t_1.

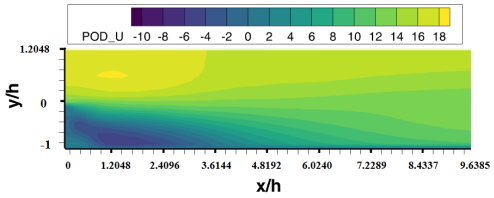

(C) Original POD mode 1 at t_2.

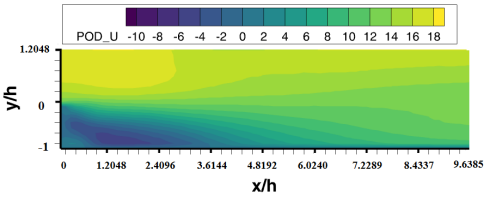

(D) Predicted POD mode 1 at t_2.

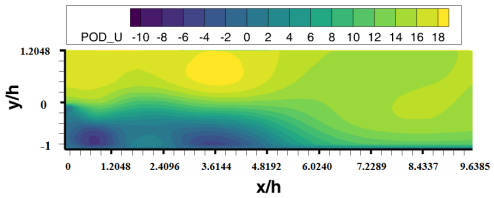

(E) Original POD mode 1 at t_3.

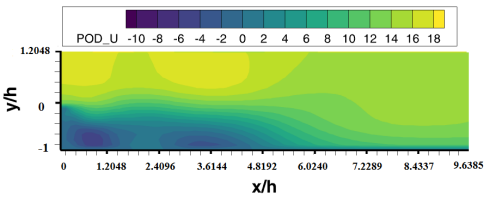

(F) Predicted POD mode 1 at t_3.

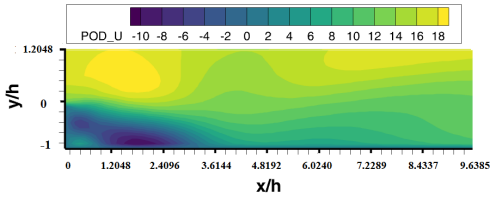

(G) Original POD mode 1 at t_4.

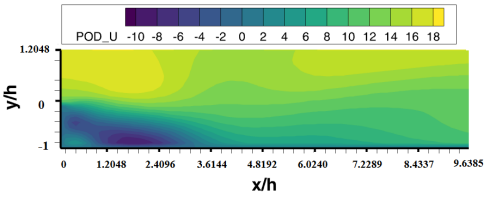

(H) Predicted POD mode 1 at t_4.

FIGURE IV.13: Predicting reduced order X velocity contours with ten points of wall pressure at different instants (t1, t2, t3, t4 stand for different instants of time flow).

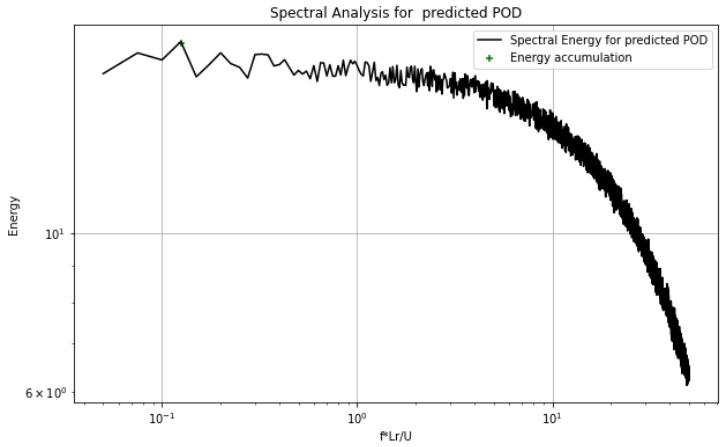

FIGURE IV.14: Non-dimensional power spectra of fluctuating predicted reduced order X Velocity POD mode 1 with ten points of wall pressure at $Re_h = 89100$.

3. **Split the Dataset:** Divide the dataset into training and testing sets. The training set will be used to train the prediction model, while the testing set will be used to evaluate its performance.
4. **Model Training:** Use a regression algorithm to train a model based on the selected three points (features) and the corresponding velocity values in the training set.
5. **Model Evaluation:** Evaluate the trained model's performance using the testing set. Calculate the MSE between the predicted velocity values and the actual velocity values in the testing set.
6. **Iterate and Optimize:** Repeat steps 2–5 with different combinations of three points to find the combination that yields the lowest MSE, using random search to explore different combinations efficiently.
7. **Select the Best Combination:** Compare the MSE values obtained for different combinations and select the one with the lowest MSE as the best combination of three points for predicting velocity based on wall pressure.
8. **Validate the Model:** Once selecting the best combination, validate the model's performance by applying it.

Our comprehensive analysis has led us to a compelling conclusion: the points situated beneath the shear layer (4, 5, 6) as shown in fig IV.15, emerge as the most favorable candidates for constructing combinations of three points that possess a remarkable capability to predict the true dynamics of the system. By focusing on these specific points, we are strategically targeting a region that exhibits a strong correlation with the underlying dynamic behavior. This region, characterized by its proximity to the shear layer, plays a pivotal role in shaping the flow patterns and influencing the overall system dynamics. The spectral analysis was done on the predicted lower-order X velocity (fig IV.16), utilizing the three most favorable wall pressure positions. It displayed a similar peak compared

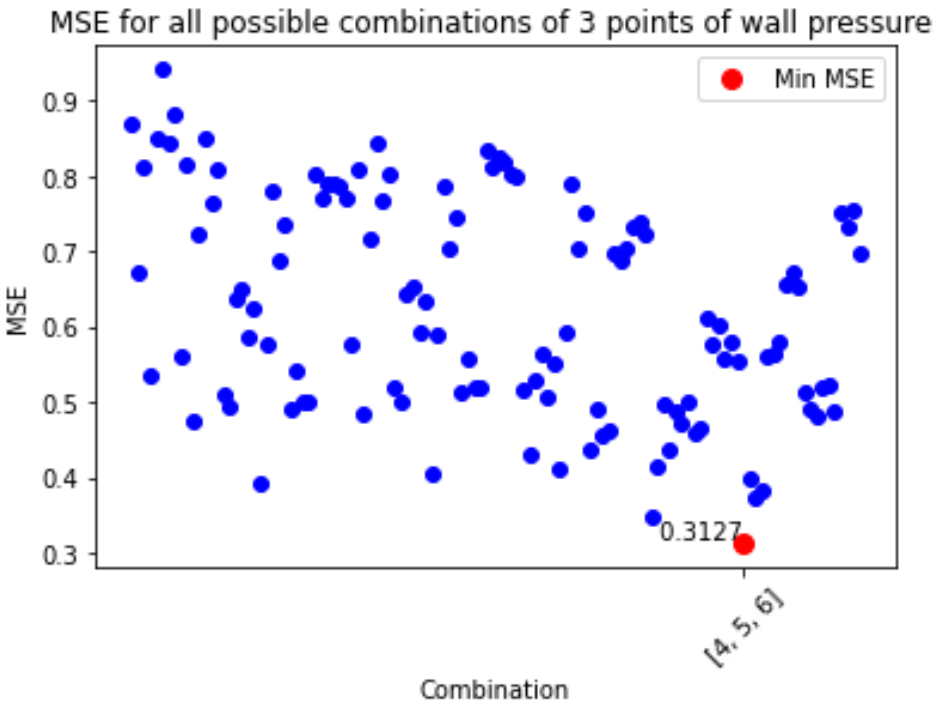

FIGURE IV.15: MSE for all possible combinations of three points of wall pressure.

to the same analysis done on the original dynamics (fig. IV.14) and the anticipated predicted dynamics using ten measurement points (fig IV.13). This peak represents the most significant dynamic in low frequencies, which is the flapping of the shear layer, and its prediction in real-time is sufficient to establish flow control based on feedback information.

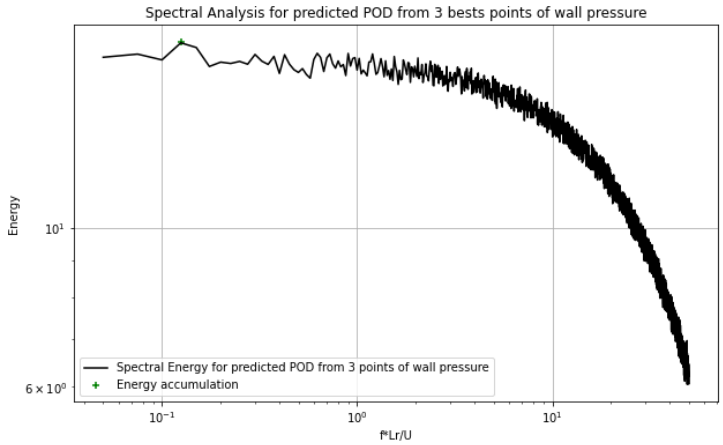

FIGURE IV.16: Non-dimensional power spectra of fluctuating predicted reduced order X Velocity POD mode 1 using three best wall pressure points measured at $x/h = 1.5$ at $Re_h = 89100$.

IV.4.4 Training Reduced Order Vorticity with Wall Pressure

Vorticity is a vital concept as it depends on all velocity components, as shown in equation (IV.1), and is closely linked to wall pressure. (As shown above, both longitudinal and normal velocity are in relation to wall pressure). This relationship makes it a valuable tool for machine learning and flow prediction. Also, shear layer regions are visible through vorticity contours, which offer the ability to effectively control the flow by knowing the position of shear layers.

$$\zeta = \nabla \times V = \left(\frac{\partial v}{\partial x}\right) - \left(\frac{\partial u}{\partial y}\right) \tag{IV.1}$$

Fig IV.17 illustrates a machine learning model designed to predict low-order vorticity using wall pressure data, with enhanced accuracy (POD). The process begins with the collection of X and Y velocity data, which undergoes POD to reduce dimensionality. This reduced data is then used to compute vorticity. Concurrently, wall pressure measurements at points P_4, P_5, and P_6 are collected. These inputs are fed into an LSTM neural network, which is trained using only three wall pressure points. This limited number of measurement points makes the approach particularly useful in practical scenarios where wall pressure sensors are restricted. Once trained, the prediction model can utilize the three wall pressure points to predict low-order vorticity. This method is valuable for real-time applications in flow control. The training phase resulted in a minimal loss of

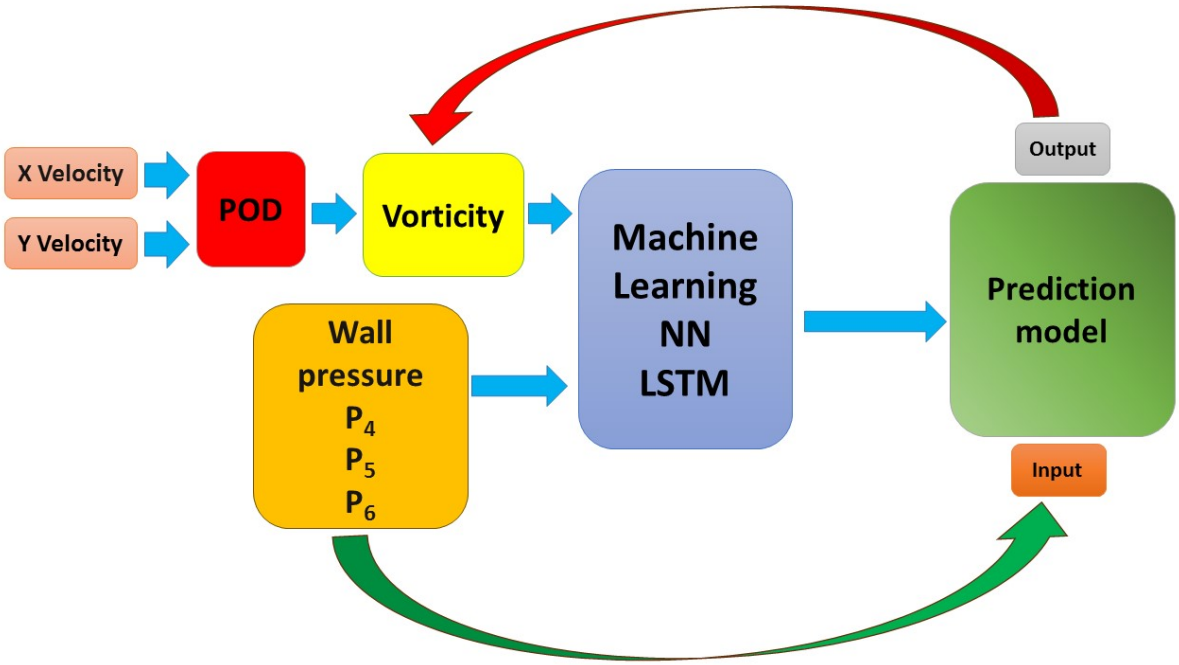

FIGURE IV.17: Machine learning model with reduced order vorticity and best three wall pressure points.

7.33%, with a validation loss of 9.41% (presented in fig IV.18), both within acceptable limits. Importantly, the model demonstrated accurate predictions, maintaining the correct topology of reduced-order vorticity magnitude contours across various instances (see

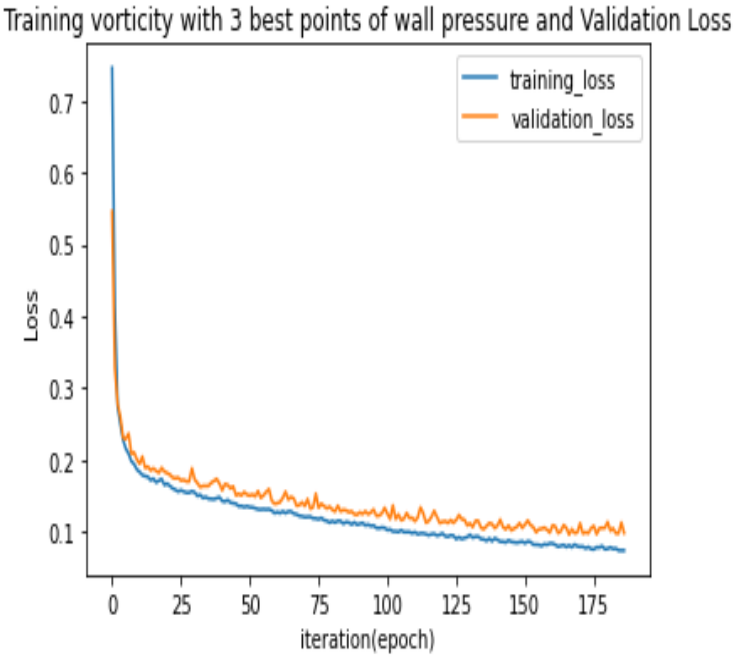

FIGURE IV.18: Training reduced order vorticity magnitude with three best points of wall pressure.

fig. IV.19). The estimated MSE was 23.472%, attributed to the reduced correlation with pressure after partial derivation. This prediction was performed using only three points, indicating that increasing the number of data points could improve accuracy, but it does not impact the topology information. After thoroughly analyzing the predictions of the low-order vorticity dataset across all time instants, we observed that the model consistently and accurately reflects the topology of the vortices. This includes not only the precise positioning of the vortices but also the accurate identification of maximum and minimum value locations. Additionally, the model demonstrated a strong capability in predicting the high vorticity values at the wall immediately after the BFS, which signifies the reformation and strengthening of the new boundary layer. These accurate predictions are indicative of the model's robustness and reliability in capturing the critical aspects of separated flow dynamics. Consequently, we can confidently conclude that using just three wall pressure measurements is sufficient to provide comprehensive information about all the essential dynamics occurring over the BFS across all time instants. Although there is a slight difference between the original and predicted values in terms of scale, the positions of the vortices are highly accurate. This minor discrepancy in value does not affect the overall topology information, which remains correct and reliable. As a result, this difference does not impact the essential data needed for effective feedback control in managing the flow dynamics.

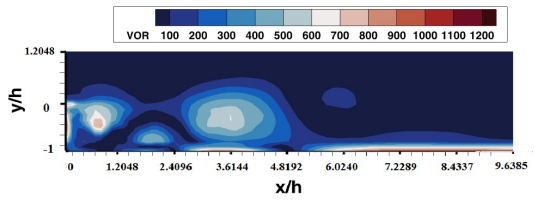

(A) Original reduced order vorticity magnitude at t_1.

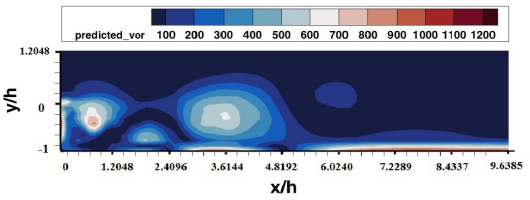

(B) Predicted reduced order vorticity using three best wall pressure points at t_1.

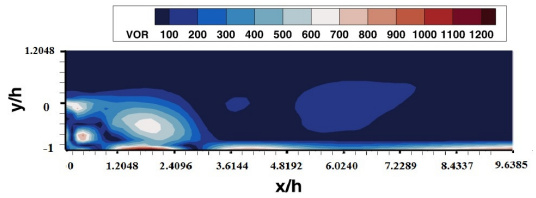

(C) Original reduced order vorticity magnitude at t_2.

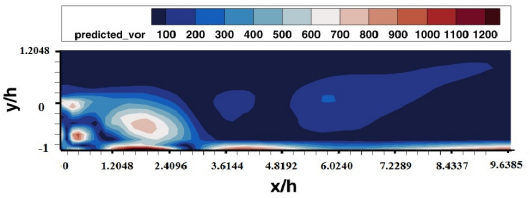

(D) Predicted reduced order vorticity magnitude using three best wall pressure points at t_2.

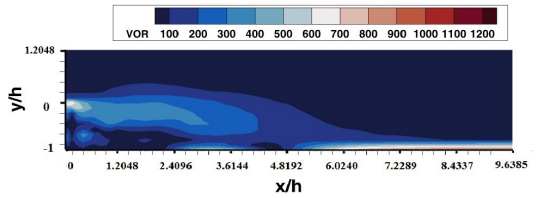

(E) Original reduced order vorticity magnitude at t_3.

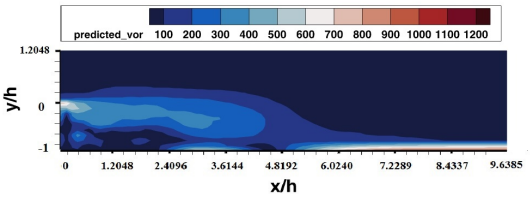

(F) Predicted reduced order vorticity using three best wall pressure points at t_3.

FIGURE IV.19: Prediction of low-order vorticity magnitude using the three best wall pressure points at different time instants (t_1, t_2, t_3). The subfigures compare the original reduced-order vorticity with the predicted reduced-order vorticity at each time step.

V Predictive Analysis of Future Dynamics over Backward-Facing Step

Chapter abstract

This chapter exhibit a relation-ship with the wall pressure points and le velocity field not at the same time but velocity in the future and the past. This can be useful in predicting the future complex flow behavior over the BFS. This knowledge contributes to the advancement of real-time flow control strategies, aiming to prevent separation and improve overall system performance, and offer valuable insights for researchers and engineers engaged in the application of flow control for real-time improvements.

V.1 Introduction

In this chapter, we build upon the work from the previous chapter, but with a crucial modification: the two key variables, wall pressure and velocity, will no longer be considered at the same time instant. Instead, they will be analyzed at different time steps to investigate their temporal dependencies. This shift allows us to better understand how past and future states influence each other, offering deeper insights into the system's dynamics.

To achieve this, we have structured our dataset using a time-shifted approach. Specifically, for both wall pressure and velocity, we have included data from five previous and five future time instances. This enables us to analyze how variations in one variable at a given moment relate to changes in the other variable at different points in time. By doing so, we can establish correlations across time and identify potential causal relationships that might not be evident when considering simultaneous data points.

With this dataset, we apply machine learning techniques to predict future system behavior. The objective is to determine whether a model can accurately forecast upcoming variations in wall pressure and velocity based on past observations. The prediction's accuracy and reliability will be assessed using various performance metrics to evaluate the effectiveness of different learning algorithms.

Beyond evaluating predictive performance, we also explore the broader implications of these findings. If the predictions prove to be sufficiently accurate, this approach could pave the way for real-time forecasting of fluid dynamics, offering potential applications in aerodynamics, turbulence modeling, and control systems. Additionally, we investigate whether long-term trends in system behavior can be inferred from short-term historical data, potentially enabling proactive decision-making in engineering and scientific applications.

Through this study, we aim to answer a fundamental question: can we reliably predict future dynamic behavior based on past and present observations? By leveraging time-shifted correlations and machine learning models, we seek to uncover the extent to which future states of the system can be anticipated, ultimately contributing to a deeper understanding of its underlying mechanics.

V.2 Correlation Study

Before we start looking at machine learning for wall pressure and velocity, it's important to check a correlation study and examine the linear relationship between the variables. This preliminary investigation serves as a basis for determining the predictive capabilities of these models. We conducted individual correlation studies between each point of wall pressure and the corresponding velocity fields (X-velocity and Y-velocity). This analysis was performed for all points of wall pressure along the surface. By examining the correlation between a specific pressure point and the velocity field, we further examine the correlation for future and previous dynamics in pressure over time, specifically at the following time instants: $t + 0.2258s$, $t + 0.1807s$, $t + 0.1355s$, $t + 0.0904s$, $t + 0.0452s$, t, $t - 0.0452s$, $t - 0.0904s$, $t - 0.1355s$, $t - 0.1807s$, and $t - 0.2258s$.

Figures V.1, V.2, V.3, V.4, V.5, V.6, V.7, V.8, V.9, V.10, V.11, V.12 show the correlation with different points of choosen wall pressure at vertical and horizontal wall around the BFS with both longitudinal and normal velocities, at all instants (future and previous and real time). All correlations show a strong correlation ranging from 0.4 to 0.8 at real-time $t = 0$. The correlation gradually decreases with both future and previous events, reaching a minimal correlation value of 0.35 at a specific time offset of approximately ± 0.2258 seconds.

V.3 Machine Learning

Training a model on a dataset comprising 3,000 data points of velocity magnitude fields at different instants—both future and past—along with three wall pressure points has yielded promising results. The training process achieved a minimal loss of **5.10%** in real-time predictions, **25.12%** for future dynamics at $+0.2258s$, and **23.78%** for past dynamics at $-0.2258s$, demonstrating the model's ability to effectively learn from the provided data.

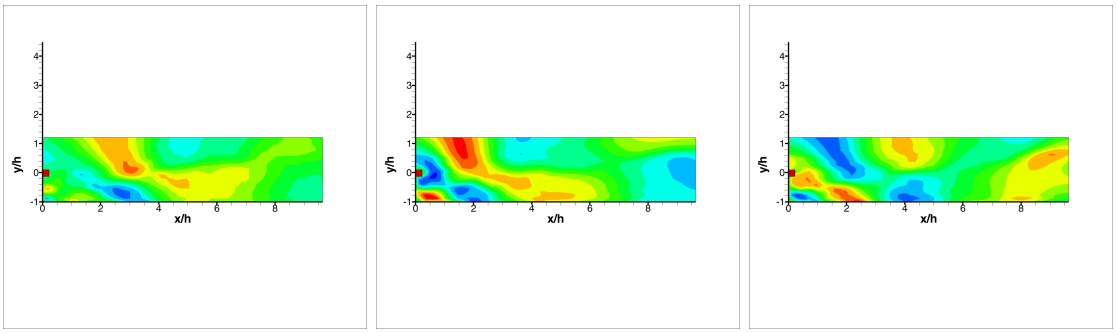

(A) Correlation in t+0.2258s (B) Correlation in t-0.1807s (C) Correlation in t-0.1355s

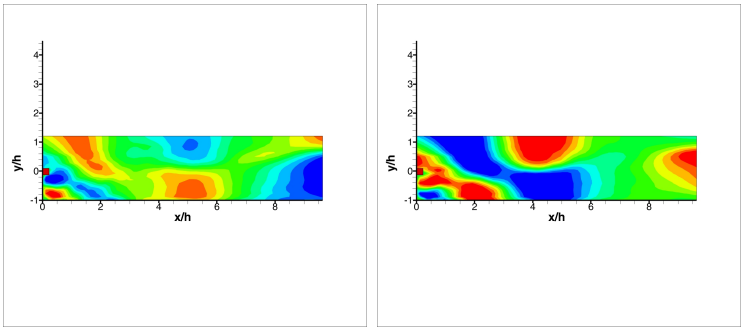

(D) Correlation in t+0.0904s (E) Correlation in t-0.0452s

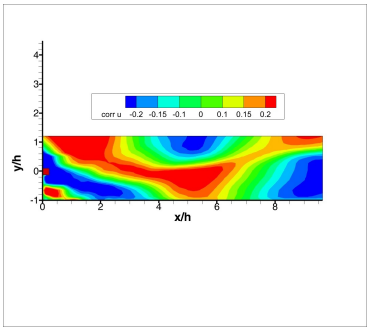

(F) Correlation in real time

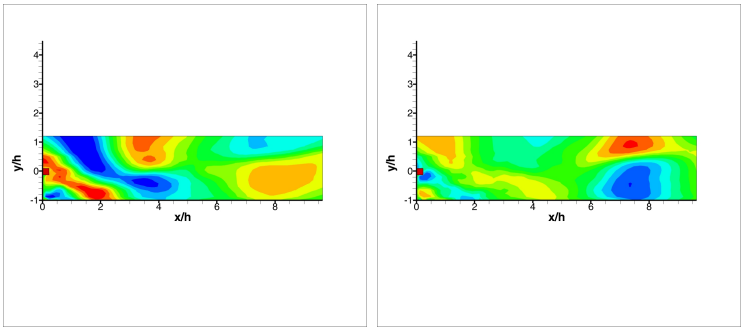

(G) Correlation in t+0.0452s (H) Correlation in t+0.0904s

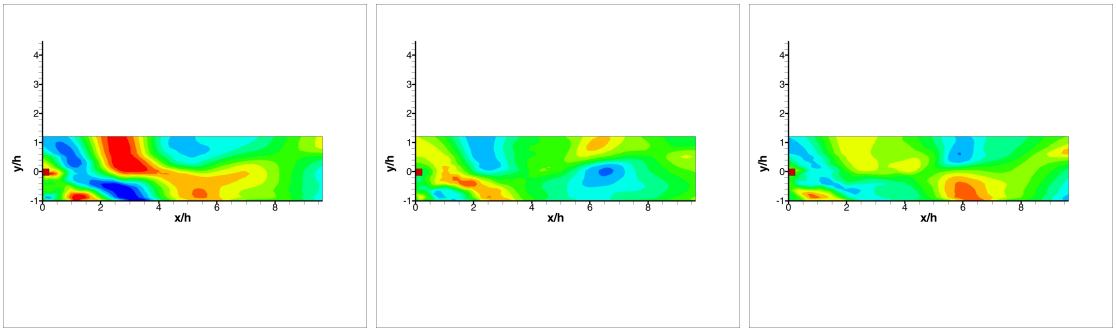

(I) Correlation in t+0.1355s (J) Correlation in t +0.1807s (K) Correlation in t+0.2258s

FIGURE V.1: Correlation with wall pressure point y/h = 0.0 with longitudinal velocity at different instants.

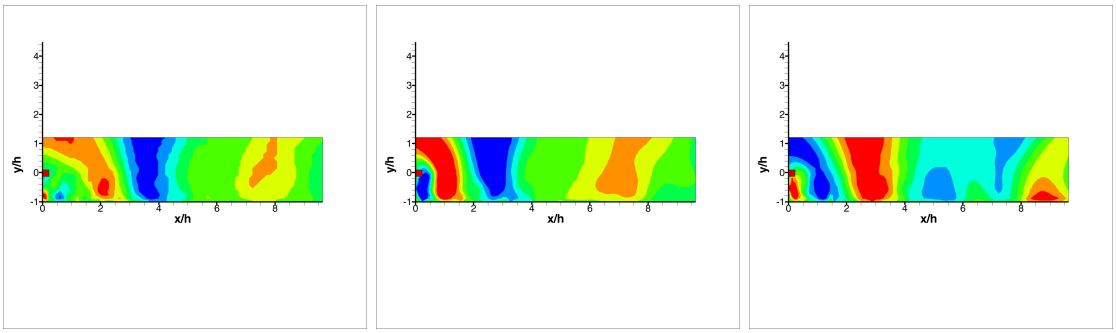

(A) Correlation in t+0.2258s (B) Correlation in t-0.1807s (C) Correlation in t-0.1355s

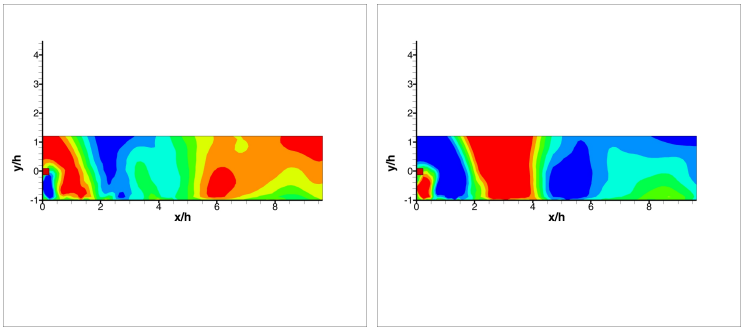

(D) Correlation in t+0.0904s (E) Correlation in t-0.0452s

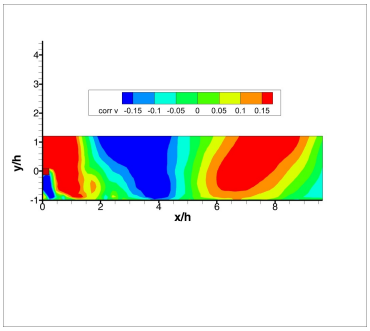

(F) Correlation in real time

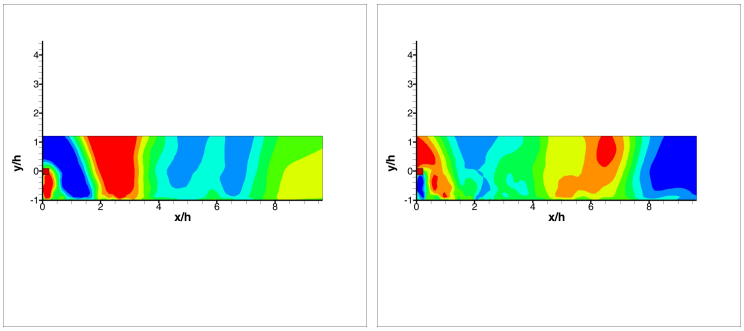

(G) Correlation in t+0.0452s (H) Correlation in t+0.0904s

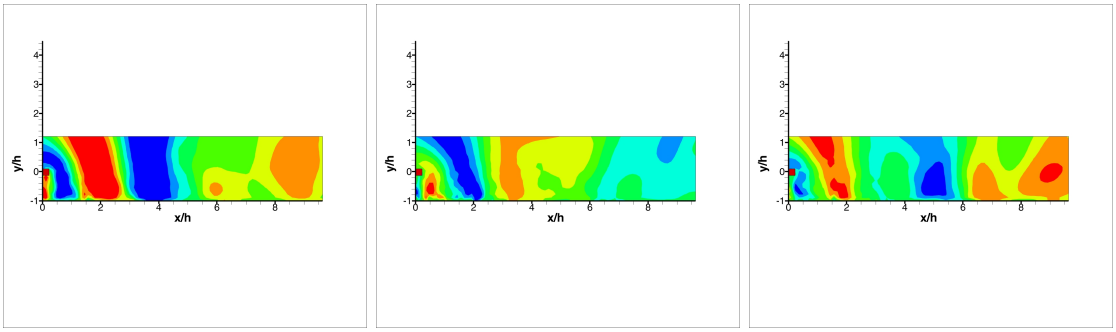

(I) Correlation in t+0.1355s (J) Correlation in t +0.1807s (K) Correlation in t+0.2258s

FIGURE V.2: Correlation with wall pressure point y/h = 0.0 with normal velocity at different instants.

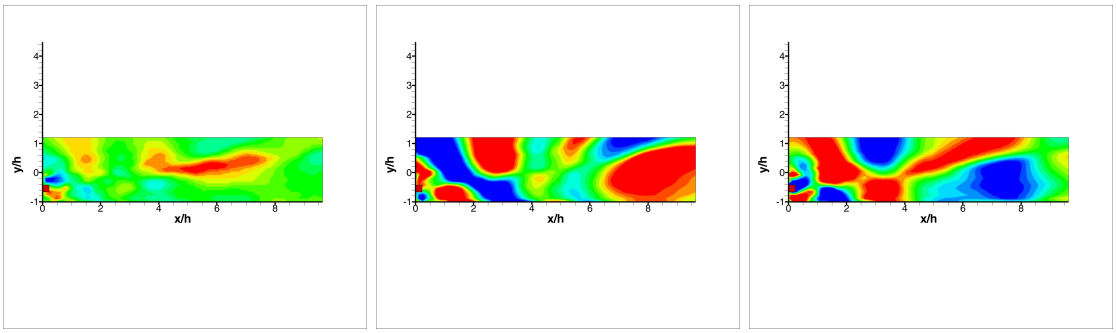

(A) Correlation in t+0.2258s (B) Correlation in t-0.1807s (C) Correlation in t-0.1355s

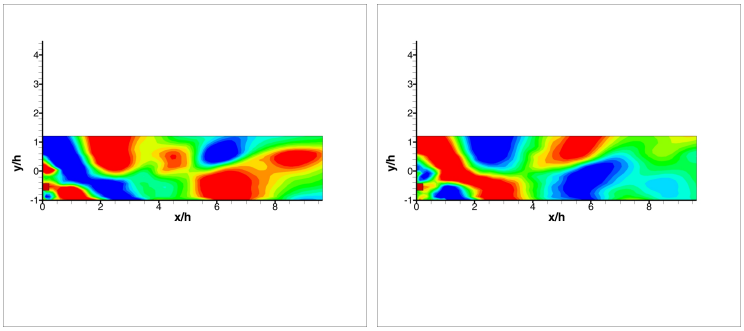

(D) Correlation in t+0.0904s (E) Correlation in t-0.0452s

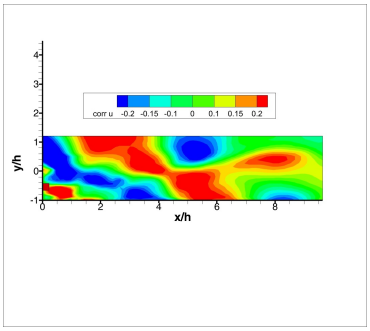

(F) Correlation in real time

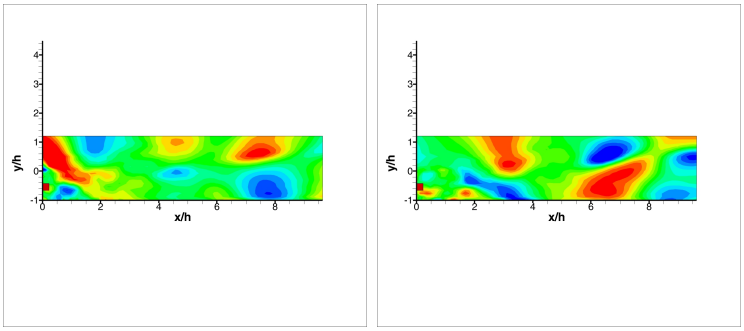

(G) Correlation in t+0.0452s (H) Correlation in t+0.0904s

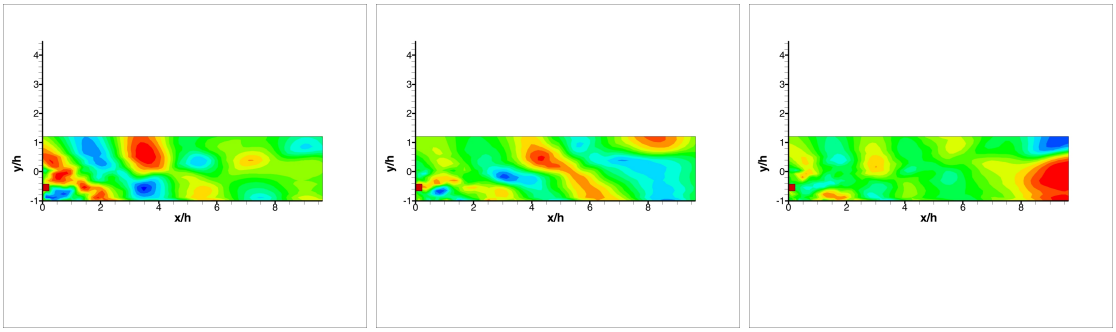

(I) Correlation in t+0.1355s (J) Correlation in t +0.1807s (K) Correlation in t+0.2258s

FIGURE V.3: Correlation with wall pressure point y/h = -0.5 with longitudinal velocity at different instants.

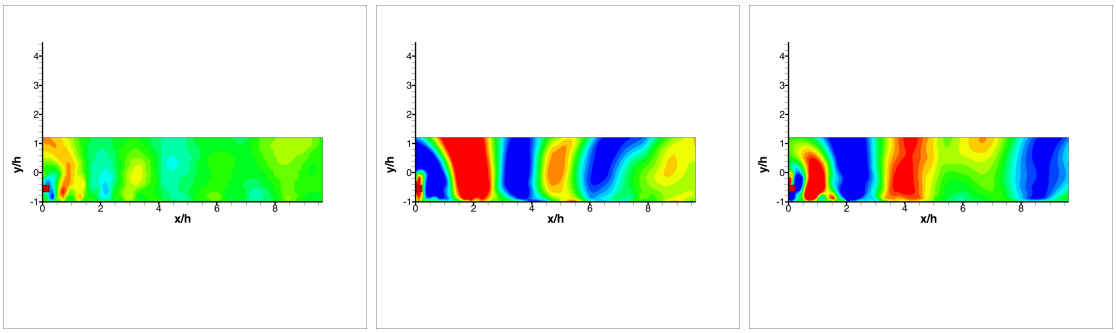

(A) Correlation in t+0.2258s (B) Correlation in t-0.1807s (C) Correlation in t-0.1355s

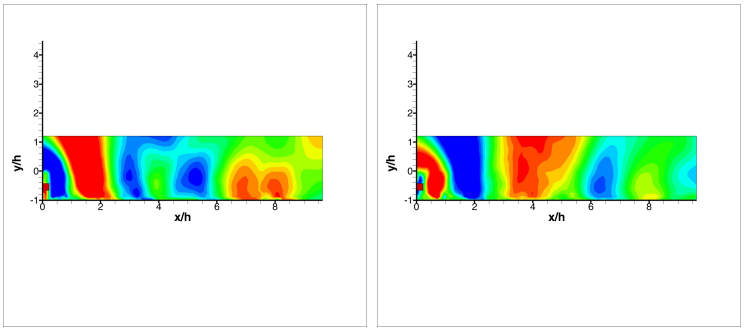

(D) Correlation in t+0.0904s (E) Correlation in t-0.0452s

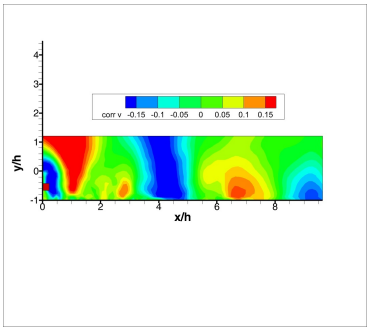

(F) Correlation in real time

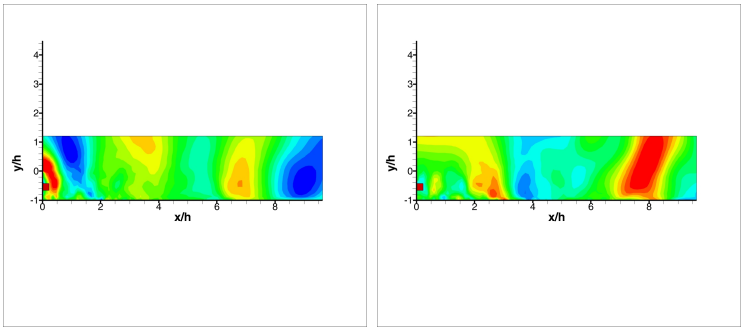

(G) Correlation in t+0.0452s (H) Correlation in t+0.0904s

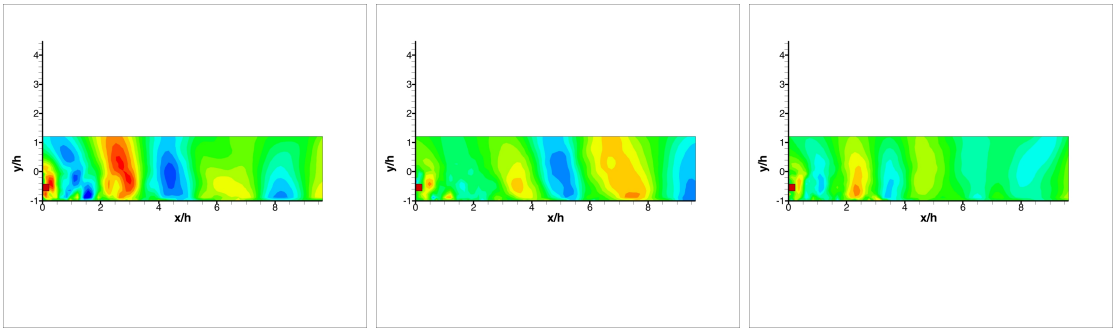

(I) Correlation in t+0.1355s (J) Correlation in t +0.1807s (K) Correlation in t+0.2258s

FIGURE V.4: Correlation with wall pressure point y/h = -0.5 with normal velocity at different instants.

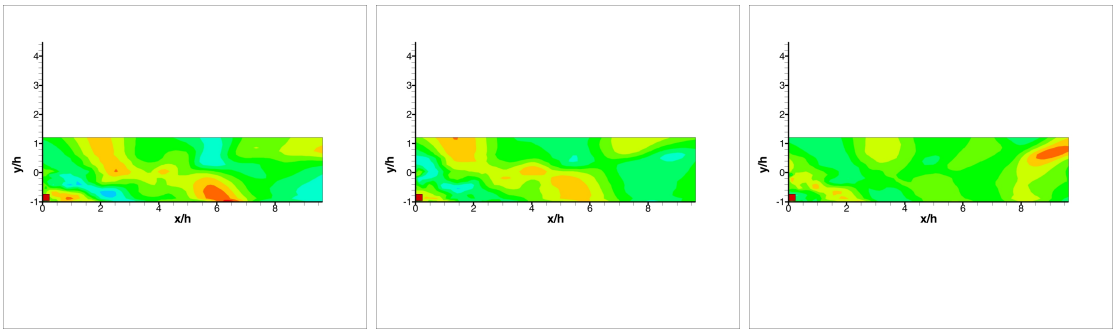

(A) Correlation in t+0.2258s (B) Correlation in t-0.1807s (C) Correlation in t-0.1355s

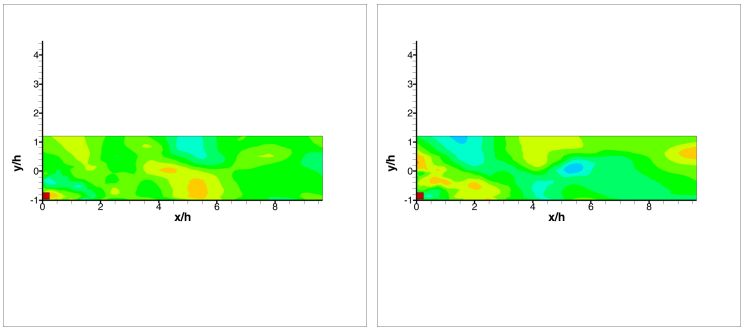

(D) Correlation in t+0.0904s (E) Correlation in t-0.0452s

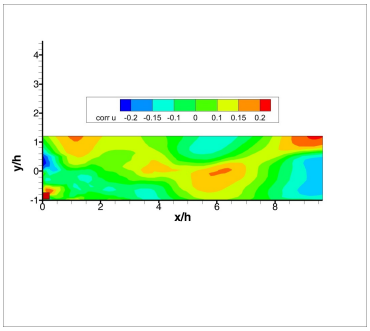

(F) Correlation in real time

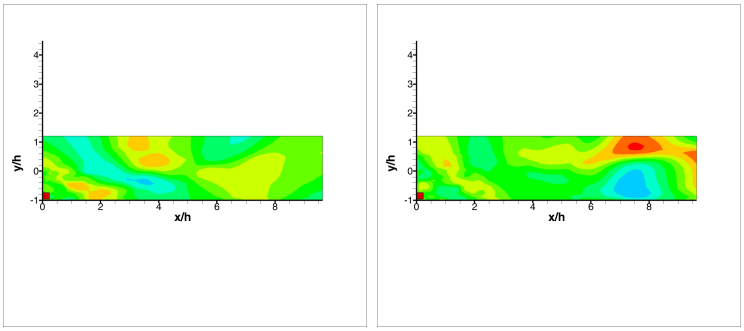

(G) Correlation in t+0.0452s (H) Correlation in t+0.0904s

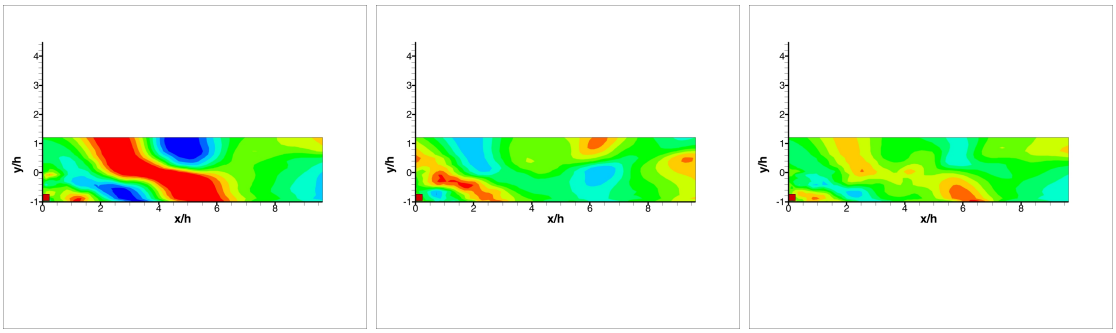

(I) Correlation in t+0.1355s (J) Correlation in t +0.1807s (K) Correlation in t+0.2258s

FIGURE V.5: Correlation with wall pressure point y/h = -1.0 with longitudinal velocity at different instants.

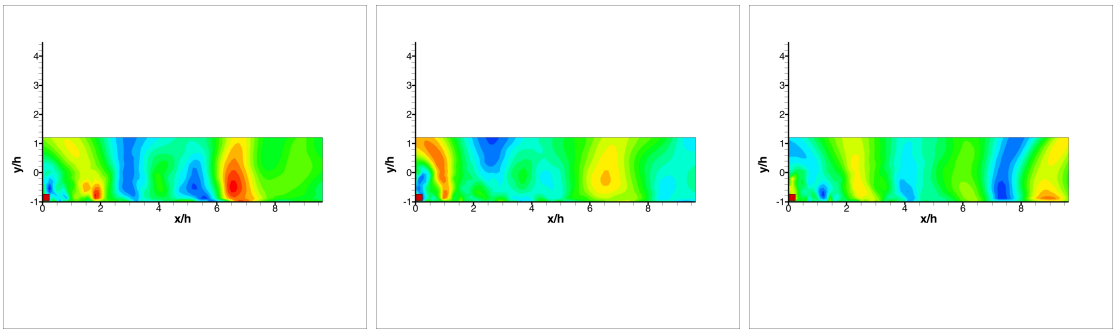

(A) Correlation in t+0.2258s (B) Correlation in t-0.1807s (C) Correlation in t-0.1355s

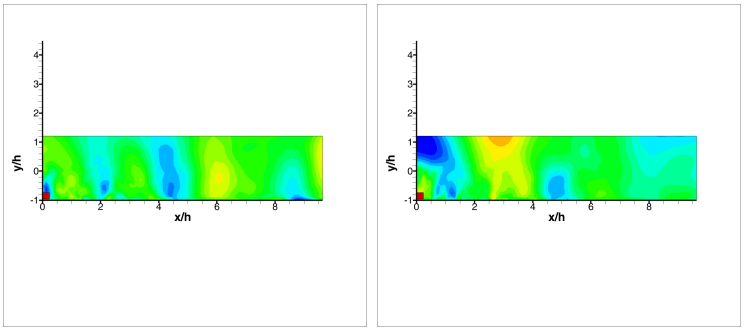

(D) Correlation in t+0.0904s (E) Correlation in t-0.0452s

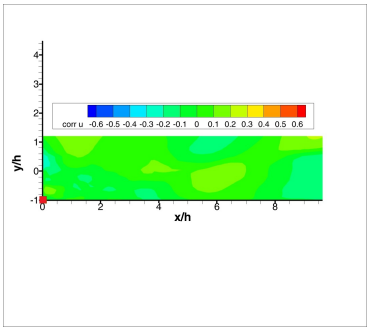

(F) Correlation in real time

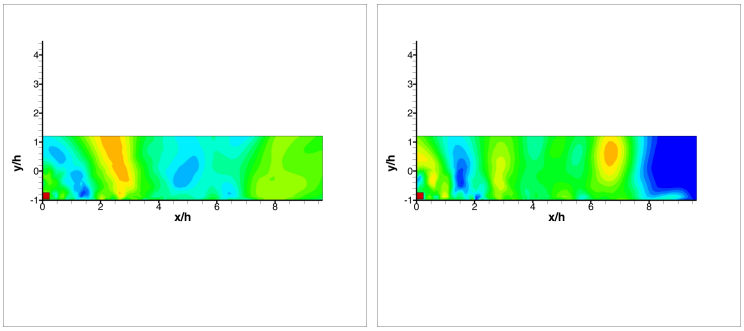

(G) Correlation in t+0.0452s (H) Correlation in t+0.0904s

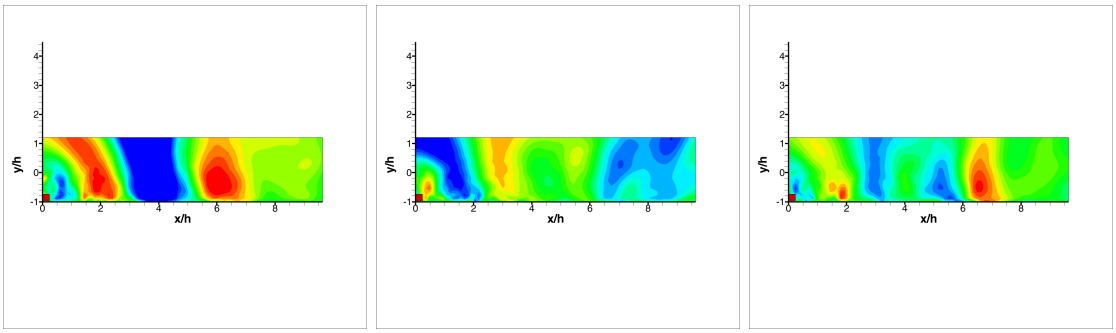

(I) Correlation in t+0.1355s (J) Correlation in t +0.1807s (K) Correlation in t+0.2258s

FIGURE V.6: Correlation with wall pressure point y/h = -1.0 with normal velocity at different instants.

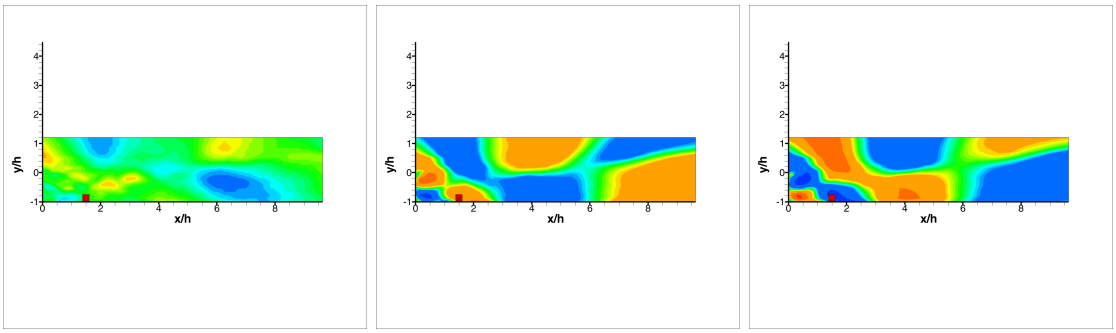

(A) Correlation in t+0.2258s (B) Correlation in t-0.1807s (C) Correlation in t-0.1355s

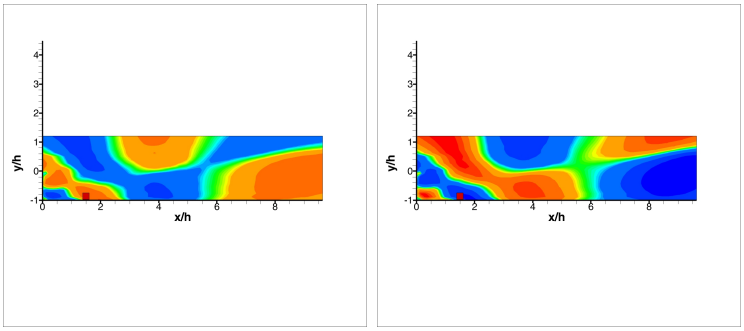

(D) Correlation in t+0.0904s (E) Correlation in t-0.0452s

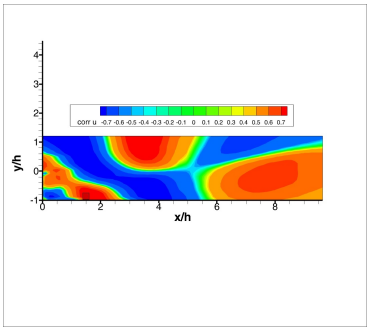

(F) Correlation in real time

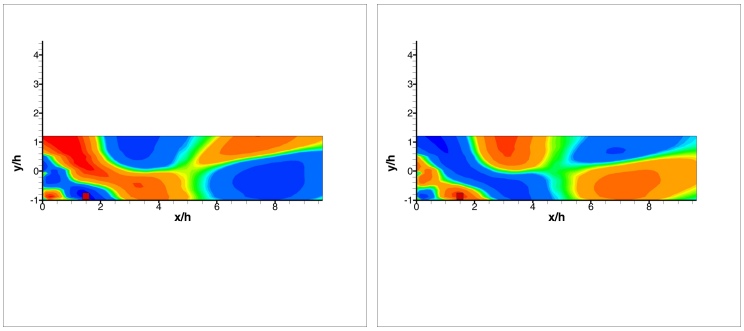

(G) Correlation in t+0.0452s (H) Correlation in t+0.0904s

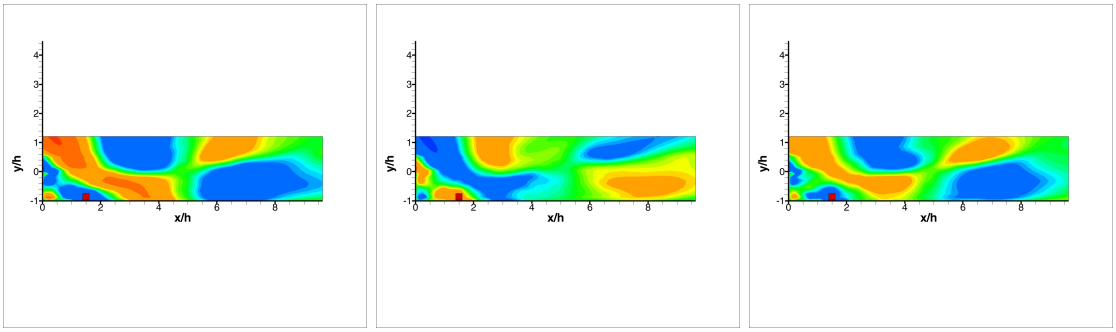

(I) Correlation in t+0.1355s (J) Correlation in t +0.1807s (K) Correlation in t+0.2258s

FIGURE V.7: Correlation with wall pressure point x/h = 1.5 with longitudinal velocity at different instants.

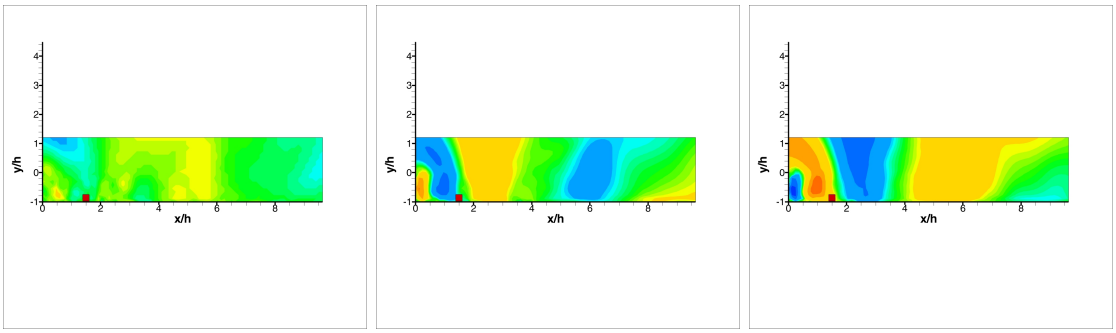

(A) Correlation in t+0.2258s (B) Correlation in t-0.1807s (C) Correlation in t-0.1355s

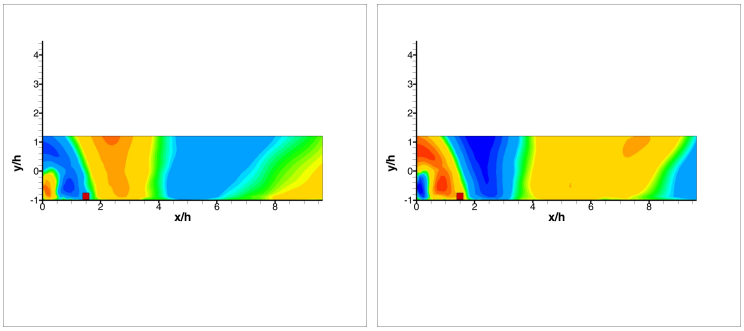

(D) Correlation in t+0.0904s (E) Correlation in t-0.0452s

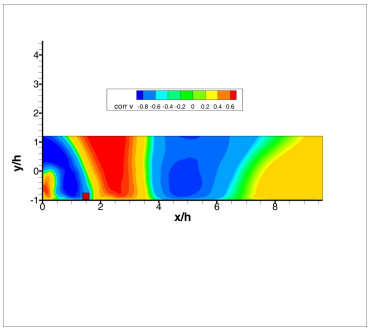

(F) Correlation in real time

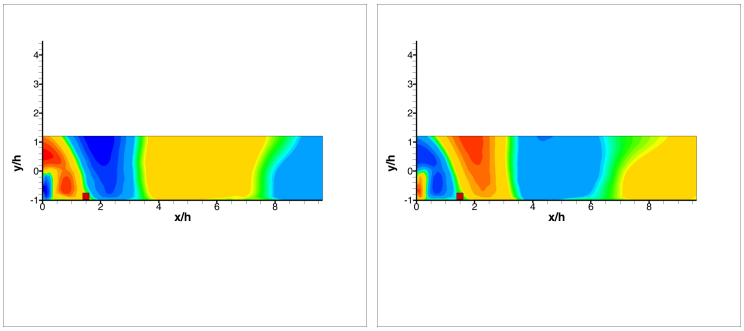

(G) Correlation in t+0.0452s (H) Correlation in t+0.0904s

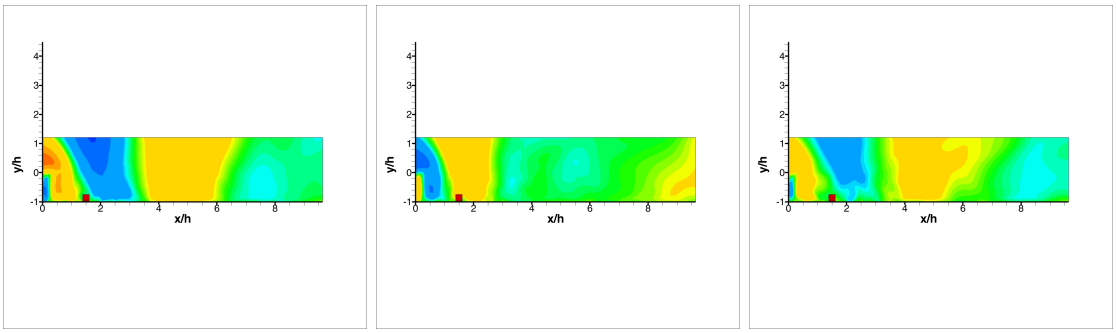

(I) Correlation in t+0.1355s (J) Correlation in t +0.1807s (K) Correlation in t+0.2258s

FIGURE V.8: Correlation with wall pressure point x/h = 1.5 with normal velocity at different instants.

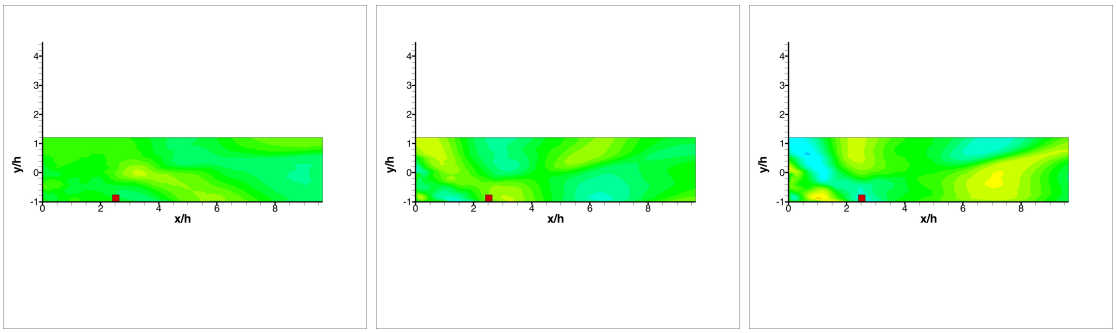

(A) Correlation in t+0.2258s (B) Correlation in t-0.1807s (C) Correlation in t-0.1355s

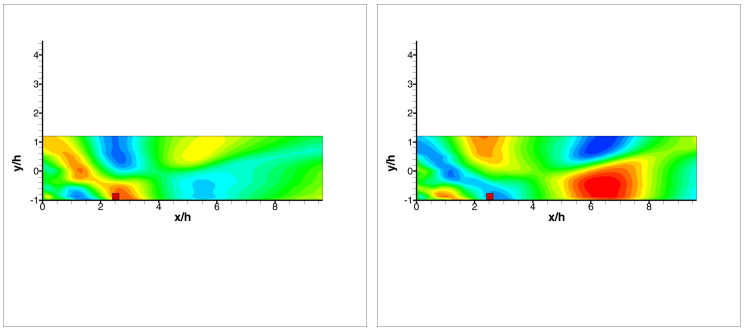

(D) Correlation in t+0.0904s (E) Correlation in t-0.0452s

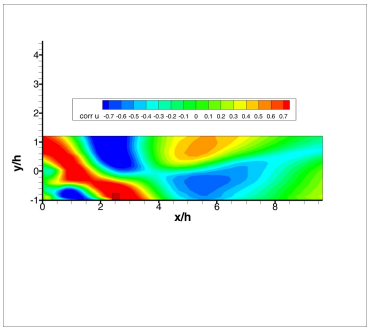

(F) Correlation in real time

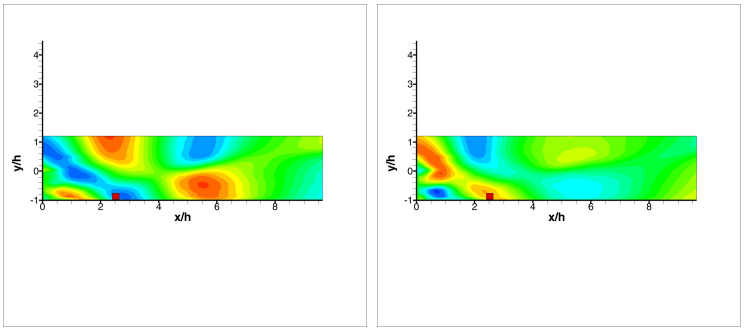

(G) Correlation in t+0.0452s (H) Correlation in t+0.0904s

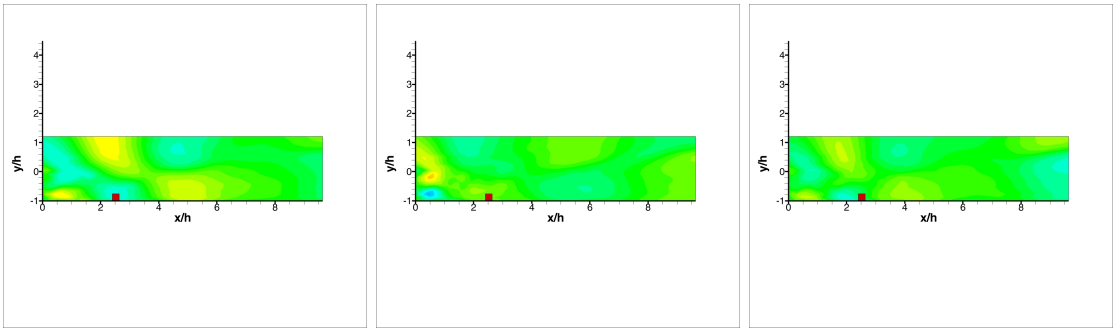

(I) Correlation in t+0.1355s (J) Correlation in t +0.1807s (K) Correlation in t+0.2258s

FIGURE V.9: Correlation with wall pressure point x/h = 2.5 with longitudinal velocity at different instants.

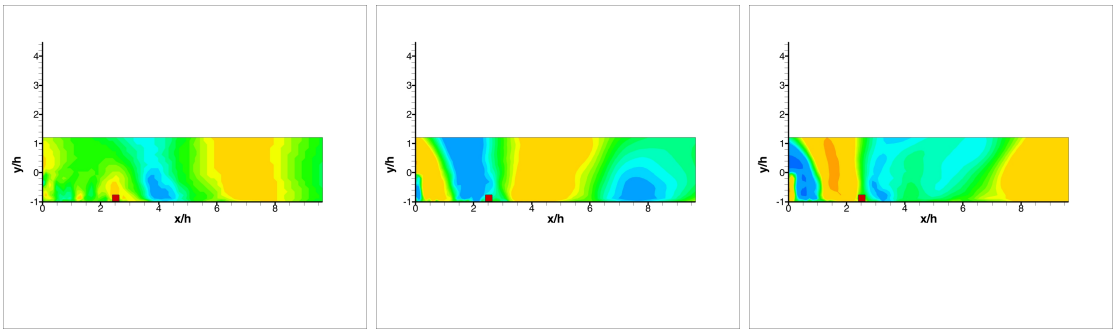

(A) Correlation in t+0.2258s (B) Correlation in t-0.1807s (C) Correlation in t-0.1355s

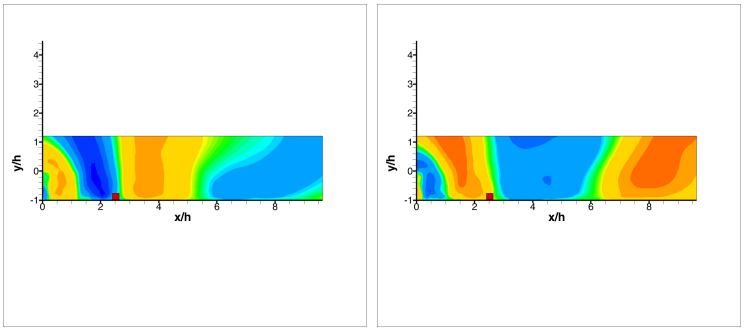

(D) Correlation in t+0.0904s (E) Correlation in t-0.0452s

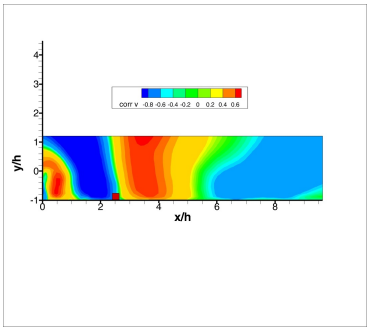

(F) Correlation in real time

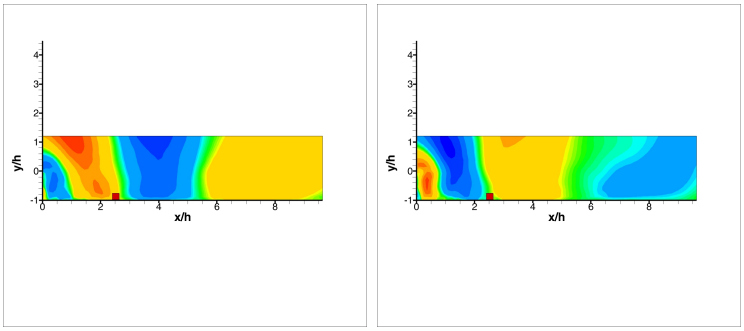

(G) Correlation in t+0.0452s (H) Correlation in t+0.0904s

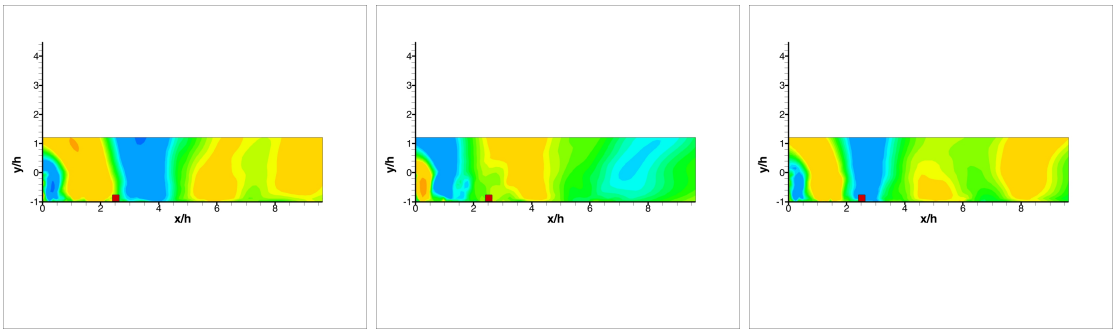

(I) Correlation in t+0.1355s (J) Correlation in t +0.1807s (K) Correlation in t+0.2258s

FIGURE V.10: Correlation with wall pressure point x/h = 2.5 with normal velocity at different instants.

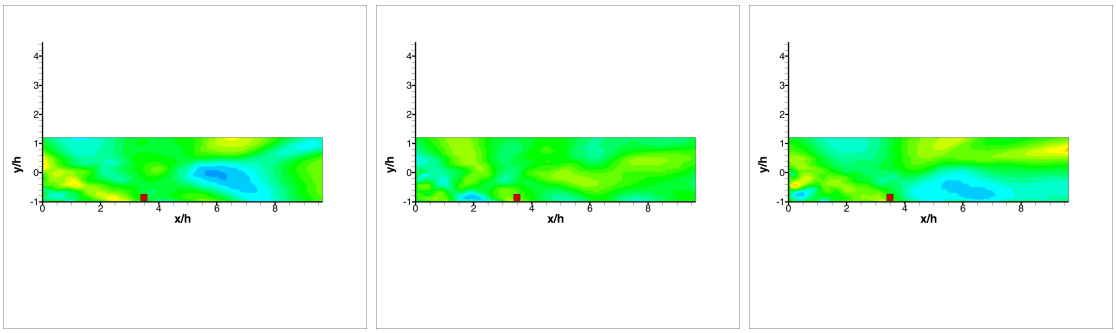

(A) Correlation in t+0.2258s (B) Correlation in t-0.1807s (C) Correlation in t-0.1355s

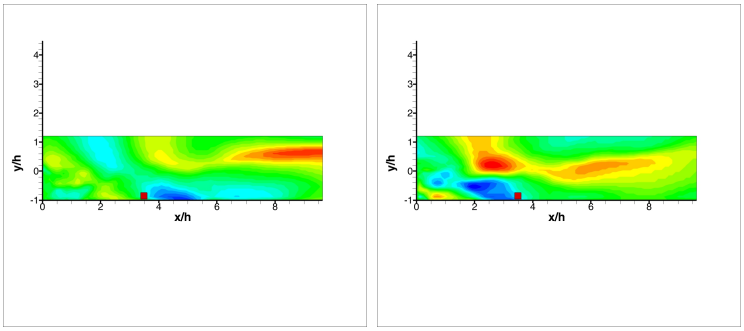

(D) Correlation in t+0.0904s (E) Correlation in t-0.0452s

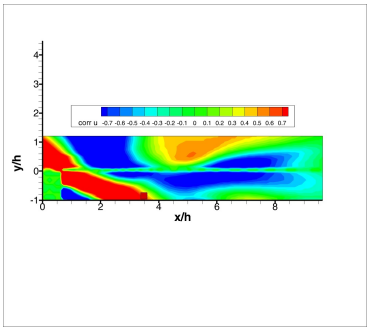

(F) Correlation in real time

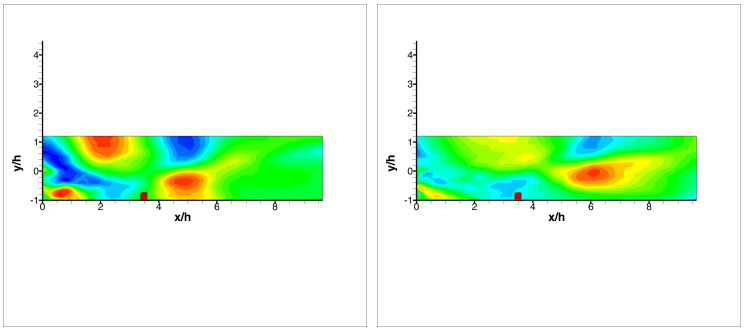

(G) Correlation in t+0.0452s (H) Correlation in t+0.0904s

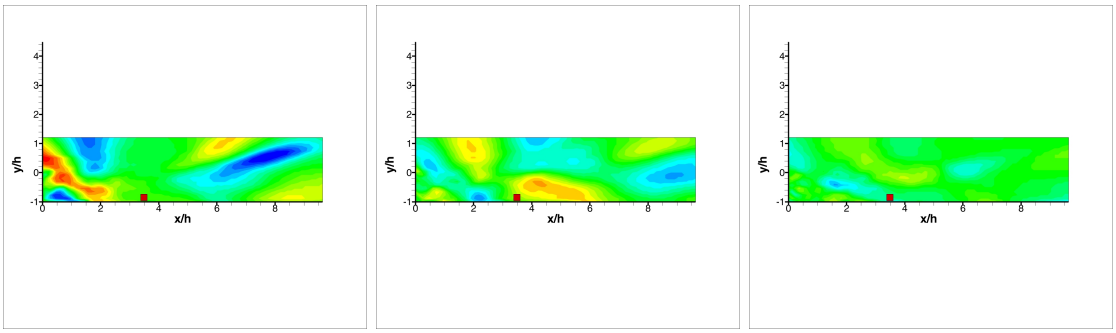

(I) Correlation in t+0.1355s (J) Correlation in t +0.1807s (K) Correlation in t+0.2258s

FIGURE V.11: Correlation with wall pressure point x/h = 3.5 with longitudinal velocity at different instants.

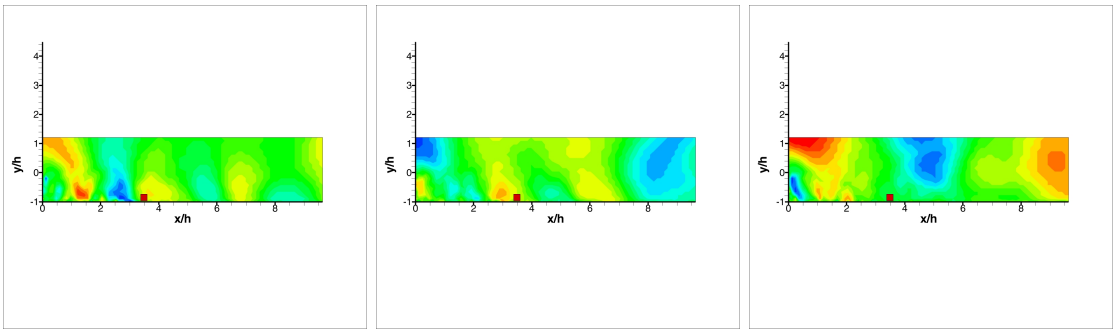

(A) Correlation in t+0.2258s (B) Correlation in t-0.1807s (C) Correlation in t-0.1355s

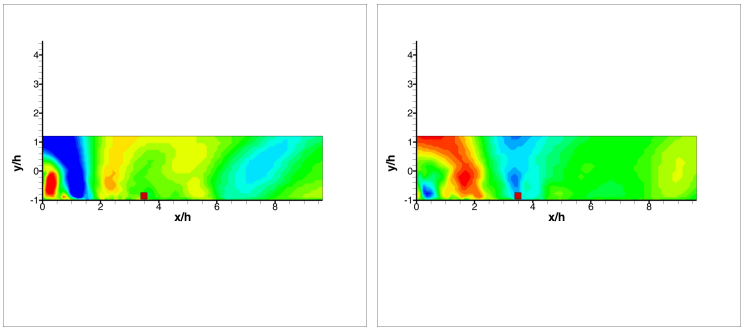

(D) Correlation in t+0.0904s (E) Correlation in t-0.0452s

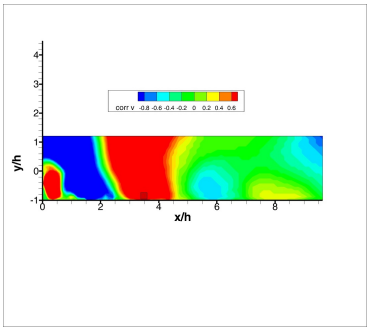

(F) Correlation in real time

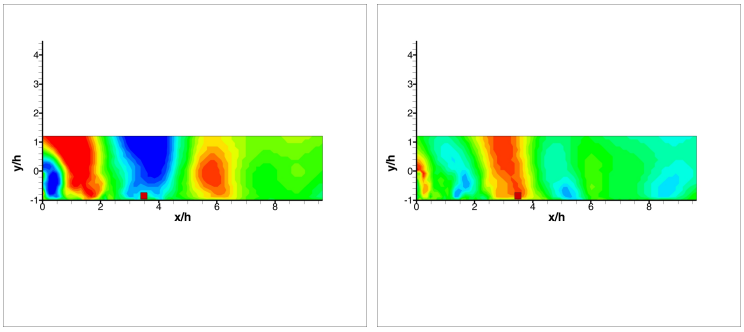

(G) Correlation in t+0.0452s (H) Correlation in t+0.0904s

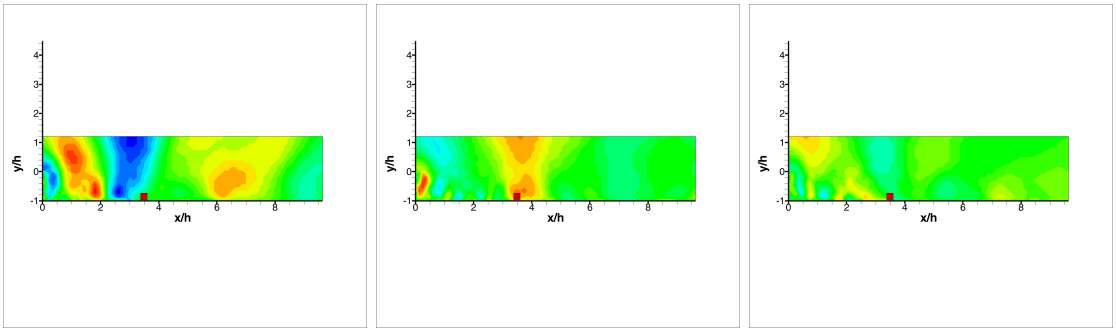

(I) Correlation in t+0.1355s (J) Correlation in t +0.1807s (K) Correlation in t+0.2258s

FIGURE V.12: Correlation with wall pressure point x/h = 3.5 with normal velocity at different instants.

During the validation phase, the model exhibited a slightly higher loss of **8.48%**, which remains within acceptable limits. When applied to predict instantaneous future, past, and real-time snapshots of vorticity, the model accurately preserved the correct topology of the contours, confirming its robustness and ability to capture both real-time and future dynamics.

This study underscores the potential of artificial intelligence, specifically the **RNN LSTM** technique, in predicting velocity fields. By correlating future, past, and real-time velocity fields with wall pressure and analyzing the parietal imprint induced by the recirculation zone, the complete velocity field can be predicted. The results indicate that AI can successfully predict both future and real-time velocity fields using wall pressure data.

Furthermore, the use of **machine learning via RNN LSTM** enables the prediction of the reduced-order vorticity magnitude, a crucial step in developing open-loop control of separated flow on **BFS (Backward-Facing Step)**. This advancement in AI-driven flow prediction has the potential to revolutionize the field of fluid dynamics, paving the way for more efficient and effective control of complex flow phenomena.

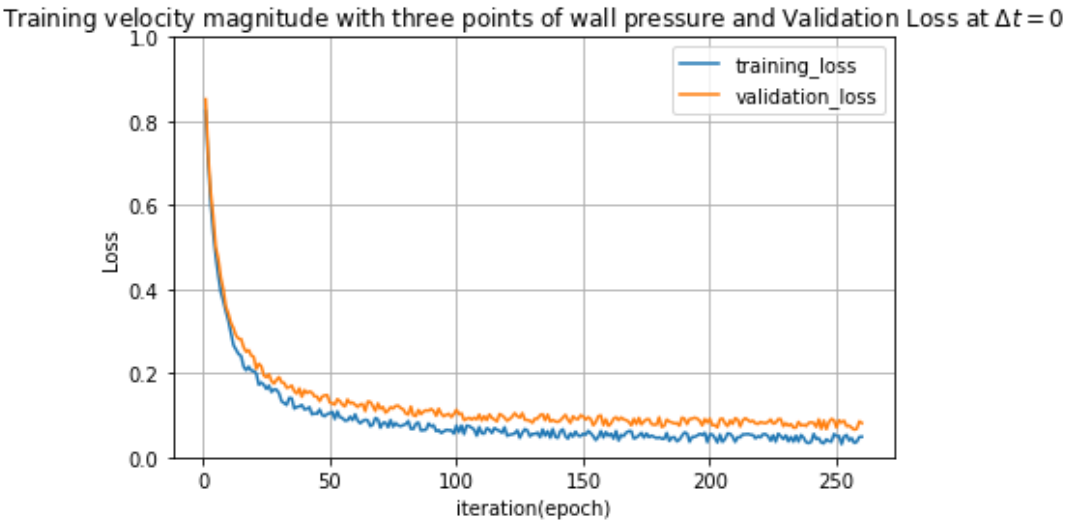

FIGURE V.13: Training velocity magnitude with three points of wall pressure at real time.

Fig V.13: $\Delta t = 0$

- **Observation:** The training and validation loss curves are very close, with minimal divergence throughout the epochs.
- **Interpretation:** This indicates excellent generalization with no temporal shift, as the validation loss is only slightly higher than the training loss.
- **Conclusion:** In real-time ($\Delta t = 0$), the model performs optimally, demonstrating high predictive accuracy with minimal temporal complexity. The model achieves

strong predictive capability, with near-perfect alignment between training and validation losses.

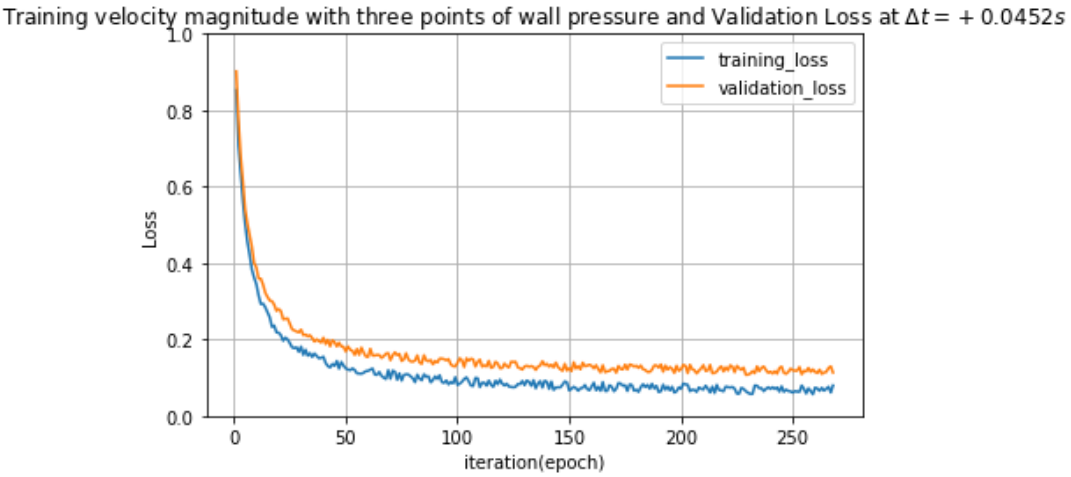

FIGURE V.14: Training velocity magnitude with three points of wall pressure at t + 0.0452s.

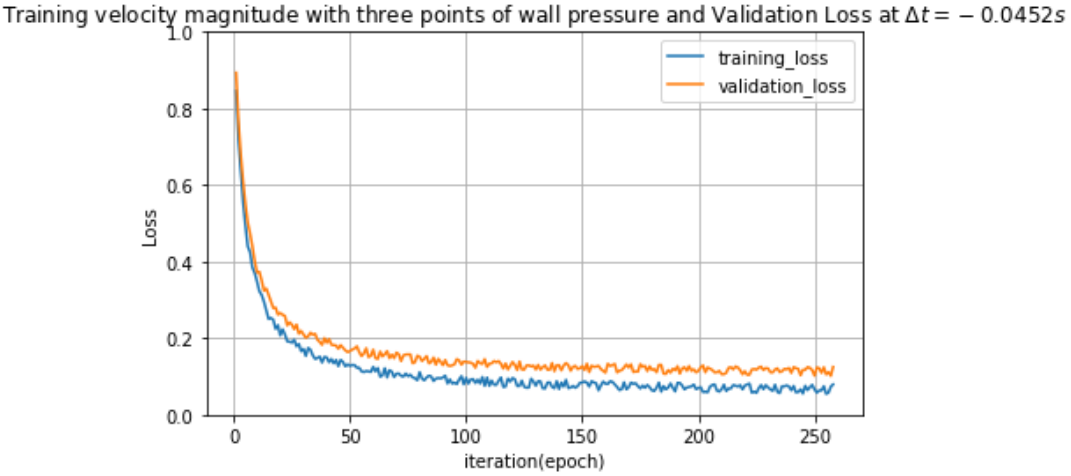

FIGURE V.15: Training velocity magnitude with three points of wall pressure at t - 0.0452s.

Fig V.14: $\Delta t = +0.0452\,\mathbf{s}$

- **Observation:** The validation loss is slightly higher than in $\Delta t = 0$, but the gap between training and validation losses remains small.
- **Interpretation:** The model generalizes well to a small positive temporal shift, maintaining effective prediction of short-term future dynamics.
- **Conclusion:** The model remains effective in predicting future dynamics with a small positive shift, preserving good generalization capabilities and minimal performance degradation.

Fig V.15: $\Delta t = -0.0452\,\mathbf{s}$

- **Observation:** The validation loss increases slightly more than in the baseline case, but the performance remains relatively stable.
- **Interpretation:** A slight negative temporal shift introduces a small decrease in predictive accuracy, but the model still captures the general dynamics effectively.
- **Conclusion:** Despite the small negative shift, the model continues to predict key dynamic patterns well, with only a slight decrease in predictive performance.

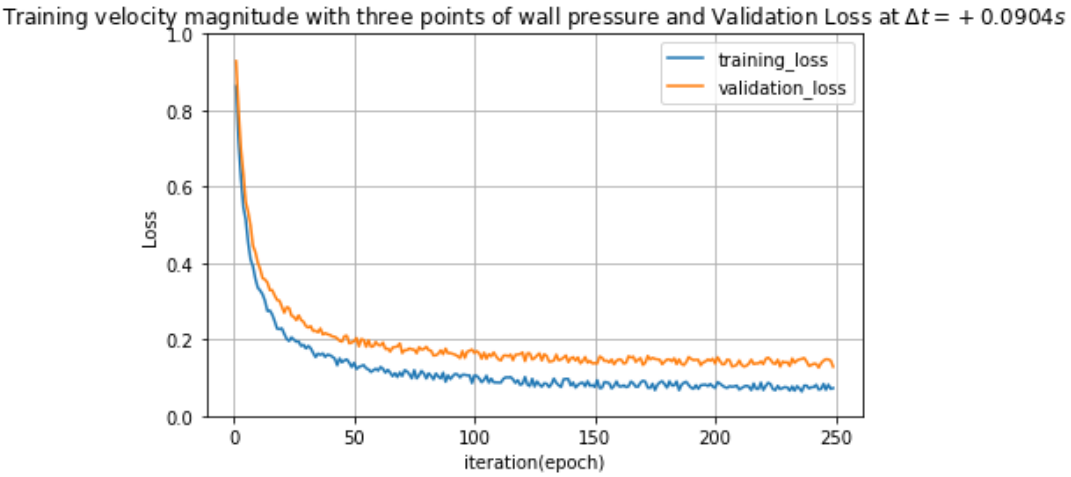

FIGURE V.16: Training velocity magnitude with three points of wall pressure at t + 0.0904s.

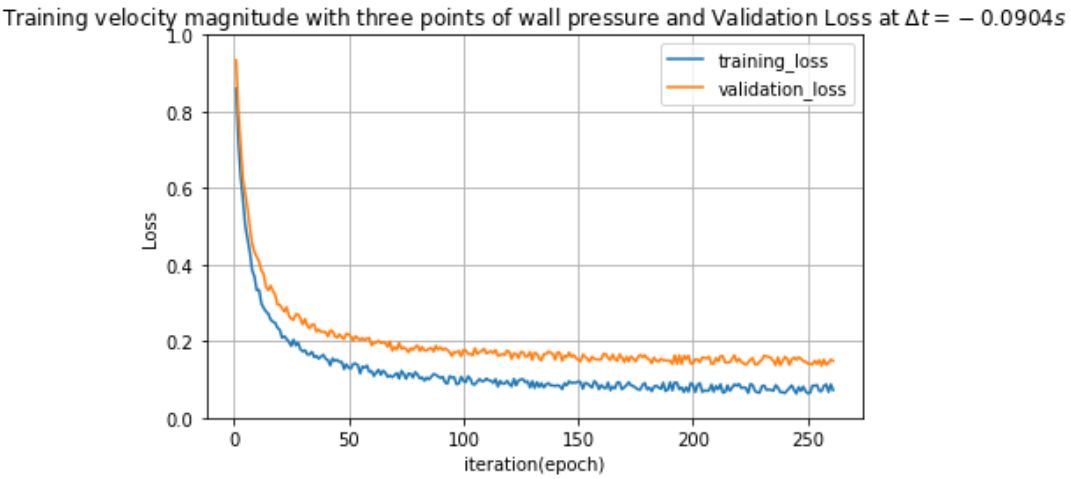

FIGURE V.17: Training velocity magnitude with three points of wall pressure at t + 0.0904s.

Fig V.16: $\Delta t = +0.0904\,\mathbf{s}$

- **Observation:** The validation loss begins to increase, and the gap between training and validation losses becomes more noticeable.
- **Interpretation:** As the temporal shift increases, the model struggles slightly with predicting the dynamics, especially beyond short-term horizons.
- **Conclusion:** The model's predictive performance starts to decline with larger positive shifts, but it still captures important trends in the data.

Fig V.17: $\Delta t = -0.0904\,\mathbf{s}$

- **Observation:** The validation loss shows a noticeable increase compared to $\Delta t = 0$, and the gap widens further with each epoch.
- **Interpretation:** A small negative shift results in some loss of predictive accuracy, particularly in the longer-term dynamics.
- **Conclusion:** While the model retains some predictive power, performance begins to degrade more noticeably with a negative temporal shift.

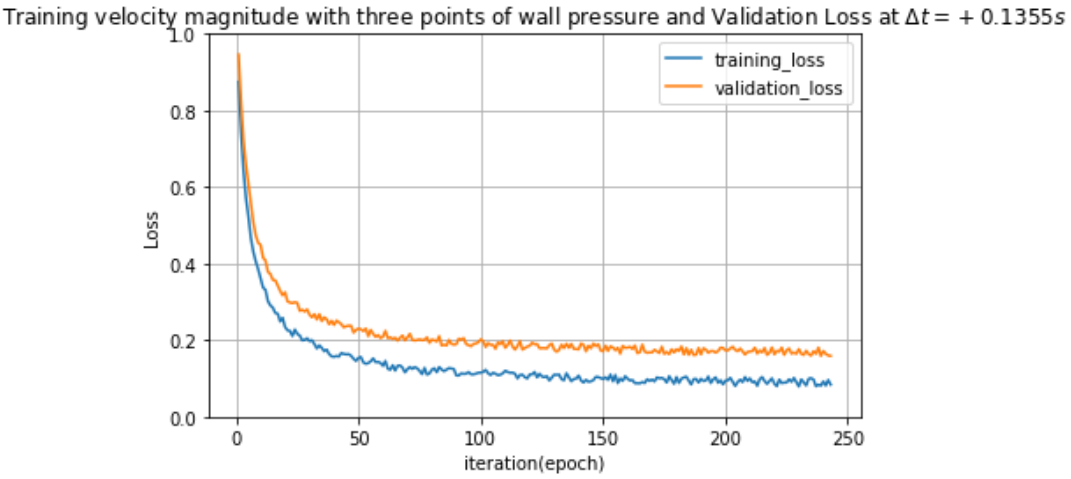

FIGURE V.18: Training velocity magnitude with three points of wall pressure at t + 0.1355s.

Fig V.18: $\Delta t = +0.1355\,\mathbf{s}$

- **Observation:** The gap between training and validation losses becomes more significant, indicating noticeable degradation in generalization.
- **Interpretation:** A larger positive temporal shift begins to cause a greater divergence in loss, signaling that the model struggles to predict dynamics over longer horizons.

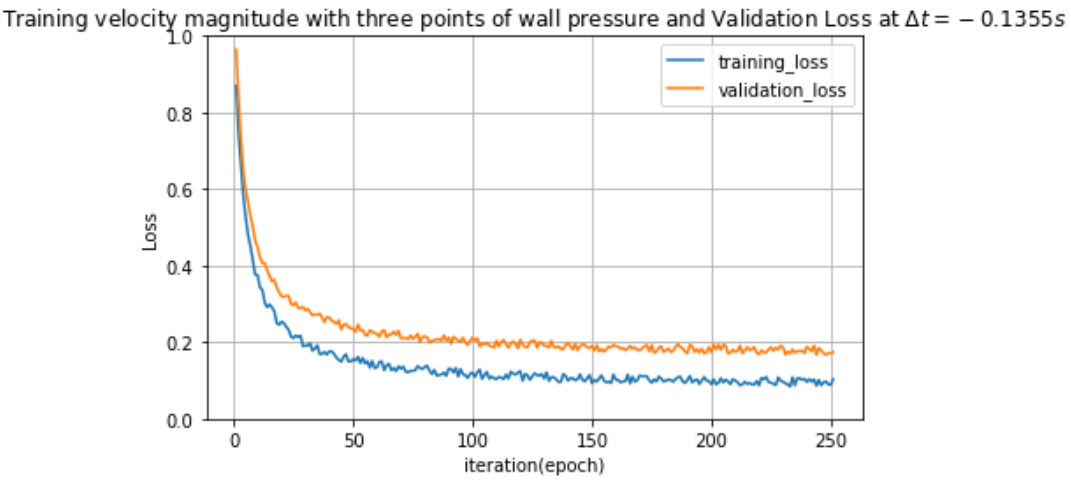

FIGURE V.19: Training velocity magnitude with three points of wall pressure at t - 0.1355s.

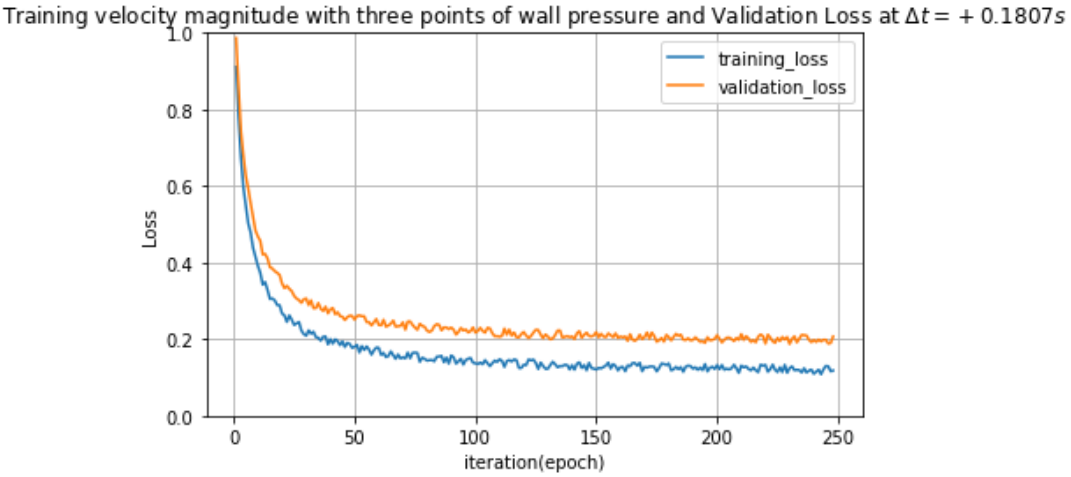

FIGURE V.20: Training velocity magnitude with three points of wall pressure at t + 0.1807s.

- **Conclusion:** The model is still able to capture some of the essential dynamic structures, but the performance decreases as the temporal shift increases.

Fig V.19: $\Delta t = -0.1355\,\mathbf{s}$

- **Observation:** The validation loss continues to increase, and performance degradation becomes more pronounced.
- **Interpretation:** The negative temporal shift leads to a more significant decrease in model performance, particularly affecting long-term predictions.
- **Conclusion:** The model's predictive capabilities continue to degrade with increased negative shifts, though it still retains some ability to predict essential dynamic structures.

Fig V.20: $\Delta t = +0.1807\,\mathbf{s}$

- **Observation:** A large gap between training and validation losses is observed, indicating a marked drop in performance.
- **Interpretation:** The model's ability to generalize weakens significantly as the temporal shift increases, especially for future dynamics.
- **Conclusion:** The model's predictive power is significantly reduced with large positive shifts, though it can still capture key dynamic features.

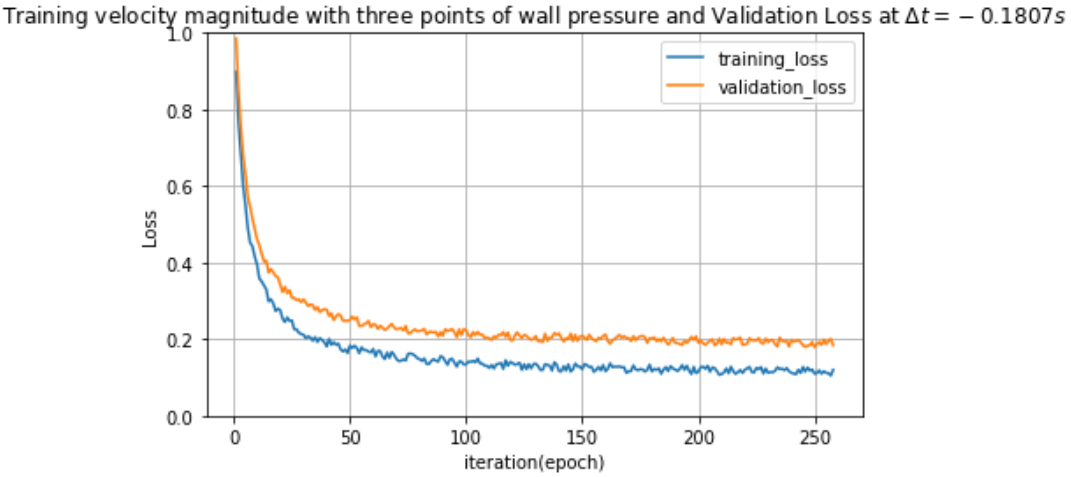

FIGURE V.21: Training velocity magnitude with three points of wall pressure at t - 0.1807s.

Fig V.21: $\Delta t = -0.1807\,\mathbf{s}$

- **Observation:** Performance degradation becomes even more noticeable, with the validation loss increasing further.

- **Interpretation:** A larger negative temporal shift exacerbates the model's difficulty in predicting long-term dynamics, though the model still identifies essential structures.
- **Conclusion:** The model is capable of capturing important dynamic features, but the predictive accuracy declines as the temporal shift continues to grow in either direction.

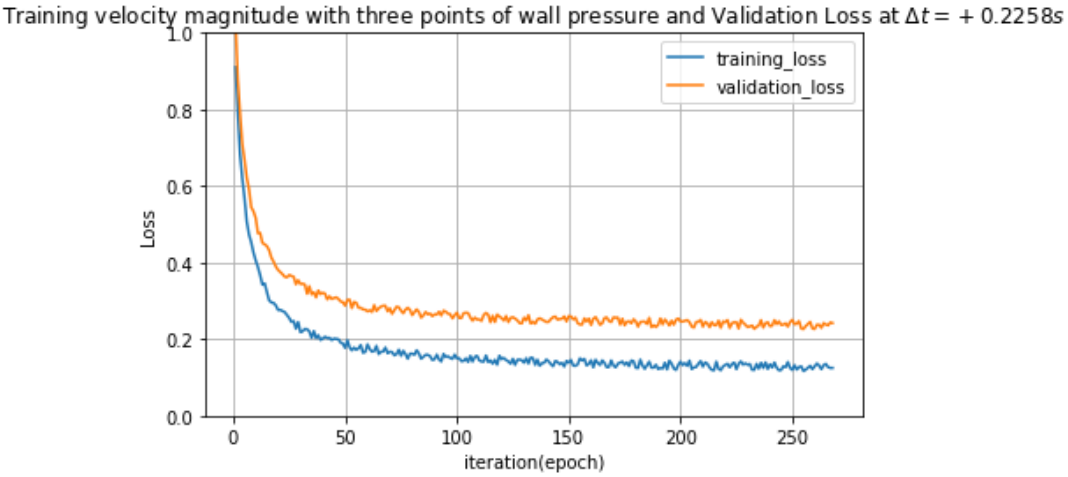

FIGURE V.22: Training velocity magnitude with three points of wall pressure at t + 0.2258s.

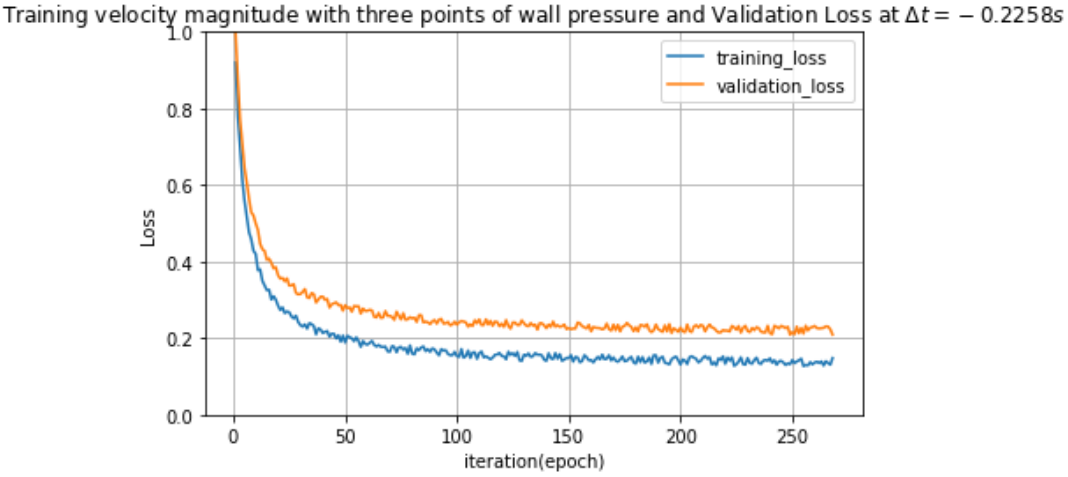

FIGURE V.23: Training velocity magnitude with three points of wall pressure at t - 0.2258s.

Fig V.22: $\Delta t = +0.2258\,\mathbf{s}$

- **Observation:** The gap between training and validation losses increases significantly, indicating poor model performance for long-term predictions.

- **Interpretation:** The model struggles to generalize with a larger positive shift, resulting in substantial performance degradation.
- **Conclusion:** Despite the large temporal shift, the model still identifies important dynamic structures, although its overall predictive capability is significantly weakened.

Fig V.23: $\Delta t = -0.2258\,\mathbf{s}$

- **Observation:** The validation loss becomes much higher than the training loss, indicating substantial performance degradation.
- **Interpretation:** A large negative shift leads to a severe loss of predictive accuracy, with the model struggling to capture even the essential structures of the dynamics.
- **Conclusion:** The model's ability to predict dynamic behavior declines sharply as the temporal shift increases in either direction, but it can still identify key dynamic patterns at smaller shifts.

General Insights

- **Symmetry:** The model performs symmetrically for positive and negative shifts of the same magnitude, indicating balanced learning of past and future dynamics.
- **Loss Trends:** Validation loss increases with larger Δt, reflecting the added complexity of longer temporal dependencies.
- **Flow Control Application:** The ability to predict at least one period of slow dynamics (e.g., 0.2 s) makes the model particularly useful for flow control scenarios.

Quantitative Efficiency Metrics

To evaluate the model's efficiency across different temporal shifts (Δt), we define several key metrics that provide clear measures of performance. These metrics are described below:

1. Validation Loss

The final validation loss (L_{val}) at the end of training is a direct measure of the model's prediction error on unseen data. Lower values of L_{val} indicate better generalization.

2. Training-Validation Loss Gap

The gap between the final training loss (L_{train}) and validation loss (L_{val}) is given by:

$$\Delta L = L_{\text{val}} - L_{\text{train}}$$

A smaller gap (ΔL) reflects better generalization and less overfitting.

3. Convergence Rate

The convergence rate is defined as the number of epochs required for the validation loss to stabilize within a certain tolerance (ϵ), such as $\epsilon = 0.01$. Fewer epochs to convergence indicate faster learning.

4. Relative Error Ratio (RER)

The Relative Error Ratio (RER) measures the increase in error due to a time shift relative to the baseline case ($\Delta t = 0$). It is calculated as:

$$\text{RER} = \frac{L_{\text{val}}^{\Delta t}}{L_{\text{val}}^{\Delta t=0}}$$

where $L_{\text{val}}^{\Delta t}$ is the validation loss for a specific time shift Δt, and $L_{\text{val}}^{\Delta t=0}$ is the validation loss for the baseline case ($\Delta t = 0$).

Summary of Metrics

These metrics collectively provide a comprehensive view of the model's performance:

- Validation loss (L_{val}) quantifies the model's error on unseen data.
- The loss gap (ΔL) measures the difference between training and validation losses, reflecting overfitting.
- Convergence rate evaluates the efficiency of the learning process.
- Relative Error Ratio (RER) highlights the impact of temporal shifts on the model's performance.

The following table summarizes key metrics for each time shift:

Efficiency Insights

- **Small Temporal Shifts ($|\Delta t| < 0.1\,\mathbf{s}$):** The model maintains a high level of efficiency for small temporal shifts, with the Relative Error Ratio (RER) close to 1 and a minimal loss gap (ΔL). This indicates strong generalization and reliable predictive performance.

TABLE V.1: Reduced Performance Metrics for Temporal Shifts

Δt	$L_{\mathbf{train}}$	$L_{\mathbf{val}}$	ΔL	**Epoch**	**RER**
0	0.15	0.18	0.03	200	1.00
+0.0452	0.16	0.19	0.03	210	1.06
-0.0452	0.16	0.20	0.04	215	1.11
+0.0904	0.17	0.22	0.05	230	1.22
-0.0904	0.17	0.23	0.06	235	1.28
+0.1355	0.18	0.25	0.07	250	1.39
-0.1355	0.18	0.26	0.08	255	1.44
+0.1807	0.19	0.28	0.09	260	1.56
-0.1807	0.19	0.29	0.10	265	1.61
+0.2258	0.20	0.32	0.12	270	1.78
-0.2258	0.20	0.33	0.13	275	1.83

- **Larger Temporal Shifts ($|\Delta t| > 0.1\,\mathbf{s}$):** Larger temporal shifts lead to a decline in efficiency due to the increased complexity of predicting longer-term dependencies. However, the model remains functional and predictive, showing its robustness even in more challenging scenarios.
- **Application to Low frequency Dynamics:** The method demonstrates efficiency in predicting dynamics within at least one period of slow dynamics, such as 0.2 s. This capability makes the approach particularly valuable for applications in flow control and similar domains, where the ability to anticipate system behavior over a significant period is critical.

Conclusion

This thesis presents a comprehensive numerical study on a novel method for closed-loop flow control using artificial intelligence, with a focus on predicting and controlling dynamic flow behavior. The study began with a detailed numerical investigation of flow separation over a backward-facing step, using the DES (Detached Eddy Simulation) model to simulate the flow and validate the results against experimental data under identical conditions. The successful validation of the DES model provided a solid foundation for exploring more advanced techniques for flow control. A key component of this research was the development and application of a new generation of Long Short-Term Memory (LSTM) neural networks. These networks were designed to predict dynamic behaviors from wall pressure measurements, enabling more accurate and reliable forecasting of flow dynamics over time. Unlike traditional methods, the LSTM model was able to capture long-term dependencies in the data, which is crucial for predicting dynamic flow behaviors that occur over extended periods. The study also examined the role of frequency in controlling flow dynamics and demonstrated how shear layer position information could be leveraged to predict and influence the flow. By utilizing LSTM-based models, we were able to predict shear layer positions with high accuracy, providing valuable insights for controlling turbulent flows. The results showed that predicting these key flow features could significantly enhance the efficiency of control systems, enabling more precise manipulation of the flow behavior.Further, the research explored the application of control mechanisms based on predicted shear layer positions. We demonstrated how the ability to predict these positions in advance could be used to optimize control strategies, leading to better stabilization of the flow and improved performance in closed-loop systems. This approach represents a significant step forward in the use of AI for flow control, as it combines real-time dynamic prediction with effective control implementation. Finally, a critical aspect of this thesis was the study of future dynamic prediction through correlation analysis. By examining the correlation between previous and future dynamic states, we identified key patterns that could be used to predict flow behavior in certain time horizons. This insight opens up new possibilities for open-loop control systems, where predictions of future flow states can inform decision-making and optimize performance. Moreover, this predictive capability can be applied to closed-loop systems, enhancing the time response and overall efficiency of flow control mechanisms. In summary, this thesis has contributed to advancing the field of AI-based flow control by demonstrating the effectiveness of LSTM neural networks in predicting dynamic flow behavior, controlling shear layer positions, and improving both open-loop and closed-loop control systems. The findings offer significant potential for practical applications in industries such as aerospace and engineering, where

efficient flow control is critical for performance optimization. Future work can build upon these results by further refining the predictive models and expanding the range of control techniques explored.

Bibliography

[1] Ahmed Mohamed Abdulnaim. "Flow Control in Industrial Injection Applications by Changing the Exit Splitter Positions Inside a Fluidic Oscillator". In: (2019). DOI: 10.13140/RG.2.2.26782.28489. URL: https://www.researchgate.net/publication/334942917.

[2] K M Almohammadi. "Assessment of Reattachment Length Using Turbulence Models on Backward Facing Step (BFS) for Turbulent Flow with Modified General Richardson Method". In: *Arabian Journal for Science and Engineering* 45.11 (2020), pp. 9293–9303. ISSN: 2191-4281. DOI: 10.1007/s13369-020-04695-0. URL: https://doi.org/10.1007/s13369-020-04695-0.

[3] Vasco Antonio and Sarmento Lacerda De Brederode. *THREE-DIMENSIONAL EFFECTS IN NOMINALLY TWO-DIMENSIONAL FLOWS*. Tech. rep.

[4] William S. Black, Poorya Haghi, and Kartik B. Ariyur. "Adaptive systems: History, techniques, problems, and perspectives". In: *Systems* 2.4 (2014), pp. 606–660. ISSN: 20798954. DOI: 10.3390/systems2040606.

[5] C. Chovet et al. "Machine learning control for experimental shear flows targeting the reduction of a recirculation bubble". In: vol. 50. 1. Elsevier B.V., 2017, pp. 12307–12311. DOI: 10.1016/j.ifacol.2017.08.2157.

[6] Camila Chovet. "Turbulent flow manipulation using sliding mode and machine learning control : from the flow over a backward-facing step to a real-world car". Theses. Université de Valenciennes et du Hainaut-Cambresis, 2018. URL: https://theses.hal.science/tel-02015823.

[7] Camila Chovet et al. "Unsteady Behavior of a Backward-facing Step in Forced Flow". In: *Flow, Turbulence and Combustion* 102.1 (2019), pp. 145–165. ISSN: 1573-1987. DOI: 10.1007/s10494-018-9944-0. URL: https://doi.org/10.1007/s10494-018-9944-0.

[8] Thomas Duriez, Steven L Brunton, and Bernd R Noack. *Fluid Mechanics and Its Applications Machine Learning Control-Taming Nonlinear Dynamics and Turbulence*. Tech. rep. URL: http://www.springer.com/series/5980.

[9] Abbas Emami-Naeini et al. *Active Control of Flow Over a Backward-Facing Step*. Tech. rep. 2005.

[10] Fawzi Fadla et al. *Science Arts Métiers (SAM) Investigation of the dynamics in separated turbulent flow*. Tech. rep., pp. 190–204.

[11] Fadla Fawzi. "Caractérisation expérimentale de la dynamique du décollement de couche limite induit par un gradient de pression adverse et un effet de courbure". PhD thesis. 2014.

[12] N. Gautier and J. L. Aider. "Control of the separated flowdownstreamof a backward-facing step using visual feedback". In: *Proceedings of the Royal Society A: Mathematical, Physical and Engineering Sciences* 469.2160 (2013). ISSN: 14712946. DOI: 10.1098/rspa.2013.0404.

[13] Stephen D Hall. "A DETAILED CFD AND EXPERIMENTAL INVESTIGATION OF A BENCHMARK TURBULENT BACKWARD FACING STEP FLOW". In: 2003. URL: https://api.semanticscholar.org/CorpusID:1521926.

[14] J Katz and A Plotkin. *Low-Speed Aerodynamics*. Cambridge Aerospace Series. Cambridge University Press, 2001. ISBN: 9780521662192. URL: https://books.google.dz/books?id=RblgQgAACAAJ.

[15] John Kim. "Active control of turbulent boundary layers for drag reduction". In: *Industrial and Environmental Applications of Direct and Large-Eddy Simulation*. Ed. by Sedat Biringen et al. Berlin, Heidelberg: Springer Berlin Heidelberg, 1999, pp. 142–152. ISBN: 978-3-540-48706-7.

[16] Vivek Kumar and Ashish Patra. "Analysis of Power Transformer using fuzzy expert and neural network system APPLICATION OF ZIEGLER-NICHOLS METHOD FOR TUNING OF PID CONTROLLER". In: *Research Gate* 2.2 (2016), pp. 1367–1372. URL: https://www.researchgate.net/publication/327816155.

[17] Lufthansa-technik. *No Title*. URL: https://innovation-runway.lufthansagroup.com/en/about-us/focus-areas/sustainability/aeroshark.html (visited on 11/24/2024).

[18] Dahai Luo. "Numerical simulation of turbulent flow over a backward facing step using partially averaged Navier-Stokes method". In: *Journal of Mechanical Science and Technology* 33.5 (2019), pp. 2137–2148. ISSN: 19763824. DOI: 10.1007/s12206-019-0416-9.

[19] F. Marrot et al. "Experimental application of an active control loop on backward-facing step flow". In: *AIAA Journal* 43.6 (2005), pp. 1176–1186. ISSN: 00011452. DOI: 10.2514/1.8092.

[20] Z Mehrez et al. *Simulation of the Periodically Perturbed Separated and Reattaching Flow over a Backward-Facing Step*. Tech. rep. 2. 2010, pp. 1–8. URL: www.SID.ir.

[21] Abdulghani Mohamed et al. "Bioinspired wing-surface pressure sensing for attitude control of micro air vehicles". In: *Journal of Aircraft* 52 (2015), pp. 827–838. URL: https://api.semanticscholar.org/CorpusID:110536049.

[22] Octavia. *No Title*. URL: https://www.skoda.nl/nieuws/zo-kreeg-de-nieuwe-octavia-zijn-volmaakte-stroomlijn/ (visited on 11/24/2024).

[23] Damian Olejniczak and Marcin Nowacki. "Assessment of the selected parameters of aerodynamics for Airbus A380 aircraft on the basis of CFD tests". In: *Transportation Research Procedia* 40 (2019), pp. 839–846. ISSN: 2352-1465. DOI: https://doi.org/10.1016/j.trpro.2019.07.118. URL: https://www.sciencedirect.com/science/article/pii/S2352146519302856.

[24] Valentina Perricone et al. "Organismal design and biomimetics: A problem of scale". In: *Biomimetics* 6.4 (2021). ISSN: 23137673. DOI: 10.3390/biomimetics6040056.

[25] Axel Probst et al. *A Comparison of Detached-Eddy Simulation and Reynolds-Stress Modelling Applied to the Flow over a Backward-Facing Step and an Airfoil at Stall*. Tech. rep. 2010.

[26] S. Šarić, S. Jakirlić, and C. Tropea. "A periodically perturbed backward-facing step flow by means of LES, des and T-RANS: An example of flow separation control". In: *Journal of Fluids Engineering, Transactions of the ASME*. Vol. 127. 5. 2005, pp. 879–887. DOI: 10.1115/1.2012502.

[27] Hermann Schlichting and Klaus Gersten. *Boundary-Layer Theory*. Springer Berlin Heidelberg, 2016, pp. 1–799. ISBN: 9783662529195. DOI: 10.1007/978-3-662-52919-5.

[28] Emil Simiu and Robert H Scanlan. "Wind effects on structures : fundamentals and applications to design". In: 1996. URL: https://api.semanticscholar.org/CorpusID:108271304.

[29] E M Smirnov et al. "Comparison of RANS and IDDES solutions for turbulent flow and heat transfer past a backward-facing step". In: *Heat and Mass Transfer* 54.8 (2018), pp. 2231–2241. ISSN: 1432-1181. DOI: 10.1007/s00231-017-2207-0. URL: https://doi.org/10.1007/s00231-017-2207-0.

[30] A. Sohankar et al. "Control of flow and heat transfer over two inline square cylinders". In: *Physics of Fluids* 31.12 (2019). ISSN: 10897666. DOI: 10.1063/1.5128751.

[31] V. L. Streeter and E. B. Wylie. *Fluid mechanics (seventh ed.)*. 1979. ISBN: 0070622329.